Spring 5-31-2011

Numerical and asymptotic modeling of evolving nonlinear ocean surface wave fields

Matt Malej
New Jersey Institute of Technology

ABSTRACT

NUMERICAL AND ASYMPTOTIC MODELING OF EVOLVING NONLINEAR OCEAN SURFACE WAVE FIELDS

by
Matt Malej

The main focus of this dissertation is the asymptotic and numerical modeling of nonlinear ocean surface wave fields. In particular, a development of an accurate numerical model for the evolution of nonlinear ocean waves, including extreme waves known as Rogue/Freak waves. Due to their elusive and destructive nature, the media often portrays Rogue waves as unimaginatively huge and unpredictable monsters of the sea. To address these concerns, derivations of asymptotically reduced models, based on the small wave steepness assumption, are presented and their corresponding numerical simulations via a Fourier pseudo-spectral method are discussed. The simulations are initialized with a well-known JONSWAP wave spectrum and different angular distributions are employed. Both deterministic and Monte-Carlo simulations and the corresponding analysis were carried out. Based on preliminary numerical analysis, certain conclusions are drawn on the validity of the modified nonlinear Schrödinger equation (MNLS) of Dysthe (1979) in relation to realistic ocean surface waves and its ability to predict the occurrence of large amplitude waves known as Rogue or Freak waves.

Furthermore, this dissertation concerns the development of a new computationally efficient numerical model for the short term prediction of evolving weakly nonlinear ocean surface waves. The derivations are originally based on the work of West et al. (1987) and Choi (1995) and since the waves in the ocean tend to travel primarily in one direction, the aforementioned new numerical model is derived based on additional assumption of a weak transverse dependence. In turn, comparisons of the ensemble averaged random initial spectra, as well as deterministic surface-to-surface

correlations are presented. The new model is shown to behave quite well in various directional wave fields and can potentially be a candidate for computationally efficient prediction and propagation of large ocean surface waves – Rogue/Freak waves.

NUMERICAL AND ASYMPTOTIC MODELING OF EVOLVING NONLINEAR OCEAN SURFACE WAVE FIELDS

by
Matt Malej

A Dissertation
Submitted to the Faculty of
New Jersey Institute of Technology
and Rutgers, The State University of New Jersey – Newark
in Partial Fulfillment of the Requirements for the Degree of
Doctor of Philosophy in Mathematical Sciences

Department of Mathematical Sciences, NJIT
Department of Mathematics and Computer Science, Rutgers-Newark

May 2011

APPROVAL PAGE

NUMERICAL AND ASYMPTOTIC MODELING OF EVOLVING NONLINEAR OCEAN SURFACE WAVE FIELDS

Matt Malej

Dr. Wooyoung Choi, Dissertation Advisor — Date
Professor, Department of Mathematical Sciences, NJIT

Dr. Michael Booty, Committee Member — Date
Professor, Department of Mathematical Sciences, NJIT

Dr. Linda J. Cummings, Committee Member — Date
Associate Professor, Department of Mathematical Sciences, NJIT

Dr. Richard O. Moore, Committee Member — Date
Associate Professor, Department of Mathematical Sciences, NJIT

Dr. Philippe Guyenne, Committee Member — Date
Associate Professor, Department of Mathematical Sciences, University of Delaware

BIOGRAPHICAL SKETCH

Author: Matt Malej

Degree: Doctor of Philosophy

Date: May 2011

Undergraduate and Graduate Education:

- Doctor of Philosophy in Mathematical Sciences,
  New Jersey Institute of Technology, Newark, NJ, 2011
- Master of Science in Applied Mathematics,
  New Jersey Institute of Technology, Newark, NJ, 2010
- Bachelor of Science in Mathematics,
  New Jersey Institute of Technology, Newark, NJ, 2006

Major: Mathematical Sciences

Presentations and Publications:

Malej, M., Goullet, A. and Choi W., "A new efficient model for the evolution of directional ocean surface wave fields," (in preparation).

Malej, M., Martinez, D. and Mascarinas A. "Using experimental methods and mathematical modeling to determine gap junctional coupling in neural networks," *CAMS (NJIT) Report 0506-9,* Newark, New Jersey, 2006.

Malej, M. "Numerical and reduced order asymptotic modeling of nonlinear deep-water ocean surface waves," *Fluid Dynamics Seminar – US Army Engineer Research and Development Center – Coastal & Hydraulics Laboratory,* Vicksburg, MS, February 2011.

Malej, M. "Spectral evolution and instabilities of nonlinear deep-water ocean waves," *SIAM Conference on Nonlinear Waves and Coherent Structures - Minisymposium on Waves, Stratified Fluids and Transport,* Philadelphia, PA, August 2010.

Malej, M. "Numerical and asymptotic modeling of evolving nonlinear ocean surface wave fields," *Oceanography Seminar – Naval Research Laboratory,* Stennis Space Center, MS, March 2010.

To the memory of my father, Wojciech Malej.

ACKNOWLEDGMENT

I would like to thank my advisor, Dr. Wooyoung Choi, for his support during the past years. He has introduced me to the topic of nonlinear ocean surface waves and showed me how interesting this field of research can be. Above all, it was an invaluable experience to be under his guidance and supervision. He has always been inspirational and available for questions and discussions, more than I could have asked for. Above all, he was always understanding of my commitments and interests outside of research work and allowed me to experience the graduate school to its fullest capacity.

I would like to thank my committee members, Dr. Michael Booty, Dr. Richard O. Moore, Dr. Linda J. Cummings, and Dr. Philippe Guyenne, whose very useful comments and suggestions led to significant improvements of my Ph.D. dissertation.

I would like to extend my gratitude to Dr. David J. Horntrop, without whom the decision to embark on graduate career might not have happened. He has been my mentor and a friend on countless occasions and for that I am extremely grateful.

I would also like to thank Dr. Daljit S. Ahluwalia, for his financial support (Ahluwalia Fellowship) during my last graduate years, as well as his insights to life beyond the student years.

In addition, I would like to thank my fellow graduate students, more specifically, Jacek Wrobel, Matthew Causley, Dongwook Kim, Daniel Fong, Daniel Cargill, and Oleksiy Varfolomiyev, for being great friends and colleagues in the last five years.

Finally, I would like to thank my family for their support. In particular, I would like to thank my wife, Wioletta, for her love and support, plus for finally understanding that "working from home" does not imply having ample time to do various chores around the house.

TABLE OF CONTENTS

Chapter **Page**

LIST OF TABLES

Table **Page**

LIST OF FIGURES

LIST OF FIGURES
(Continued)

Figure **Page**

LIST OF FIGURES
(Continued)

Figure **Page**

LIST OF FIGURES
(Continued)

Figure **Page**

LIST OF FIGURES
(Continued)

Figure **Page**

Symbol	Description	Units
$\bar{a}$	characteristic wave height	meters $[m]$
$E[\cdot]$	statistical averaging	quantity dependent
$F(k,\theta)$	wavenumber spectrum	m^2
g	gravitational acceleration	m/s^2
h	undisturbed water depth	m
H_s	significant wave height	m
k_p	peak wave number	m^{-1}
k_x, k_y	horizontal wavenumbers / Fourier multipliers	m^{-1}
M_n	nth statistical moment	dimensionless
$m_3(\zeta)$	skewness	dimensionless
$m_4(\zeta)$	kurtosis	dimensionless
p	pressure	$kg/m \cdot s^2$
T_p	peak period	seconds $[s]$
β	directional spectral distribution parameter	dimensionless
$\epsilon = k_p\bar{a}$	wave steepness	dimensionless
γ	peak enhancement	dimensionless
λ	wavelength	m
ν	kinematic viscosity	m^2/s
$\omega(k_x, k_y)$	angular frequency / dispersion relation	s^{-1}
$\phi(x,y,z,t)$	velocity potential	m^2/s
ρ	fluid/water density	kg/m^3
σ	standard deviation	dimensionless
$\zeta(x,y,t)$	surface elevation	m

CHAPTER 1

INTRODUCTION

1.1 Objective

Computing efficiently and accurately the evolution of highly nonlinear time-dependent, three-dimensional surface wave fields in various ocean environments is certainly a challenging hydrodynamic problem. Consequently, a considerable effort and resources have been allocated towards a better understanding of large nonlinear ocean waves over the course of the last decade (Waseda et al. 2009). These large waves whose height surpasses twice the significant wave height (H_s) of the analyzed field are commonly referred to as Rogue or Freak Waves. In terms of waves with broad directional distribution, it has been shown by Onorato et al. (2002) and Socquet-Juglard et al. (2005) that as directional distribution broadens, the occurrence of these uncommonly large waves subsides. Those findings were normally supported via statistical methods, such as a measure of the fourth statistical moment (kurtosis), see for example Dysthe et al. (2003), Waseda et al. (2009b), or Toffoli et al. (2010).

When considering the prevalent theories, it is believed that these extreme waves occur more frequently than random superposition of different waves would predict. Though questionable, a common assumption in modeling is that the sea state is a stationary random process. This tends to give a false impression on the frequency of the occurrence of these extremely large waves. Prevailing models for describing such phenomena are highly complex. These models do not possess analytic solutions and hence require careful and costly numerical computations. In modeling, a large number of factors need to be considered such as: variable bottom topography, ocean currents, wave-wind interactions and energy dissipation due to wave breaking. An additional complication is that there is a wide range of scales to be resolved. The

coupling between various modes and thus the energy transfer between different length scales lack a thorough understanding (Waseda et al. 2009a).

In the effort of bringing the oceanographic community closer towards real time wave prediction, the objective of this research has been the development of an efficient numerical model to accurately forecast the evolution of weakly nonlinear, multi-directional irregular surface wave fields in the ocean. Also, in order to better understand the underling physical effects and to deviate from having to carry out intensive numerical computations of the full Euler equations, in this dissertation we re-derived, based on the work of West et al. (1987) and Choi (1995), a reduced model accurate to a third order in wave steepness. In fact, Dommermuth and Yue (1987) have also independently derived a similar model, commonly referred to as a HOSM (higher-order spectral method). For an excellent review of various computational approaches to nonlinear free-surface flows see Tsai and Yue (1996).

Subsequently, since waves in the ocean tend to primarily travel in one direction, we also proposed a new weakly two-dimensional (Weakly 2D) model based on additional assumption of weak transverse dependence. This weak transverse dependence is exhibited in the wavenumber ratio k_y/k_x being on the order of wave steepness (ϵ), where k_y and k_x are of course the horizontal wavenumbers. The models are presented for arbitrary water depth ($0 < h < \infty$), as well as for both shallow or infinitely deep water.

This dissertation is organized as follows. In chapter 1 we give the objective, motivation and the background information, as well as several accounts of marine ship accidents attributed to Rogue/Freak waves. In §1.4 we present the mathematical formulation of an ideal fluid with a free-surface. In chapter 2, we re-derive the fully two-dimensional (Fully 2D) model based on the work of West et al. (1987) and Choi (1995), and introduce a new model based on weak transverse dependence (Weakly 2D). Then in chapter 3, we give a detailed description of our numerical method and

statistical description of the realistic ocean wave fields. In chapter 4, we present the results of the simulations for the deterministic surface-to-surface comparisons and ensemble averaged wavenumber spectra for an array of initial wave fields. The comparisons are made between the Fully 2D and the Weakly 2D model, as well as, between Fully 2D and MNLS (Modified Nonlinear Schrödinger Equation) of Dysthe (1979). Also, in chapter 5, we show how the Fully 2D model can be effectively uncoupled and separated into unidirectional components. Finally, in chapter 6 the concluding remarks are given. In addition, in the Appendix we carry out linearized stability analysis for the MNLS and plot regions of modulational instability of the Stokes wave for the MNLS. Ultimately, we argue that the Weakly 2D model behaves quite well in broad directional wave fields. Moreover, even though our models do not account for wave breaking, we still observed permanent downshifting of the spectral peak. In that respect, it appears that the primary driving mechanism behind the spectral downshifting is indeed the nonlinear wave-wave interaction, brought about by the mode coupling and thus the nonlinear energy transfer.

1.2 Background Information

Whether being on a beach or onboard a vessel, one of the first things one will notice when looking at the ocean are the omnipresent surface waves. Despite that, relatively little progress had been made from the times of ancient Greeks to the 19th century. Some of the great minds like George Biddell Airy (1801-1892), John Scott Russell (1808-1882), Sir George Stokes (1819-1903), Lord Rayleigh (1842-1919), and Joseph Boussinesq (1842-1929) are among the scientists who provided important contributions to the development of ocean waves. Generally speaking, ocean surface waves are the result of forces acting on the initially uniform ocean surface. In fact, many types of waves involving different physical factors exist in the ocean and all must be associated with some form of a restoring force. It is therefore convenient to

make a rough classification of ocean waves according to their restoring force as (also summarized in Table 1.1):

Table 1.1 Classification of Various Ocean Surface Wave Types Based on the Restoring Force. The Typical Period in the Third Column is Given in Seconds (sec), Minutes (min), Hours (h), and Days.

Wave Type	*Physical Mechanism*	*Typical Period*	*Populated Regions*
Sound	Compressibility	10^{-2} *to* 10^{-5} *sec*	Underwater
Capillary	Surface Tension	$< 10^{-1}$ *sec*	Surface
Gravity & Swells	Gravity	1 *to* 25 *sec*	Surface
Tsunami	Gravity	10 *min to* 2 *h*	Surface
Internal	Layer Stratification	2 *min to* 10 *h*	Deep Ocean (interior)
Tides	Earth Rotation	12 *to* 24 *h*	Entire Ocean

- Water compressibility which leads to the creation of sound waves that are not discussed further in this dissertation.
- Pressure fluctuations or atmospheric stresses (particularly from the wind) create capillary and gravity waves.
- Subsurface earthquakes that create long surface gravity waves (tsunami) that have enormous destructive powers, especially for coastal and riverine communities. The earthquake can create a long wave of small amplitude traveling very fast (often several hundreds of miles per hour) in the deep ocean. While the wave approaches shallow coastal water on the continental shelves, it slows down and increases in amplitude and can even travel thousands of kilometers away from the earthquake.

- Gravitational attraction from the moon and rotation (Coriolis force) of the earth can generate tidal waves.

Unnatural physical event can also produce waves in the ocean. One can take the example of a boat cruising in Norwegian fjords. Depending on the boat's speed and the depth of the fjord, it can generate waves which become high enough to cause damage along the coast.

Ocean surface waves have been a subject of study with an increasing interest over the last several decades. Shipping companies, offshore industries (especially the oil and gas producers), fish industries, harbors (transport of sediments), tourist industry (ships, waves breaking on beaches) and environmentalists are becoming increasingly concerned about the role of the ocean waves. A better understanding of the waves can play a major role in the economy, the safety of populations and the protection of the world. A wave hitting an oil platform and stopping the production of oil means several millions of dollars lost per day for the company. When a tsunami reaches a coast without warning, thousands of human lives may be lost.

For the present dissertation, however, the primary motivation has been the so-called Freak/Rogue wave, also commonly referred to as extreme wave. These waves are storm waves with extreme heights compared to the significant wave height of the surrounding wave field. The commonly accepted definition of the significant wave height (H_s), is the average of the top one-third (1/3) of the highest wave heights. The meaning of a wave height (H) is simply a distance from a trough to a peak and when we talk about the wave height, we have to distinguish between up-crossing (H-) and down-crossing (H+) wave heights. In turn, the height of the wave will ultimately be the maximum value of the up-crossing and down-crossing wave heights, as is illustrated in Figure 1.1. An alternative point of view exists on rogue waves that consists of two views: (1) "classical" extreme waves (that are described by standard physical models and statistics) and (2) "freak" extreme waves (that need a new set of

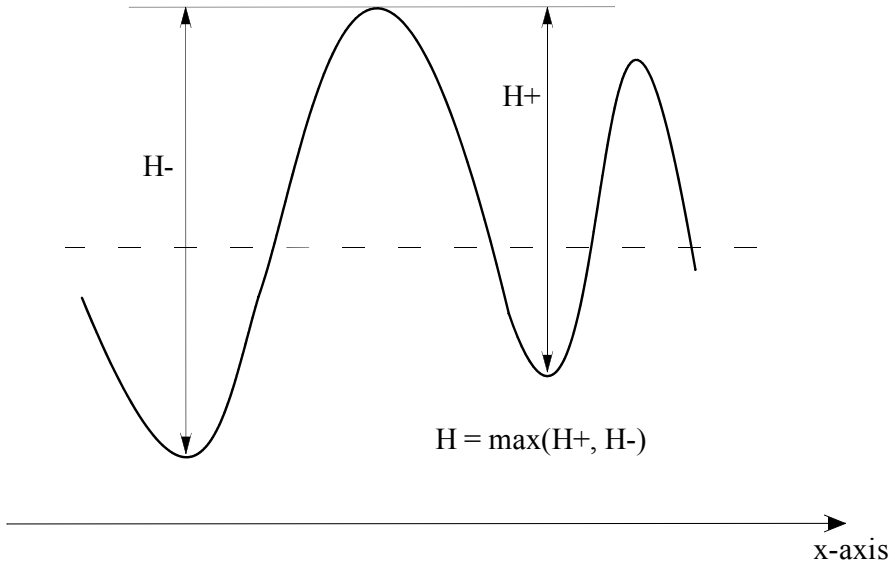

Figure 1.1 Schematic and definition of a wave height (H).

theories and approaches) (Haver 2005). This concept is primarily based on stochastic (probabilistic) approaches and considerations. In this dissertation, however, we are concerned with all kinds of extreme waves and we do not make a distinction between rouge and freak waves; thus we use those two terms interchangeably.

Before discussing more details of water waves, few basic assumptions about the ocean are needed, mainly:

- The water is considered to be incompressible.
- It has an inviscid nature, meaning that any frictional forces are neglected and only gravity and pressure forces are taken into account, although for the majority of this dissertation only gravity waves will be considered.
- The fluid is irrotational.

When observing the ocean from a beach during calm weather, one can notice the presence of nearly sinusoidal long-crested and progressive waves. These waves will become higher and shorter when reaching the coast and will finally break. This phenomenon is well-known among the surfers. The water depth (h) plays a major role in ocean physics. When a wave propagates, both surface and underwater particles are in motion. The phase speed and the frequency of the waves depends on depth (h) through the dispersion relation. This comes from the fact that water is a dispersive media, in other words - water waves of different wavelengths (λ) and frequency travel with different speeds. A simple classification using the water depth (h) and the wavelength (λ) to characterize the ocean can be made as follows

- Shallow water $h < \lambda/25$
- Transitional/Arbitrary/Finite depth $\lambda/25 < h < \lambda/4$
- Deep water $\lambda/4 < h$.

Here, we deal primarily with a finite water depth, with occasional considerations of the other two ends of the spectrum (shallow and deep water). The dispersive nature of water waves can be described by the fundamental relationship between the wavenumber $k = \sqrt{k_x^2 + k_y^2}$, where k_x and k_y are the horizontal wavenumbers, and the angular wave frequency ($\omega = \omega(k)$), which is commonly referred to as dispersion relation. This relation can be easily derived from the linear theory and has the following form

$$\omega^2 = gk \tanh(kh), \tag{1.1}$$

where g is the gravitational acceleration equal to $9.81 m/s^2$. For deep water, $\tan(kh) \approx 1$ and the dispersion relation reduces to $\omega^2 = gk$. When watching the ocean, it is relatively obvious that the sea is not a single sinusoidal wave. Moreover, it is not easy to get a general description, or the governing law for the surface elevation.

Waves have different speeds, amplitudes, directions, and wavelengths. Short waves ride on top of the long waves and small waves are overtaken by longer waves. When observing one particular point on the ocean surface it seems that it evolves almost randomly. Looking at a larger piece of the ocean from a satellite, however, one can see the influence of the wind and the different patterns – especially in the coastal areas where the surface interacts with the bottom topography.

In addition, when one treats the ocean surface waves as a stationary random process (a stochastic process whose joint probability distribution does not change when shifted in time or space), then they can be simulated as the sum of simple sinusoidal waves with different wavelengths, frequencies, amplitudes, and directions. By the same token, one can include a large number of simple sinusoidal waves to build the sea surface. Therefore, it should not be surprising that adding two-dimensional (2D) waves with different heights, wavelengths and directions, will ultimately result in a realistic ocean surface field where seemingly no general physical laws are observed. In fact, Lord Rayleigh once said:"The basic law of the seaway is the apparent lack of any law."

From the theory established by Fourier, it follows that the sea surface at a given instant can be obtained from the superposition of many simple sinusoidal waves. It is quite fascinating to realize that something very complicated can be constructed by adding relatively simple elements. In linear theory, one can simulate the sea surface at any time by adding many sinusoidal waves like

$$\zeta(x,y,z,t) = \sum_i \sum_j a_{i,j} \ \exp\left(k_{x_i}x + k_{y_j}y - \omega(k_x,k_y)t + \phi_n\right) + c.c.\,, \tag{1.2}$$

where *c.c.* stands for the complex conjugate with random phases ϕ_n. Each sinusoidal wave in the sum is an elementary wave, often referred to as a Fourier mode. Taking nonlinear effects into account, however, means that the individual Fourier modes are

coupled. Thus the amplitudes ($a_{i,j}$) and phases (ϕ_n) are changing with time and in principle have to be computed at every time step.

1.3 Freak/Rogue Waves

This section presents some accounts and stories about freak waves, which have been presented in scientific papers, as well as popular scientific magazines and even the media. Media accounts often portray rogue waves as unimaginatively huge monsters of the sea, mainly due to their size and unpredictable nature. There are many well-documented cases of the occurrence of extreme waves. Until few decades ago, these extreme waves were usually dismissed as simple mariners' tales and were given very little credibility. In fact, when captain Dumont d'Urville, a French scientist and naval officer on an expedition in 1826, along with three of his colleagues, reported seeing waves up to 30 meters high, they were openly ridiculed as such waves were practically impossible to experience given the current water wave theories.

Until recent, the largest reliably measured waves have had the heights of 30 meters, in particular the waves registered during the "Halloween Storm" in 1991 and Hurricane Luis in 1995. Currently, the observations and hence data collection of extreme waves from space have been possible with SAR (Synthetic Aperture Radar) and other similar satellite imagining devices. These large waves are usually generated by storms and hurricanes, hence one would expect the occurrence of rogue waves to increase, or become more probable during severe weather. In fact, Komar (2007) reported a substantial increase in typical wave heights during a season of tropical storms in the North Atlantic region.

The list of marine accidents attributed to extreme waves contains many records in the recent decades. Twenty-two super carriers were lost or severely damaged between 1969 and 1994 due to occurrence of sudden rogues waves and a total of 542 lives were lost as a result of these accidents (Lawton 2001). Figures 1.2-1.3 show

respectively, the density of ship accidents and individual ship accidents between the years of 1995-1999 around the world, collected by the Lloyds Marine Information Service (LMIS). The areas of East China Sea and the North Sea are well known for abnormally large waves. Therefore, it is not a surprise that the largest concentration and occurrence of ship accidents, due to collisions with extreme waves, are in these parts of the world.

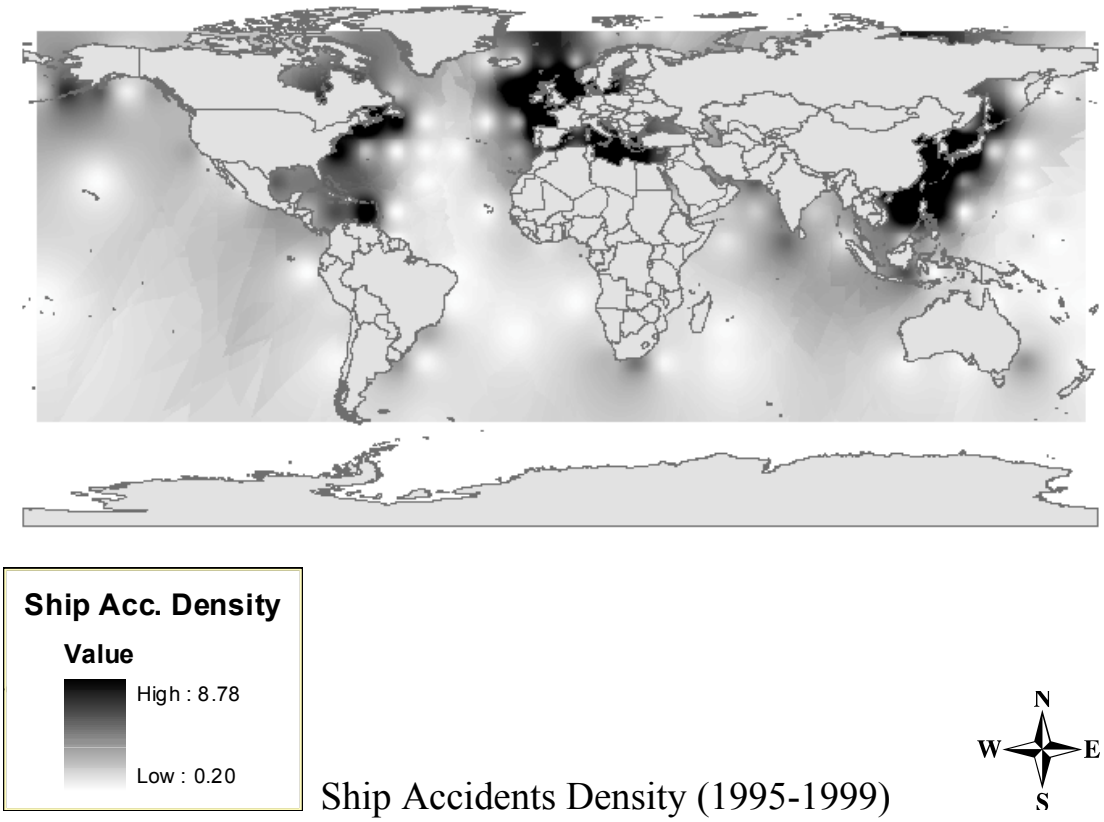

Figure 1.2 Geographical distribution: ship accidents in the period of five years from 1995 to 1999. Taken from the Lloyds Marine Information Service (LMIS) casualty database.

Moreover, the number of accidents reported by the media is growing and the issue of huge sea waves has attracted many people from various communities (scientific and non-scientific). Some of the recent accidents with large ocean liners that include Queen Elizabeth II in 1995, Bremen and Caledonian Star 2001, and Norwegian Dawn in 2005, demonstrate the destructive powers of rogue waves.

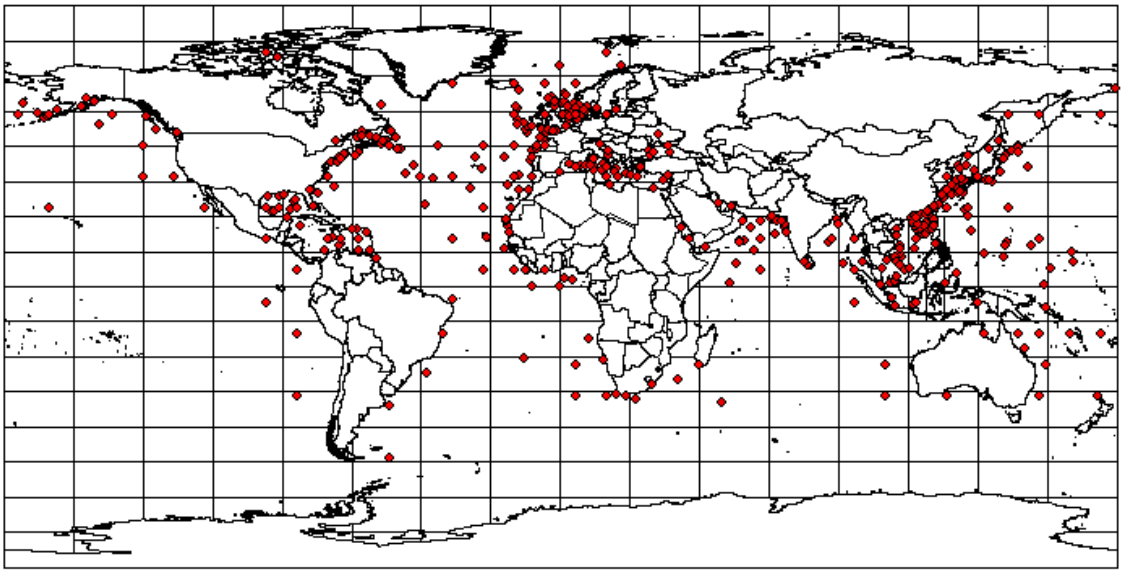

Figure 1.3 Worldwide ship accidents (1995-1999) due to severe weather. Taken from the Lloyds Marine Information Service (LMIS) casualty database.

Offshore platforms are also quite vulnerable to rogue waves; not so much about the loss of life, but more about the financial and ecological problems a damaged oil drilling platform can create. The famous New Year Waves hit the Draupner platform on January 1, 1995, with a height of approximately 26 meters, while the typical surrounding waves were about 10-11 meters (Trulsen and Dysthe 1997).

Over the past few decades, the combination of in situ and remote sensing observations have demonstrated that extremely large nonlinear rogue waves are ubiquitous features of costal oceans (Kharif et al. 2009). Much of the modern interest in large surface waves in oceanography began in the early 1960s with an interesting confluence of advances in ocean instrumentation, applied mathematics, and remote sensing. Prevailing models for describing such phenomena are highly complex. These models do not possess analytic solutions and hence require careful and costly numerical computations. In addition, calculations and predictions generated by these models are often inaccurate due to oversimplifications in the models and their numerical schemes. In modeling, a large number of factors need to be considered such as: variable bot-

tom topography, ocean currents, wave-wind interactions, and energy dissipation due to wave breaking. An additional complication is that there is a wide range of scales to be resolved. The coupling between various modes and thus the energy transfer between different length scales lack a thorough understanding. The ability to predict more accurately the generation and propagation of highly nonlinear ocean wave fields, such as rogue (freak) waves, will be crucial for a number of engineering and scientific applications.

Furthermore, there are many individuals and government agencies that dedicate a lot of resources toward a better understanding of water waves. For example: civil and ocean engineers trying to protect coastal and offshore structures, naval architects designing ships, and physical oceanographers investigating air-sea interaction, are all interested in obtaining a better understanding of the dynamics of nonlinear ocean waves. Increasingly, the investigation of nonlinear ocean surface waves requires high power computing. Global propagation and real time wave field prediction is still a computationally formidable task, since it requires correlating a vast amount of in situ experimental data with proposed models and the resolution of large scale interactions (Osborne 2010). One of the questions addressed in this research is, do these extreme waves occur more frequently than random superposition of different waves would predict? Though questionable, a common assumption in modeling is that the sea state is a stationary random process. This tends to give a false impression on the frequency of the occurrence of these extremely large waves (Waseda – private communications). Another hydrodynamic difficulty is an accurate computation of the highly nonlinear time-dependent, three-dimensional surface wave fields in various ocean environments.

From the physical point of view, there have been several plausible explanations for the generation of rogue waves, some of which include:

- focusing due to modulational instability (Benjamin-Feir instability)

- wave-current interaction
- geometric (spatial) focusing
- dispersive focusing (spatio-temporal focusing)
- soliton collisions.

Waves with hight exceeding 30 meters are being reported more frequently these days. This certainly has to do with an increasing number of freight vessels in the sea, as well as the ever increasing growth of technology and communication. Freak waves in shallow and deep water have been observed all around the world, along the South African coast, East China Sea, in the Gulf of Mexico, or in the North Sea. In regards to possible mechanism of rogue wave generation in linear theory, one can cite Lavrenov (1998) (amplification due to opposing current), White and Fornberg (1998) (wave focusing due in a random current) and Kharif et al. (2000) (wave focusing in arbitrary depth). On the other hand, for the nonlinear theory, one can mention the work of Dysthe and Trulsen (1999) with the Modified Nonlinear Schrödinger Equations, or Onorato et al. (2002) via the Zakharov equation.

The following are accounts of crew members and witnesses of recent ship accidents attributed to rogue waves.

- **Cruise Liner Queen Elizabeth II**

  Reported by E.S.A. (European Space Agency)

  The Cruiser Liner Queen Elizabeth II was struck by a 30-meter high rogue wave during a hurricane in the North Atlantic during the month of February in 1995. Ronald Warwick, the captain of the vessel, described the incident as "a great wall of water... it looked as if we were going into the White Cliffs of Dover."

- **The Bremen and the Caledonian Star**

  Reported by E.S.A. (European Space Agency)

In March of 2001 two tourist cruisers,The Bremen and the Caledonian Star, had their bridge and windows smashed by 30-meter waves, as they were cruising in the South Atlantic. As a result of this impact, the Bremen was left drifting without navigation or propulsion for about two hours. A senior scientist of the Bremen (Wolfgang Rosenthal) accounts: "All the electronics were switched off on the Bremen as they drifted parallel to the waves, and until they were turned on again the crew were thinking it could have been their last day alive. The same phenomenon could have sunk many less lucky vessels: two large ships sink every week on average, but the cause is never studied to the same detail as an air crash. It simply gets put down to bad weather."

- **Statoil Oil Platform**

  The Draupner oil rig owned by Statoil in the North Sea had registered on January 1, 1995, a nearly 26 meter wave (see Figure 1.4). In addition, the same year in the North Sea, Statoil floating rig Veslefrikk-B becomes severely damaged by a rogue wave. Though rogue waves are usually short lived, one of the crew members of the floating rig described the wave as a"wall of water" visible for several minutes before it struck.

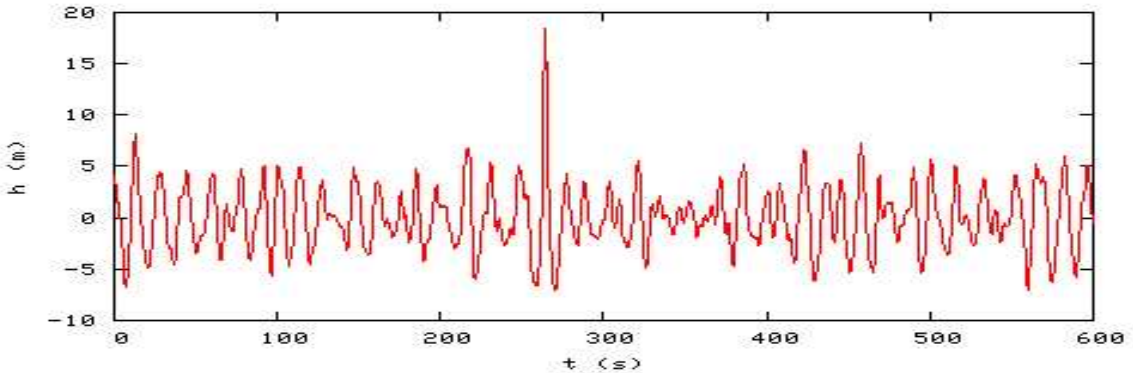

Figure 1.4 New Year wave which hit the Draupner offshore drilling platform on January 1, 1995.

- **Oil tankers damaged by giant waves off the south-east coast of South Africa**

  Smith (1976) had collected information on several ship accidents due to freak waves: "During the closure of the Suez Canal a number of ships, particularly oil tankers, have reported extensive damage caused by giant waves off the south-east coast of South Africa (Mallory 1974; Sturm 1974; Sanderson 1974). Two particularly unfortunate vessels are the World Glory, which broke in two and sank in June 1968, and the Neptune Sapphire, which lost 60 m of its bow section in August 1973. We can only speculate that giant waves may account for many of the ships which have been lost without trace off this coast."

- **Oil Tanker Esso Languedoc**

  Lawton (2001) reported the accounts of Philippe Lijour, who was a first mate on the oil tanker Esso Languedoc and was describing the huge wave that slammed into the ship off the east coast of South Africa in 1980: "We were in a storm and the tanker was running before the sea. This amazing wave came from the aft and broke over the deck. I did not see it until it was alongside the vessel but it was special, much bigger than the others. It took us by surprise. I never saw one again." Lijour and his shipmates are very fortunate to be alive. They were struck by a rogue wave – a monstrous wall of water, that rose out of nowhere and slammed onto the deck. Ships often do not survive an event of this magnitude. In fact, many vessels sink before anyone on board realizes what has hit them. Lijour had another stroke of luck that day. As the wave crashed into the ship, he managed to get a hold of his camera. The photograph he took, is one of the few images we have of a rogue wave (see Figure 1.5). It shows a large wall of water, much bigger that anything else in the surrounding sea at the time, smashing into the bow. Lijour estimated that the wave was around 20 meters high. In reality, it was most likely much bigger sine rogue waves are

Figure 1.5 Picture of a Rogue wave taken by Philippe Lijour on board of the oil tanker Esso Languedoc in 1980.

often preceded by a deep trough, thus when viewed from the sea surface shortly before it struck, the wave could have been as large as 30 meters or more.

- **SS Spray**

  Captain G. Anderson Chase was on board the SS Spray in February of 1986, in the Gulf Stream, off Charleston when the picture (see Figure 1.6) was taken. He wrote: "A substantial gale was moving across Long Island, sending a very long swell down our way, meeting the Gulf Stream. We saw several rogue waves during the late morning on the horizon, but thought they were whales jumping. It was actually a nice day with light breezes and no significant sea. Only the very long swell, of about 15 feet high and probably 600 to 1000 feet long. This one hit us at the change of the watch at about noon. The photographer was an engineer (name forgotten), and this was the last photo on his roll of film. We were on the wing of the bridge, with a height of eye of 56 feet, and this

wave broke over our heads. This shot was taken as we were diving down off the face of the second of a set of three waves, so the ship just kept falling into the trough, which just kept opening up under us. It bent the foremast (shown) back about 20 degrees, tore the foreword firefighting station (also shown) off the deck (rails, monitor, platform and all) and threw it against the face of the house. It also bent all the catwalks back severely. Later that night, about 7:30 pm, another wave hit the after house, hitting the stack and sending solid water down into the engine room through the forced draft blower intakes."

Figure 1.6 Picture of a big wave taken on board of the SS Spray in 1986.

1.4 Mathematical Formulation – Ideal Fluid with a Free-Surface

In a wide variety of gravity wave problems, the variation of water density is insignificant over the temporal and spatial scales of interest. The fundamental conservation

laws (mass & momentum) are adequately described by the Navier-Stokes equations:

$$\begin{aligned} &\text{Conservation of Mass :} && \nabla \cdot \mathbf{u} = 0, \\ &\text{Conservation of Momentum :} && \left(\tfrac{\partial}{\partial t} + \mathbf{u} \cdot \nabla\right) \mathbf{u} = -\nabla \left(\tfrac{p}{\rho} + g\mathbf{z}\right) + \nu \nabla^2 \mathbf{u}, \end{aligned} \tag{1.3}$$

where $\mathbf{u}(x, y, z, t)$ is the velocity vector, $p(x, y, z, t)$ is the pressure, ρ is the density, g is the acceleration due to gravity, and ν is the kinematic viscosity. The illustration of problem geometry is provided in Figure 1.7. In water, where the kinematic viscosity (ν) is small ($\approx 10^{-2} cm^2/s$), the last term in the momentum balance equation of (1.3) is negligible except in the regions of large velocity gradients and strong vorticity. Furthermore, for an inviscid irrotational flow, the velocity ($\mathbf{u}$) can be expressed as the gradient of a scalar potential (ϕ)

$$\mathbf{u} = \nabla \phi$$

and ultimately the following physical setup is employed, (where $\boldsymbol{x} \equiv (x, y)$):

- Ideal Fluid (Inviscid, Incompressible, Irrotational)
- No variable bottom topography (flat bottom)
- No imposed currents or atmospheric pressure fluctuations (waves are fully developed).

Here, ∇ is defined as the horizontal gradient: $\nabla \equiv \left(\frac{\partial}{\partial x}, \frac{\partial}{\partial y}\right)$, while the free-surface elevation as $z = \zeta(\boldsymbol{x}, t)$ and so the governing equation for the velocity potential is the three-dimensional Laplace equation

$$\nabla^2 \phi + \frac{\partial^2 \phi}{\partial z^2} = 0 \qquad\qquad -h \leq z \leq \zeta(\boldsymbol{x}, t). \tag{1.4}$$

For variable bottom topography, h would in turn be a function of space $h = h(\boldsymbol{x})$, assuming, of course, no temporal variations. The boundary condition at the bottom

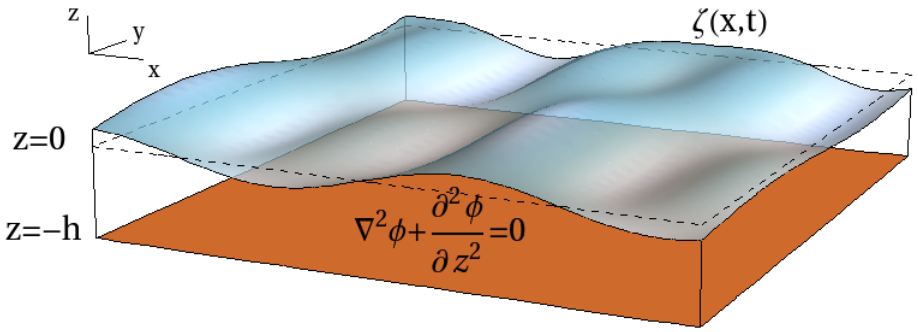

Figure 1.7 Physical three-dimensional setup of the ocean surface wave field. No variable topography or actions of current and atmospheric stresses are imposed, hence waves are fully developed.

is the standard kinematic boundary condition $\frac{D}{Dt}(z - h(\boldsymbol{x})) = 0$, where $\frac{D}{Dt}$ is the material derivative, but since a flat bottom is employed, it reduces to simply implying no vertical fluid velocity at the bottom

$$\frac{\partial \phi}{\partial z} = 0 \qquad \text{at} \quad z = -h. \tag{1.5}$$

The above problem is elliptic, hence in order to have any wave-like motion one needs to impose additional boundary conditions on the free-surface. Therefore, the free-surface boundary conditions are the kinematic (1.6) and dynamic (1.7) boundary conditions

$$\frac{\partial \zeta}{\partial t} + \nabla\phi \cdot \nabla\zeta = \frac{\partial \phi}{\partial z} \qquad \text{at} \quad z = \zeta(\boldsymbol{x}, t), \tag{1.6}$$

$$\frac{\partial \phi}{\partial t} + \frac{1}{2}|\nabla\phi|^2 + \frac{1}{2}\left(\frac{\partial \phi}{\partial z}\right)^2 + g\zeta = 0 \qquad \text{at} \quad z = \zeta(\boldsymbol{x}, t). \tag{1.7}$$

The kinematic boundary condition is a simple consequence of having particles of the free-surface remaining on the free-surface itself. Also, note that since the fluid is effectively inviscid, only the normal stress balance is considered with zero-atmospheric pressure above the free-surface and thus obtaining the dynamic boundary condition (1.7) directly from Bernoulli's equation, where g is the acceleration due to gravity.

It should also be noted that, since the the gravity waves will be of sole interest to us at the moment, the effects of surface tension are neglected, whose significance would be substantiated if the wavelengths were $O(1\,cm)$. That same point can be readily derived by making the linearized dynamic boundary condition (1.7) equal to the surface tension (since now the atmospheric pressure would be balanced by the effects of surface tension rather than simply being equal to zero). Subsequently, by assuming a wave-like form for the surface elevation $\zeta = A\,\cos(kx - \omega t)$, writing down a dispersion relation ($\omega = \omega(k)$) and balancing the effects of gravity and surface tension, one can ultimately show that the importance of surface tension in relation to gravity is measured by

$$\mathcal{P} = \frac{\alpha k^2}{\rho g}$$

being close to the value of one. Here, α is the surface tension constant of water, g is the usual gravitational acceleration and ρ is the density of water. Hence, for water surface waves $\mathcal{P} = 1$ when the wavelength is about 1.7 cm. Therefore, if the wavelengths are much larger than this, as is the case for gravity waves, the effects of surface tension are essentially negligible.

CHAPTER 2

SMALL WAVE STEEPNESS ASYMPTOTICS

2.1 Fully 2-Dimensional (Fully 2D) Model

This section concerns the derivation of what we call a Fully 2D model. It is based on a sole assumption of a small wave steepness (ϵ) and can be viewed (in a broad terms) as sort of boundary integral method. In other words, the field equations that govern the evolution of the surface elevation (ζ) and the velocity potential (ϕ) will be transformed into new canonical variables – the surface elevation $\zeta(x, y, t)$ and the velocity potential defined at the free surface $\Phi \equiv \phi(x, y, z = \zeta, t)$. That, in turn, will eliminate the need to solve Laplace equation for the velocity potential at every time step. Moreover, with this transformation we can utilize the two-dimensional (2D) FFT (Fast Fourier Transform) in our Fourier pseudo-spectral numerical method (discussed in the next chapter). The derivation of the Fully 2D model is based on the work of West et al. (1987) and Choi (1995).

At first, we will recast our free-surface boundary conditions into a different form - those having our velocity potential ϕ and the vertical velocity $\frac{\partial \phi}{\partial z}$ defined at the free-surface $z = \zeta$, mainly

$$\begin{cases} \Phi(\boldsymbol{x}, t) \equiv \phi(\boldsymbol{x}, z = \zeta, t) \\ W \equiv \frac{\partial \phi}{\partial z}(\boldsymbol{x}, z = \zeta, t), \end{cases} \tag{2.1}$$

and through a simple application of the chain rule we obtain

$$\begin{cases} \frac{\partial \phi}{\partial t}|_{z=\zeta} = \frac{\partial \Phi}{\partial t} - W \frac{\partial \zeta}{\partial t} \\ \nabla \phi|_{z=\zeta} = \nabla \Phi - W \nabla \zeta. \end{cases} \tag{2.2}$$

Then, we substitute (2.2) into the free-surface boundary conditions (1.6) and (1.7) and we obtain a system of two equation for kinematic and dynamic boundary condition in the following form (Zakharov, 1968)

$$\frac{\partial \zeta}{\partial t} + \nabla\Phi \cdot \nabla\zeta = \left(1 + |\nabla\zeta|^2\right) W, \tag{2.3}$$

$$\frac{\partial \Phi}{\partial t} + \frac{1}{2}|\nabla\Phi|^2 + g\zeta = \frac{1}{2}\left(1 + |\nabla\zeta|^2\right) W^2. \tag{2.4}$$

Equations (2.3) and (2.4) give a system of two equations with three unknowns. Hence, in order to close the system we need a constituent relation between Φ and W, i.e. we seek a way of representing W in terms of Φ and ζ.

For that, we start-off by expanding both Φ and W about the mean surface $z = 0$.

$$\begin{cases} \Phi(\boldsymbol{x}, t) = \phi(\boldsymbol{x}, z = 0, t) + \zeta\phi_z(\boldsymbol{x}, z = 0, t) + \frac{\zeta^2}{2}\phi_{zz}(\boldsymbol{x}, z = 0, t) + ... \\ W \equiv \phi_z(\boldsymbol{x}, z = \zeta, t) = \phi_z(\boldsymbol{x}, z = 0, t) + \zeta\phi_{zz}(\boldsymbol{x}, z = 0, t) + \frac{\zeta^2}{2}\phi_{zzz}(\boldsymbol{x}, z = 0, t) + ... \ . \end{cases} \tag{2.5}$$

Then, we define the velocity potential and the vertical velocity at the mean surface ($z = 0$) to be $\phi_o \equiv \phi(\boldsymbol{x}, 0, t)$ and $W_o = \frac{\partial\phi}{\partial z}(\boldsymbol{x}, 0, t)$, and with the help of our three-dimensional Laplace's equation can rewrite (2.5) as

$$\begin{cases} \Phi(\boldsymbol{x}, t) = \phi_o + \zeta W_o - \frac{\zeta^2}{2}\nabla^2\phi_o + ... \\ W = W_o - \zeta\nabla^2\phi_o - \frac{\zeta^2}{2}\nabla^2 W_o + ..., \end{cases} \tag{2.6}$$

where every instance of a second derivative of ϕ with respect to z was replaced by the negative horizontal laplacian.

Now, for our constituent relation between W and Φ (or rather W_o and ϕ_o) we will solve Laplace equation in the 3D rectangular region $-h \ \leq z \leq 0$ and $-\infty \leq \boldsymbol{x} \leq \infty$ via 2D Fourier transform. Our Fourier transform pair is

$$\begin{cases} \hat{\phi}(k_x, k_y, z, t) = \iint_{\mathbb{R}^2} \left(\phi(x, y, z, t) \mathrm{e}^{-ik_x x} dx\right) \, \mathrm{e}^{-ik_y y} dy \\ \phi(x, y, z, t) = \frac{1}{4\pi^2} \iint_{\mathbb{R}^2} \left(\hat{\phi}(k_x, k_y, z, t) \mathrm{e}^{ik_x x} dk_x\right) \, \mathrm{e}^{ik_y y} dk_y. \end{cases} \tag{2.7}$$

Hence, in Fourier space the Laplace equation becomes

$$\hat{\phi}_{zz} - \left(k_x^2 + k_y^2\right) \hat{\phi} = 0 \qquad \Rightarrow \qquad \hat{\phi} = A \cosh(\kappa(z+h)) + B \sinh(\kappa(z+h)) \,,$$

where $\kappa \equiv \sqrt{k_x^2 + k_y^2}$ and after imposing the boundary condition at the bottom ($z = -h$), as well as the fact that $\phi = \phi_o$ at $z = 0$ we obtain

$$\hat{W}_o = \hat{\phi}_o \kappa \tanh(\kappa\, h) = \left.\frac{\partial \hat{\phi}}{\partial z}\right|_{z=0} . \tag{2.8}$$

Consequently, inverting the Fourier transform yields our constituent relation (convolution)

$$W_o = \iint_{\mathbb{R}^2} \phi_o(\xi, \eta, t) \mathcal{K}(\xi - x,\, \eta - y)\, d\xi\, d\eta \;, \tag{2.9}$$

where $\mathcal{K}$ is the kernel defined by

$$\mathcal{K}(\xi - x,\, \eta - y) \equiv \frac{1}{4\pi^2} \iint_{\mathbb{R}^2} \sqrt{k_x^2 + k_y^2}\, \tanh\left(\sqrt{k_x^2 + k_y^2}\, h\right) \mathrm{e}^{ik_x(\xi - x)} \mathrm{e}^{ik_y(\eta - y)} dk_x\, dk_y \;.$$

Hereafter, the linear integral (convolution) operator (2.9) will be defined as

$$W_o \equiv -\mathcal{L}[\phi_o], \tag{2.10}$$

where the minus sign is added purely for convenience. It should perhaps be pointed out that our constituent relation (2.10) serves as a Dirichlet-to-Neumann operator. Craig and Sulem (1993) have also derived their version of a Dirichlet-to-Neumann operator for the unidirectional waves, while Bateman et al. (2001) proposed an extension of it to account for directionality.

Returning to our expansions of Φ and W (2.6) about the mean surface and substituting (2.10) yields

$$\begin{cases} \Phi = \phi_o - \zeta\mathcal{L}[\phi_o] - \frac{\zeta^2}{2}\nabla^2\phi_o + ... \\ W = -\mathcal{L}[\phi_o] - \zeta\nabla^2\phi_o + \frac{\zeta^2}{2}\nabla^2(\mathcal{L}[\phi_o]) + \dots \ , \end{cases} \tag{2.11}$$

which effectively closes the system. Note that the first equation in (2.11) can be formally inverted by writing

$$\begin{aligned} \phi_o &= \Phi + \zeta\mathcal{L}\left[\Phi + \zeta\mathcal{L}[\Phi + ...] + \frac{\zeta^2}{2}\nabla^2(\Phi + ...) + ...\right] \\ &\quad + \frac{\zeta^2}{2}\nabla^2\left(\Phi + \zeta\mathcal{L}[\Phi + ...] + \frac{\zeta^2}{2}\nabla^2(\Phi + ...) + ...\right) + \dots, \end{aligned}$$

which helps us write W solely in terms of Φ and ζ.

Finally, what we are left with is a straightforward substitution of (2.11) into (2.3) and (2.4). Then, we can effectively truncate our system at successive orders of wave steepness and our fully two-dimensional model (Fully 2D) accurate to the third order in wave steepness (ϵ) has the following dimensional form

$$\frac{\partial\zeta}{\partial t} = -\mathcal{L}[\Phi] - \nabla(\zeta\nabla\Phi) - \mathcal{L}[\zeta\mathcal{L}[\Phi]] - \nabla^2\left(\frac{\zeta^2}{2}\mathcal{L}[\Phi]\right) - \mathcal{L}\left[\frac{\zeta^2}{2}\nabla^2\Phi + \zeta\mathcal{L}[\zeta\mathcal{L}[\Phi]]\right] + O(\epsilon^4), \tag{2.12}$$

$$\frac{\partial\Phi}{\partial t} = -g\zeta - \frac{1}{2}|\nabla\Phi|^2 + \frac{1}{2}\left(\mathcal{L}[\Phi]\right)^2 + \mathcal{L}[\Phi]\left(\zeta\nabla^2\Phi + \mathcal{L}[\zeta\mathcal{L}[\Phi]]\right) + O(\epsilon^4). \tag{2.13}$$

In fact, one can write down a recursive formula which would yield the above mentioned (Fully 2D) system accurate to any order, see Choi and Lyzenga (2006).

2.2 Weak Transverse Dependence (Weakly 2-Dimensional Model)

Since the waves in the ocean tend to primarily travel in one direction, our weakly two-dimensional model (Weakly 2D) is based on additional assumption of weak transverse dependence. Recall the relations (2.8) and (2.10), where our operator $\mathcal{L}$ took the

following form in Fourier ($\mathcal{F}$) space

$$\mathcal{F}\left[\,\mathcal{L}[\Phi]\,\right] = -\kappa\,\tanh(\kappa h)\hat{\Phi}, \quad \text{where} \quad \kappa = \sqrt{k_x^2 + k_y^2} \quad \text{and} \quad \hat{\Phi} = \mathcal{F}[\Phi],$$

with h being the undisturbed water depth. In that respect, the weak transverse assumption is realized through the ratio k_y/k_x being small. How small it is, is a matter of predefined initial velocity wave field and since our original small parameter ϵ was defined to be a product of characteristic wave amplitude and peak wave number ($\epsilon = \bar{a}\,k_p$), we will set the ratio k_y/k_x to be $O(\epsilon)$. Also, our primary concern is the case of arbitrary water depth $0 < h < \infty$, but the other two extremes, infinitely deep and shallow water, are also presented. The modeled equations, correct to the third order in wave steepness (ϵ), in their symbolic Fourier form are given by

$$\begin{aligned}\zeta_t \;+\; & |k_x|\left(1+\tfrac{1}{2}\left(\tfrac{k_y}{k_x}\right)^2\right)\tanh(|k_x|h)\Phi + |k_x|\left(\tfrac{|k_x|h}{2}\left(\tfrac{k_y}{k_x}\right)^2\operatorname{sech}^2(|k_x|h)\right)\Phi \\ & + (ik_x\zeta\, ik_x\Phi - \zeta k_x^2\Phi) + |k_x|\tanh(|k_x|h)\,(\zeta|k_x|\tanh(|k_x|h)\Phi) \\ & -k_x^2\left(\tfrac{\zeta^2}{2}|k_x|\tanh(|k_x|h)\Phi\right) \\ & +|k_x|\tanh(|k_x|h)\left(-\tfrac{\zeta^2}{2}k_x^2\Phi + \zeta|k_x|\tanh(|k_x|h)(\zeta|k_x|\tanh(|k_x|h)\Phi\right) + O(\epsilon^4) \;=\; 0,\end{aligned} \tag{2.14}$$

$$\begin{aligned}\Phi_t \;+\; & g\zeta + \tfrac{1}{2}(ik_x\Phi)^2 - \tfrac{1}{2}(|k_x|\tanh(|k_x|h)\Phi)^2 \\ & -|k_x|\tanh(|k_x|h)\Phi\,(-\zeta k_x^2\Phi + |k_x|\tanh(|k_x|h)\,[\zeta|k_x|\tanh(|k_x|h)\Phi)]) + O(\epsilon^4) \;=\; 0.\end{aligned} \tag{2.15}$$

For clarity, the above mentioned symbolic Fourier form can be viewed as, for example:

$$k_x^2\left(\frac{\zeta^2}{2}|k_x|\tanh(|k_x|h)\Phi\right) \;\equiv\; \mathcal{F}^{-1}\left[k_x^2\,\mathcal{F}\left[\frac{\zeta^2}{2}\,\mathcal{F}^{-1}\{|k_x|\tanh(|k_x|h)\mathcal{F}[\Phi]\}\right]\right],$$

where $\mathcal{F}$ and $\mathcal{F}^{-1}$ are the forward and backward Fourier transforms, respectively. What should also be immediately apparent is that in equations (2.14) and (2.15) we have only two terms with transverse dependence (k_y). That very same point has great advantages for numerical computation and is discussed further in the subsequent sections.

In addition, when we consider an infinite water depth limit ($h \to \infty$) we recover the following system

$$\begin{aligned}\zeta_t \;&+\; |k_x|\left(1+\tfrac{1}{2}\left(\tfrac{k_y}{k_x}\right)^2\right)\Phi + (ik_x\zeta\, ik_x\Phi - \zeta k_x^2\Phi) + |k_x|\left(\zeta|k_x|\Phi\right) - k_x^2\left(\tfrac{\zeta^2}{2}|k_x|\Phi\right)\\ &+|k_x|\left(-\tfrac{\zeta^2}{2}k_x^2\Phi\right) + |k_x|\left(\zeta|k_x|(\zeta|k_x|\Phi)\right) + O(\epsilon^4) \;=\; 0,\end{aligned} \tag{2.16}$$

$$\Phi_t + g\zeta + \tfrac{1}{2}(ik_x\Phi)^2 - \tfrac{1}{2}(|k_x|\Phi)^2 - |k_x|\Phi\left(-\zeta k_x^2\Phi + |k_x|(\zeta|k_x|\Phi)\right) + O(\epsilon^4) \;=\; 0, \tag{2.17}$$

where in this case, we retain only one term that depends on transverse variable (k_y).

Furthermore, for the other end of the spectrum – the shallow water limit ($h \to 0$), upon taking the balance of $k_x h = \mathcal{O}(\epsilon^{1/3})$ the system (2.14)-(2.15) reduces to

$$\zeta_t + k_x^2 h\Phi + \left(ik_x\zeta\, ik_x\Phi - \zeta k_x +^2 \Phi\right) + k_x^2 h\left(\zeta k_x^2 h\Phi\right) + O(\epsilon^{\frac{10}{3}}) = 0, \tag{2.18}$$

$$\Phi_t + g\zeta + \frac{1}{2}(ik_x\Phi)^2 - \frac{1}{2}(k_x^2 h\Phi)^2 + O(\epsilon^{\frac{10}{3}}) \;=\; 0, \tag{2.19}$$

where the terms with transverse dependence occur at the next order, hence making the above two systems ($h \to \infty$ and $h \to 0$) especially attractive for our numerical simulations. In contrast to shallow water equations, such as for example the KP equation (Kadomtsev & Petviashvili 1970), the ratio k_y/k_x in the KP equation is $O(\epsilon^{1/3})$.

2.3 Modified Nonlinear Schrödinger Equation (MNLS)

The Modified Nonlinear Schrödinger equation (MNLS) governs the evolution of the so-called envelope (A) of the ocean surface waves, accurate to third-order in wave steepness (ϵ), see Figure 2.1 for the schematic. The subsequent derivation is directly based on the work of Trulsen and Dysthe (1996), hence most of the details will be omitted here. We begin with the field equations (1.4), (1.5), (1.6), and (1.7). The equations are then scaled by characteristic amplitude $\bar{a}$, peak wavenumber k_p, and

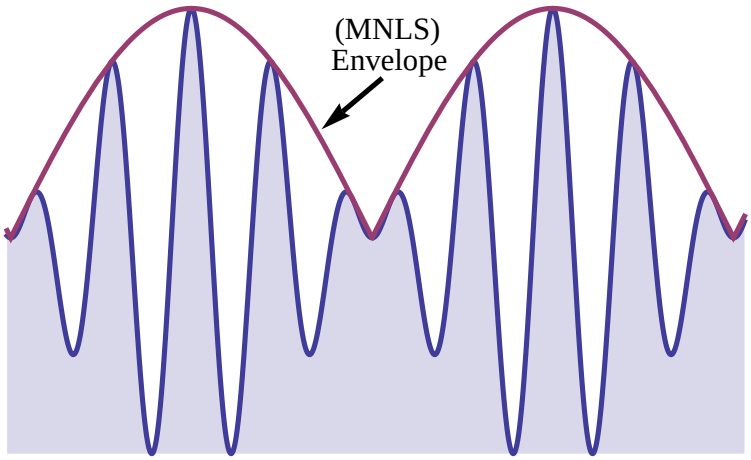

Figure 2.1 Sketch of an envelope of a periodic wave train, corresponding to the evolution of the first harmonic (A) in the Modified Nonlinear Schrödinger equation (MNLS).

peak frequency ω_p to give the following dimensionless quantities

$$\zeta' = k_p\zeta, \qquad \phi' = \frac{k_p}{\omega_p\bar{a}}\phi, \qquad (x', y', z') = k_p(x, y, z), \qquad t' = \omega_p t, \qquad d = k_p h.$$

Which, in turn, (after dropping primes for convenience) yield the following system

$$\nabla^2\phi + \tfrac{\partial^2\phi}{\partial z^2} = 0 \qquad -d \le z \le \epsilon\,\zeta(\bar{x}, t),$$

$$\tfrac{\partial\phi}{\partial z} = 0 \qquad at \quad z = -d,$$

$$\tfrac{\partial\zeta}{\partial t} + \epsilon\nabla\phi\cdot\nabla\zeta = \tfrac{\partial\phi}{\partial z} \qquad at \quad z = \epsilon\,\zeta(\bar{x}, t),$$

$$\tfrac{\partial\phi}{\partial t} + \tfrac{\epsilon}{2}|\nabla\phi|^2 + \tfrac{\epsilon}{2}\left(\tfrac{\partial\phi}{\partial z}\right)^2 + \tfrac{1}{\tanh(d)}\zeta = 0 \qquad at \quad z = \epsilon\,\zeta(\bar{x}, t),$$

where once again the wave steepness is $\epsilon = k_p\bar{a}$ and the last coefficient $1/\tanh(d)$ comes from the linearized dispersion relation $\omega^2 = gk_p\tanh(k_p h)$.

Furthermore, the wave field is assumed to have a narrow spectral bandwidth. By narrow, we imply that the bandwidth, defined by

$$\frac{\Delta k}{k}\,, \tag{2.20}$$

is on order of the wave steepness (ϵ). Subsequently, one can conveniently express the surface elevation (ζ) as superposition of harmonic modes about the peak frequency as

$$\begin{aligned}\zeta(x,y,t) &= \bar{\zeta}(\epsilon x,\epsilon y,\epsilon t)+\tfrac{1}{2}(A(\epsilon x,\epsilon y,\epsilon t)\mathrm{e}^{i\theta}+A_2(\epsilon x,\epsilon y,\epsilon t)\mathrm{e}^{2i\theta}\\ &+ A_3(\epsilon x,\epsilon y,\epsilon t)\mathrm{e}^{3i\theta}+...+c.c.),\end{aligned} \tag{2.21}$$

where $c.c$ stands for the complex conjugate and $\theta = k_x x - \omega t$. The coefficients A, A_2, and A_3 are functions of slow modulation variables in both space and time and are of first, second, and third order in wave steepness (ϵ), respectively. Moreover, $\bar{\zeta}$ is also a slowly varying variable in space and time, representing the mean surface elevation. In most of our subsequent numerical simulations, $\bar{\zeta}$ will be on the order of machine precision – hence for all practical purposes, zero.

The substitution of equation (2.21) into the rescaled field equations above is certainly a laborious procedure, but carrying it out to the third order in wave steepness ultimately yields the following system for the evolution of an envelope of a slowly varying wave field (wave train):

$$\begin{aligned}&\tfrac{\partial A}{\partial t}+\tfrac{1}{2}\tfrac{\partial A}{\partial x} \quad +\tfrac{i}{8}\tfrac{\partial^2 A}{\partial x^2}-\tfrac{i}{2}\tfrac{\partial^2 A}{\partial y^2}+\tfrac{i}{2}|A|^2A\\ &\quad -\tfrac{1}{16}\tfrac{\partial^3 A}{\partial x^3}+\tfrac{3}{8}\tfrac{\partial^3 A}{\partial x\partial y^2}+\tfrac{5}{4}|A|^2\tfrac{\partial A}{\partial x}+\tfrac{1}{4}A\tfrac{\partial|A|^2}{\partial x}+iA\tfrac{\partial\bar{\phi}}{\partial x}=0 \qquad \text{at} \qquad z=0,\end{aligned} \tag{2.22}$$

$$\frac{\partial\bar{\phi}}{\partial z}=\frac{1}{2}\frac{\partial|A|^2}{\partial x} \qquad \text{at} \qquad z=0, \tag{2.23}$$

$$\nabla^2\bar{\phi}+\frac{\partial^2\bar{\phi}}{\partial z^2}=0 \qquad -h\le z\le 0, \tag{2.24}$$

$$\frac{\partial\bar{\phi}}{\partial z}=0 \qquad \text{at} \qquad z=-h. \tag{2.25}$$

The reconstruction formulas are given by

$$\begin{aligned} \bar{\zeta} &= \tfrac{1}{2}\tfrac{\partial \bar{\phi}}{\partial x}, \\ A_2 &= \tfrac{1}{2}A^2 - \tfrac{i}{2}A\tfrac{\partial A}{\partial x}, \\ A_3 &= \tfrac{3}{8}A^3. \end{aligned} \tag{2.26}$$

Note that a similar system of evolution equations, along with reconstruction formulas for second and third order terms, can be obtained for the following expansion of the velocity potential (ϕ):

$$\phi(x,y,z,t) = \bar{\phi} + \frac{1}{2}\left(B\mathrm{e}^{\mathrm{i}\theta} + \mathrm{B}_2\mathrm{e}^{2\mathrm{i}\theta} + \mathrm{B}_3\mathrm{e}^{3\mathrm{i}\theta} + ... + \mathrm{c.c.}\right), \tag{2.27}$$

where $\bar{\phi}$ is the induced current.

It should also be noted that the MNLS equation was derived under the assumption of infinitely deep water, hence the dispersion relation was in the form of $\omega^2 = gk$. When we compare the numerical results on the MNLS with Fully 2D model in the subsequent sections, we take the depth (h) to be 20 meters, hence $\omega^2 = gk\tanh(kh) \sim gk$. However, when the depth is finite ($h \approx 1$), all of the coefficients of the MNLS equation become function of $\tanh(kh)$ and several new terms enter the equation to account for free long waves. Brinch-Nielsen and Jonsson (1986) derived equations for the temporal evolution of the velocity potential (B), while Sedletsky (2003) derived fourth-harmonic contribution for the temporal evolution of the velocity potential (B_4). The following two reconstruction formulas can be extracted from Brinch-Nielsen and Jonsson (1986) for the second and third harmonic of the surface elevation

$$A_2 = \frac{3 - \tanh(kh)^2}{4\tanh(kh)^3}A^2 + ...$$

$$A_3 = \frac{3(3 - \tanh(kh)^2)(3 + \tanh(kh)^4)}{64\tanh(kh)^6}A^3 + ...,$$

and in the limit ($h \to \infty$) the above two coefficients become 1/2 and 3/8, respectively. Therefore, it should be rather obvious that nonlinear contributions to the reconstruction of the surface elevation become more significant at smaller depths.

CHAPTER 3

NUMERICAL SIMULATIONS

3.1 Statistical Description of Realistic Ocean Surface Wave Fields

In reality, water waves obey certain physical laws and may be taken into account in a deterministic setting/model. In practice, however, this approach fails due to inadequate information about the sea state and its fluctuations in time. Generally speaking, a system of equations that one chooses to work with often suffers from sensitive dependence on initial data/conditions. From our daily experiences we know that the ocean waves behave irregularly and somewhat unpredictably on various time scales, nevertheless they can exhibit periodic behavior. Therefore, the dynamics of ocean waves often manifest a random (stochastic) nature. In that respect, the sea surface at a given place and time is represented by a random indexed function $\zeta_j(x, y, t)$ with some statistical properties. In turn, this approach is referred to as stochastic and aims at a statistical description of the sea surface. The goal is to describe and predict the dynamics of certain realizations on the basis of ensemble averages. This approach, in fact, is widely used in ocean engineering and atmospheric research.

Furthermore, in order to obtain time dependent statistical properties, we can elect to perform stochastic simulations – that is, we can use our deterministic models to compute a sufficient number of randomly chosen realizations of the sea state, i.e., Monte-Carlo simulations. The premise behind it is that, if we take a sufficiently large number of random representations of the sea surface, then the ensemble average of this large (but finite) number of simulations would adequately represent the evolution of the whole ensemble (in statistical sense). If we consider the surface elevation to be a function of both space and time $\zeta(x, y, t)$, then its autocorrelation function is

defined as

$$R(x,y,t;\,\bar{x},\bar{y},\tau) \equiv E\left[\zeta(x,y,t)\cdot\zeta(x+\bar{x},y+\bar{y},t+\tau)\right], \tag{3.1}$$

where $E[\cdot]$ denotes statistical averaging over the ensemble of realizations $\zeta_j(x,y,t)$ and has the following form

$$E\left[\zeta(x,y,t)\cdot\zeta(x+\bar{x},y+\bar{y},t+\tau)\right] = \lim_{N\to\infty}\frac{1}{N}\sum_{j=1}^{N}\zeta_j(x,y,t)\cdot\zeta_j(x+\bar{x},y+\bar{y},t+\tau). \tag{3.2}$$

Although in practice N is finite, it should be sufficiently large to provide a good estimate of the above limit. This approach requires the random process to be stationary (statistical properties do not depend on time). If we have stationarity and spatial homogeneity, then the autocorrelation function (3.1) does not depend on space and time. In turn, the equation (3.2) represents the mean energy density and via Parseval's formula for a finite Fourier series we can write

$$E \sim \sum_{l=1}^{N_1}\sum_{m=1}^{N_2}|a_{lm}|^2 = \frac{1}{N_1N_2}\sum_{l=1}^{N_1}\sum_{m=1}^{N_2}|\zeta_{lm}|^2, \tag{3.3}$$

where a_{lm} are the Fourier coefficients. Therefore, the Fourier transform of the autocorrelation function (3.1) gives the wave spectrum $F(k_x,k_y)$. Moreover, the integral of the spectrum gives the mean energy density in the physical domain $[L_x\times L_y]$

$$E = \int_{-k_{x\max}}^{k_{x\max}}\int_{-k_{y\max}}^{k_{y\max}}F(k_x,k_y)\mathrm{d}k_x\mathrm{d}k_y, \tag{3.4}$$

where $k_{x\max}$ and $k_{y\max}$ are given by

$$k_{x\max} = (N_x/2)\Delta k_x \quad\text{and}\quad k_{y\max} = (N_y/2)\Delta k_y \quad\text{with}\quad \Delta k_{x,y} = 2\pi/L_{x,y}.$$

It is also well known that the total energy of a linear progressive plane wave

$$\zeta(x,y,t) = \frac{A_0}{2}\mathrm{e}^{i(k_xx+k_yy-\omega t+\theta)} + c.c = A_0\cos(k_xx+k_yy-\omega t+\theta)$$

is defined as

$$E_{Total} = \rho g \int_{-\infty}^{\infty} \int_{-\infty}^{\infty} F(k_x, k_y) \mathrm{d}k_x \mathrm{d}k_y = \rho g \frac{A_0^2}{2}. \tag{3.5}$$

The relation (3.5), in turn, allows us to define the spectrum as the squared absolute value of the Fourier transform of the process.

In order to describe a relatively realistic ocean wave field, we designate the Fourier transform of the autocorrelation function $F(\mathbf{k})$ of surface elevations as our initial spectrum in the following form

$$F(\mathbf{k}) = F(k, \theta) = S(k)\, D(\theta), \tag{3.6}$$

where k and θ are the polar coordinates of (k_x, k_y). For $S(k)$ we utilize the JONSWAP spectrum from the Joint North Sea Wave Atmosphere Project

$$S(k) = \frac{\alpha\, k_p^2\, H_s^2}{2\, k^4} \exp\left(-\frac{5}{4} \left(\frac{k_p}{k} \right)^2 \right) \gamma^{\exp\left(-(\sqrt{k/k_p} - 1)^2 / (2\sigma_A^2) \right)}. \tag{3.7}$$

Once again, k_p is the peak wavenumber obtained through linear dispersion relation $\omega_p^2 = g k_p \tanh(k_p h)$, the coefficient γ is known as the peak enhancement, while the parameter σ_A has the values

$$\begin{cases} \sigma_A \;=\; 0.07 & \text{if} \quad k < k_p \\ \sigma_A \;=\; 0.09 & \text{if} \quad k > k_p. \end{cases}$$

Note that from $S(\omega)\mathrm{d}\omega\, \mathrm{d}\theta = S(k) k\, \mathrm{d}k\, \mathrm{d}\theta$ and the linearized dispersion relation one can transform the wavenumber spectrum (3.7) into a frequency spectrum via

$$S(k) \;\equiv\; \frac{S\left(\omega(k)\right)}{k} \frac{\mathrm{d}\omega}{\mathrm{d}k}.$$

In addition, the dimensional parameter α, known as the Phillips parameter, was taken to be 5/16. Similarly, based on the relatively narrow spectral bandwidth (Ochi 2005),

we can define the wave steepness as the product of twice the standard deviation and the peak wavenumber ($\epsilon = 2k_p\sigma$), where

$$\sigma = \left(\iint k\, F(k,\theta)\, dk\, d\theta \right)^{\frac{1}{2}} \tag{3.8}$$

is the standard deviation. Note, however, that the above definition of the wave steepness is $\sqrt{2}$ larger than that of Socquet-Juglard et al. (2005). For the directional distribution function $D(\theta)$ the following form was used (see Figure 3.3)

$$D(\theta) = \begin{cases} \frac{1}{\beta}\cos^2\left(\frac{\pi\theta}{2\beta}\right) & \text{if} \quad |\theta| \leq \beta \\ 0 & \text{if} \quad |\theta| > \beta. \end{cases} \tag{3.9}$$

For the purpose of illustration, Figure 3.1 shows few realizations of the JONSWAP spectra $S(k)$, for an array of different initial parameters, corresponding the four different cases in Table 3.1.

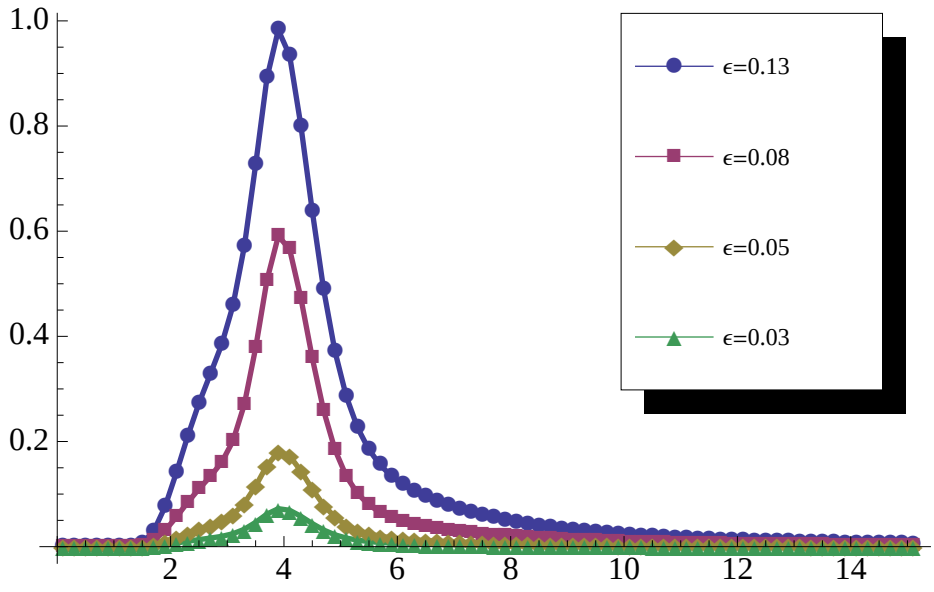

Figure 3.1 Plots of four different initial JONSWAP spectra $S(k)$ for varying parameters: $\gamma = (3.3, 5.0)$, $\epsilon = (0.03, 0.05, 0.08, 0.13)$, corresponding to initial data given in Table 3.1 and scaled by the maximum value.

3.2 Numerical Method

For the numerical method of our Fully and Weakly 2D models we wrote a Fourier pseudo-spectral method, where the surface elevation (ζ) and the velocity potential (Φ) are given by

$$\zeta(x,y,t) \;=\; \sum_{m=-\frac{N_x}{2}}^{\frac{N_x}{2}} \sum_{n=-\frac{N_y}{2}}^{\frac{N_y}{2}} a_{mn}(t)\, \mathrm{e}^{\mathrm{i}(m\Delta k_x\, x + n\Delta k_y\, y)}, \tag{3.10}$$

$$\Phi(x,y,z=\zeta,t) \;=\; \sum_{m=-\frac{N_x}{2}}^{\frac{N_x}{2}} \sum_{n=-\frac{N_y}{2}}^{\frac{N_y}{2}} b_{mn}(t)\, \mathrm{e}^{\mathrm{i}(m\Delta k_x\, x + n\Delta k_y\, y)}, \tag{3.11}$$

similar to the one used by Lo and Mei (1987).

Spectral methods are one of the major three numerical techniques for solving partial differential equations (PDEs), alongside the finite difference and finite element methods. In the 1970s, the transformation of the field was brought about Orszag and others with their work on fluid dynamics and meteorology and spectral methods became rather famous. Historically, the major precursor to this surge of interest in the spectral methods in the 1970s, was the re-introduction and numerical implementation of the Fast Fourier Transform (FFT) in 1965 by J. W. Cooley and J. W. Tukey. The algorithm and its recursive nature was actually invented by Carl Friedrich Gauss around 1805, who applied it to interpolation of asteroid trajectories. The main achievement of the FFT was the fact that it takes $O(N \log N)$, rather than $O(N^2)$ number of floating point operations to carry out a matrix multiplication in the standard discrete Fourier transform (DFT). Furthermore, if a solution of PDE is needed to a high level of accuracy and if the data defining the problem are smooth, then spectral methods are usually ideal. The reason behind this application is that smooth functions change slowly and since high wavenumbers correspond to short

waves and rapid oscillations, such functions therefore contain little energy in their spectral tail (at the high wavenumbers).

Moreover, if the Fourier transform of a function decays rapidly, then the errors introduced by numerical discretization will in turn be small. This is primarily because these errors are caused by this so-called aliasing of the high wavenumbers to low wavenumbers. This aliasing is a simple consequence of finite discretization of the domain and the periodic nature of the basis functions. In other words, functions on a discrete domain $x \in [x_1, x_2, ..., x_n]$, like for example $sin(2\pi k x_j)$ or $\exp[i\pi k x_j]$, will have an infinite family of "aliases" that are equal to them and are separated by integer values.

In contrast to finite difference or finite element methods, the spectral methods often gain several orders of accuracy within a similar time frame and dedicated computational resources. The Fourier pseudo-spectral method applied in our simulations requires periodic boundary conditions in both horizontal directions. If one desires different boundary conditions for their numerical simulations, such as Dirichlet or Neumann, then different basis functions (such as Chebyshev) have to be employed. Nevertheless, the FFT can still be used to accommodate the Fourier transform with Chebyshev basis.

As noted earlier, the value of the standard deviation σ in (3.8) is appropriately chosen through the input parameters so the wave steepness (ϵ) has a desired value and in the case of numerical simulation discussed next, its values are $\epsilon = 0.03, 0.05, 0.08,$ and 0.13 (see Table 3.1). In addition, Table 3.1 contains another parameter called the Benjamin-Feir Index (BFI), which is defined as the ration of the wave steepness (ϵ) to the relative spectral bandwidth $\Delta\omega/\omega_p \sim \Delta k/2k_p$. Where $\Delta\omega$ and Δk are the measures of the width of frequency and wavenumber spectrum, respectively. These widths were measured at the point where the one-half of the maximum/peak of the spectrum occurred. It should be pointed out that BFI is treated as an indicator for

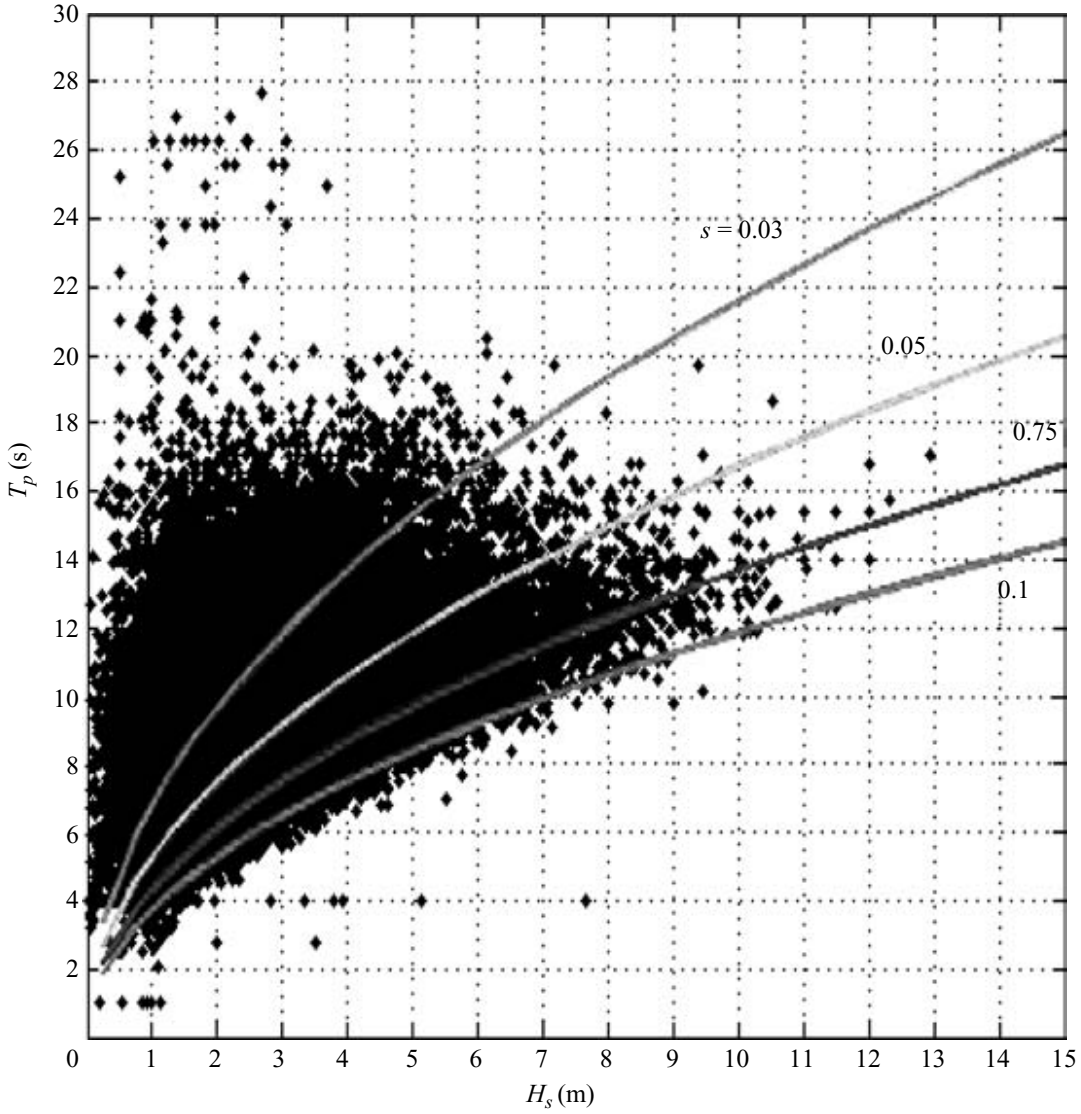

Figure 3.2 Recordings of wave heights from the North Sea, taken over the span of 28 years in the intervals of 20 minutes. Lines of constant wave steepness (ϵ) are superimposed. Plot taken from Socquet-Juglard et al. (2005) – with permission from Karsten Trulsen.

the relative degree of nonlinearity. In other words, when BFI>1, this indicates that the wave field is highly nonlinear, while BFI<1 describes a weakly nonlinear wave field. Also, note that the case of $\epsilon = 0.1$ is a rather extreme end of the spectrum, as it is illustrated in Figure 3.2 (extracted from Socquet-Juglard et al. (2005) with permission from Karsten Trulsen). It represents recordings of wave heights over the period of 28 years taken within intervals of 20 minutes in the North Sea. The lines of constant steepness are superimposed showing that the steepness of $\epsilon = 0.1$ is indeed an extreme end of the spectrum.

Aside of the required periodic boundary conditions and in order to minimize the computational burden of ensemble averaged simulations, the initial spatial grid was comprised (after padding) of

$$(N_x,\, N_y) = (512,\, 256)$$

Fourier modes, where we padded half of the modes with zero-pad-filter in order to avoid aliasing. The choice of the zero-pad filter region is based on the order of the nonlinearity (m) and is given by $(m+1)/2$. Therefore, since we are dealing with the cubic nonlinearities $(m = 3)$, we needed to double the number of Fourier modes, thus essentially we padded half of the Fourier modes with zeros. The numerical computations for both, Fully and Weakly 2D models, were initialized in Fourier space via the square root of the autocorrelation function of surface elevations $F(\mathbf{k})$ with random phases

$$\mathcal{F}[\zeta(x,y,t=0)] = \hat{\zeta}(k_x,k_y,t=0) = \sqrt{2\,F(\mathbf{k}_{mn})\,\Delta k_x\,\Delta k_y}\,\mathrm{e}^{\imath\theta_{mn}}, \tag{3.12}$$

where $F(\mathbf{k}_{mn})$ is given by (3.6) and the random phases θ_{mn} were uniformly distributed over a 2π domain, with the wavenumber vector being defined as

$$\mathbf{k}_{mn} = (m\,\Delta k_x\,, n\,\Delta k_y) \quad \text{with} \quad \Delta k_x = 1/512 \quad \text{and} \quad \Delta k_y = 1/256.$$

Therefore, the corresponding spatial resolution/discretization in physical space is

$$\Delta x = 2\pi/(N_x\,\Delta k_x) \quad \text{and} \quad \Delta y = 2\pi/(N_y\,\Delta k_y).$$

We employed about 30 characteristic wavelengths ($\lambda_p = 2\pi/k_p$) in each horizontal direction, with characteristic wave period of 1 sec. This implies that the horizontal domain had dimensions of about $L_x = L_y \sim 46$ meters. It should also be noted that, although in realistic ocean wave fields the characteristic wave period is between 6 to 16 seconds, we can certainly (without a loss of generality) scale the system to accommodate our characteristic wave period of 1 sec.

Finally, the numerical codes were written in FORTRAN 90 and were parallelized with the use of the Message Passing Interface (MPI) library/paradigm, to allow for multiprocessor and multicore computations with high performance computing (HPC) machines, such as Hydra at NJIT (New Jersey Institute of Technology) or Dolphin at KAIST (Korean Advanced Institute of Science and Technology). The Dolphin in KAIST is a brand new IBM 256 core HPC cluster with Infiniband interconnects. For our simulations we used a set time step of $\Delta t = 10^{-3}$ and we normally achieved the following time results under an intermediate cluster load:

$$\textbf{Fully 2D} \begin{cases} 32 \text{ processor cores } \rightarrow\ 4.48 \times 10^{-2} \text{ sec per time step} \\ 64 \text{ processor cores } \rightarrow\ 3.56 \times 10^{-2} \text{ sec per time step,} \end{cases}$$

$$\textbf{Weakly 2D} \begin{cases} 32 \text{ processor cores } \rightarrow\ 3.58 \times 10^{-2} \text{ sec per time step} \\ 64 \text{ processor cores } \rightarrow\ 2.71 \times 10^{-2} \text{ sec per time step.} \end{cases}$$

To put this in perspective, a case of one set of parameters of the Fully 2D model for 100 ensemble averaged simulations up to 150 peak periods (150 sec), with a fixed time step of $\Delta t = 10^{-3}$ and using 32 dedicated processor cores, it took about 8 days to complete the simulation. In contrast, for a single simulation on 32 processors cores

up to 150 peak periods with the same time step, but with $[2048 \times 1024]$ Fourier modes (after padding), it takes about 30 days to complete this one simulation.

In reality, due to the limits on the computational resources and the fact that the HPC queue was a shared system, we were often limited to using only 16 cores for a single job. Hence, a large number of our simulations were carried out on 16 cores each. Nonetheless, the use of parallel computing in our case is literally indispensable. Without these resources and tools, it would probably take another few years to complete all of these simulations on a single processor machine, despite the fact that we still kept the number of Fourier modes at fairly modest level ($N_x = 512, N_y = 256$).

It should be noted though, that these results were obtained without optimizing the FFT for the Weakly 2D model. In other words, we mentioned before that because of only two terms with transverse dependence appearing in the Weakly 2D model (2.14)-(2.15), we can cut down the time and operation count of carrying out a single 2D FFT for all other terms (without transverse dependence – k_y) by 50%. That is, we can simply apply 1D FFT along the x-direction for every single instance of y, without subsequently having to transpose the matrix and applying additional 1D FFT along y-direction for every single x. Therefore, it is expected that if these optimizations would be implemented, thus also eliminating the need of transposing the matrix to carry out the second part of the 2D FFT, the computational times for the Weakly 2D model, given above, would reduce by at least 50%.

Nevertheless, we cannot expect to monotonically decrease the computational time with continuous increase of the dedicated processor cores, because of the plateau effect. In other words, since the MPI (Message Passing Interface) library and the FFT requires a hefty amount of communication between various nodes/cores at every time step, we would expect that the communication overhead would eventually take longer than a single computation per time step. The exact place of the plateau is of course dictated by the HPC architecture and is also code dependent. In fact, in some of

our early simulations we observed very little gain in computational speed when we increased from 64 to 128 dedicated processor cores. Hence, we were almost plateauing and we can pretty much assume that once we increase to 256 processor cores, our simulations would take longer than those for 128 cores.

Consequently, our initial surface wave fields were initialized by taking a two-dimensional discrete fast Fourier transform (FFT) of (3.12). Upon taking a two-dimensional FFT in space, we solve for temporal evolution via fourth order Runge-Kutta method with, as mentioned before, a set time step of

$$\Delta t = 10^{-3},$$

which conserves all of the corresponding conserved quantities such as: mass, momentum, and energy to a very high degree of accuracy. For instance, in the case of widest initial directional distribution of $\beta = 0.7$ and wave steepness $\epsilon = 0.13$, after 150 wave periods (150 sec) the energy was conserved on the order of 10^{-4} of a percent. We carried out both, single deterministic and multiple Monte-Carlo simulations averaged over 100 and in some cases 200 runs. Furthermore, in order to see appreciable evolution of the spectra and to manage the computational burden in our averaged Monte-Carlo simulations, we chose the final time to be on the order of $150\,T_p$, where T_p is the peak wave period - taken here to be 1 sec. Note that, based on nonlinear four-wave interaction theory of Pushkarev et al. (2003), the time scale for the onset of nonlinear four-wave interaction is inversely proportional to fourth power of wave steepness (ϵ^4). We also present few results for 100 averaged simulations carried out for 900 peak periods (900 sec).

Table 3.1 JONSWAP spectrum — Initial Input and Numerical Simulation Parameters. β is the Initial Directional Distribution Parameter. γ is the Peak Enhancement, k_p is the Peak Wavenumber, λ_p is the Peak Wavelength, T_p is the Characteristic (Peak) Wave Period (1 sec), ϵ is the Wave Steepness, $\bar{a}$ is the Characteristic Wave Amplitude, and $Time$ Represents the Physical Duration of the Simulations (in sec), While $\#\ of\ Runs$ Gives the Total Number of Ensemble Averaged Random Monte-Carlo Simulations for the Given Set of Parameters. BFI is the Benjamin-Feir Index Defined as the Ratio of the Wave Steepness ϵ to the Relative Spectral Bandwidth $\Delta\omega/\omega_p \sim \Delta k/2k_p$. The Spectral Bandwidth Δk is Defined as the Width of the Spectrum at the Half-Height of the Peak Frequency or Wavenumber.

β	γ	$k_p(m^{-1})$	$\lambda_p = 2\pi/k_p(m)$	$T_p(sec)$	$H_s(m)$	$\epsilon = k_p\bar{a}$	Δk	BFI	$Time\ (sec)$	$\#\ of\ Runs$
0.14	5.0	4.02	1.56	1	0.0114	0.03	1.35	0.18	150	100
0.35	5.0	4.02	1.56	1	0.0180	0.05	1.35	0.29	150	200
0.35	3.3	4.02	1.56	1	0.0326	0.08	1.52	0.42	150	100
0.7	3.3	4.02	1.56	1	0.0326	0.08	1.52	0.42	150	200
0.7	3.3	4.02	1.56	1	0.0515	0.13	1.52	0.69	150 & 900	100 & 100

Also, wanting to study the influence of the directional spreading of the spectrum on the evolution of the wave field, especially in the context of extreme waves, we chose three different cases of initial directional distribution for (3.9). Similar cases of directional distributions were also examined by Socquet-Juglard et al. (2005). However, their simulations were carried out exclusively for the set wave steepness of $\epsilon = 0.1$. The above mentioned three cases of directional distribution (3.9) are the following

$$\begin{cases} Case\ (1) & \beta = 0.14 & \gamma = 5.0 \\ Case\ (2) & \beta = 0.35 & \gamma = 5.0 \\ \quad and & \beta = 0.35 & \gamma = 3.3 \\ Case\ (3) & \beta = 0.7 & \gamma = 3.3. \end{cases}$$

Also, we note that the case for $\beta = 0.7$ gives a wider initial mean directional spreading

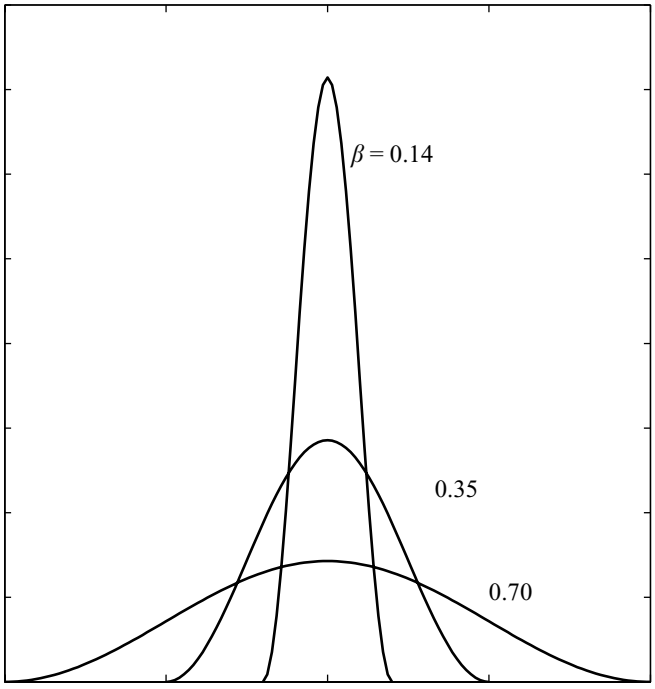

Figure 3.3 Three different cases of directional distribution function $D(\theta)$ defined by equation (3.9).

(defined in the next chapter), than the widest case of directional spreading ($N = 24$) used by Toffoli et al. (2010). In their work, Toffoli and collaborators compared the simulations of the higher order spectral method (HOSM) of West et al. (1987) and the broader modified nonlinear Schrödinger (BMNLS) equation of Trulsen and Dysthe (1996) to a series of experimental data. They have also carried out simulations based on the JONSWAP spectrum with different initial directional distributions and 100 averaged simulation, but only up to 60 peak periods (60 sec). Most of the correlations have been performed in the statistical setting of the third and fourth moment (skewness and kurtosis), with the usual results of a decreasing kurtosis when the directional distribution broadened. The skewness and kurtosis of the surface elevations is defined as

$$\begin{cases} M_3(\zeta) = \sum_{j=1}^{N} \frac{(\zeta_j - \bar{\zeta})^3}{N} & \Longrightarrow \quad \text{Skewness :} \quad \mathrm{m}_3(\zeta) \equiv \frac{\mathrm{M}_3}{\sigma^3} \\ M_4(\zeta) = \sum_{j=1}^{N} \frac{(\zeta_j - \bar{\zeta})^4}{N} & \Longrightarrow \quad \text{Kurtosis :} \quad \mathrm{m}_4(\zeta) \equiv \frac{\mathrm{M}_4}{\sigma^4}, \end{cases} \tag{3.13}$$

where σ is the standard deviation of the surface wave field. Also it should be noted that Toffoli and collaborators, have performed only four (4) experiments and both of the numerical models were being compared to them. This seeming low number of experiments might be the reason behind their findings, that the BMNLS was behaving the least well for the case of narrow directional distribution — where in theory it should have behaved the best.

CHAPTER 4

RESULTS OF NUMERICAL SIMULATIONS (SINGLE AND ENSEMBLE AVERAGES)

This chapter presents the results and analysis of the numerical simulations. The following two sections compare the simulations between the Fully 2D and Weakly 2D models, as well as the Fully 2D and the MNLS, respectively. Aside of direct surface-to-surface wave profile comparisons, we elected to carry out ensemble averaging of the spectra. As it was mentioned in the previous chapters, the ensemble averaging has been employed to give credibility to our random simulations, especially due to the lack of any direct experimental data that these models could be compared with.

Moreover, due to spatial discretization of initially smooth JONSWAP spectrum, after one single simulation the spectrum becomes uneven and loses all of its original smoothness. The averaging over 100 simulations allows us, in turn, to smooth out the spectrum in order to be able to clearly distinguish the level curves in the density plots. In contrast, Dysthe et al. (2003), who compared MNLS with a cubic NLS for an initially Gaussian spectrum, have not only averaged their randomly initialized spectra over 20 simulations (in 2D), but have also smoothed it out with a so-called "moving average" by using a Gaussian with appropriately chosen standard deviation. They also argue that the spectrum reaches a quasi-steady-state within few (20 or so) periods (1 period = 1 sec). We, on the other hand, do not believe that smoothing out the spectrum with the help of a moving average is a reliable method and in our simulations, we resort only to ensemble averaging to support this quasi-steady-state.

Socquet-Juglard et al. (2005), who simulated MNLS with an initial JONSWAP spectrum and used a Fourier pseudo-spectral method similar to ours, have employed a rather peculiar circular zero-pad de-aliasing filter, centered around the peak of the

spectrum, with a radius equal to the distance (or rather a number of Fourier modes) from zero to the peak wavenumber (k_p). The physical aspect and the validity of this filter, as well as the amount of energy that is initially cut off, still needs further investigation.

Also, we would like to point out the work of Tanaka (2007), where he simulated the evolution of the JONSWAP spectrum under the action of both, the HOSM (Higher Order Spectral Method) of West et al. (1987) and the Zakharov equation (1968), with an unusually large number of Fourier modes. Mainly, in his Fourier pseudo-spectral method, he used as many as $(N_x, N_y) = (4096, 2048)$ Fourier modes and showed that in such fine discretization of the wave field, the spectrum for a single simulation remained not only incredibly smooth, but also the downshifting of the spectral peak was almost nonexistent – even up to the time of 100 peak periods. These results, as far as we are concerned, were not reproduced by anyone yet, but it is worth adding that they contradict the last two decades of numerical results for the simulation of evolving weakly nonlinear ocean surface waves.

It should perhaps be pointed out that, in all of the above mentioned simulations, as well as the ones discussed below, the simulated models do not account for any atmospheric pressure fluctuations or wind forcing and cannot topologically accommodate wave breaking – where wave breaking is commonly believed to enhance the downshifting of the spectral peak (Babanin et al. 2010). Therefore, the waves are fully developed and the only mechanism for the evolution of the spectrum in time, has to be the nonlinear energy transfer from the nonlinear mode coupling – at least in the initial transient phase of the evolution.

4.1 Comparison Between Fully 2D and Weakly 2D Models

In this section we compare the results of the numerical simulations of our Fully and Weakly 2D models. Since the Weakly 2D model was derived with an additional

assumption of weak transverse dependence, it was expected that the simulations with small initial directional distribution β in (3.9) would yield both good qualitative and quantitative agreements. In Figure 4.1 we show the spectrum at $t = 0\,sec$ (left column) and at $t = 150T_p = 150\,sec$ (right column) for the first case of directional distribution (3.9) with $\beta = 0.14$ and wave steepness of $\epsilon = 0.03$. The top row corresponds to the Fully 2D model, while in the bottom row we have the Weakly 2D model. Also, the crossing of the two vertical and horizontal black marker lines corresponds to the location of the initial spectral peak. As expected, the spectra of both models appears to be almost indistinguishable. Nevertheless, it shows a slight downshifting of the spectral peak attributed to the generation of both bound and free waves. Free waves, are simply the waves that obey the dispersion relation of the given dispersive problem.

Similarly, in Figure 4.2 we also show the spectrum at $t = 0\,sec$ (left column) and at $t = 150\,sec$ (right column) for the second case of directional distribution (3.9) with $\beta = 0.35$ and wave steepness of $\epsilon = 0.05$. Once again, an excellent quantitative agreement between the two models is achieved. Moreover, the downshifting of the spectral peak, commonly attributed to modulation (Benjamin-Feir) instability and the nonlinear energy transfer, is becoming more evident. In other words, as β increased, we observed that the spectral peak downshifting was more pronounced in the given time frame of computation. Hence, the findings of Waseda et al. (2009b) that the rate of spectral downshifting is a monotonically decreasing function of the directional distribution (β), are also supported here. Though it should be noted that as our initial directional distribution is broadened, the nonlinearity (ϵ) is also being increased.

In contrast, in Figure 4.3 the spectrum at $t = 0\,sec$ (left column) and at $t = 150\,sec$ (right column) for the third case of directional distribution (3.9) with $\beta = 0.7$ and wave steepness of $\epsilon = 0.08$ is shown. In this case, the downshifting of the spectral

peak is even more pronounced than in the previous two cases. Also, upon more detailed observation, we notice that the spectrum appears to start cascading its energy along the branches of the so-called figure-8 of McLean et al. (1981). Moreover, the head (or nose) of the spectrum in the three different cases of directional distribution and steepness, is topologically different. In other words, it transforms from being concave for the case of $\beta = (0.14, 0.35)$, to a convex structure in the final case of $\beta = 0.7$. Finally, the tail of the spectrum between Weakly 2D and Fully 2D models is qualitatively different. This is also the case of for $\beta = 0.7$ and $\epsilon = 0.13$ (see Figure 4.5). Interestingly enough, when we retain the steepness of $\epsilon = 0.08$, but we downgrade the directional distribution to $\beta = 0.35$, we no longer notice the significant difference in the spectral tail. In other words, the tails of spectra between Fully 2D and Weakly 2D models have similar curvatures. We ultimately believe that this difference in the qualitative nature of the spectral tail is brought about the asymptotic limitations of the Weakly 2D model. Mainly, in the areas (corners) where the Weakly 2D spectrum (at t=150 sec) does not have the same curvature as the Fully 2D model, the ratio k_y/k_x, originally assumed to be of order of the wave steepness (ϵ), is no longer small and is about 2/3.

A natural question one may ask is – how do we ascertain that 100 simulation average is sufficient. In Figure 4.6, we show the standard deviation of the ensemble averaged spectra for 10, 20, 30, ... , 100, ... , 200 simulations for $\beta = 0.7$, $\epsilon = 0.8$ (left column) and $\epsilon = 0.13$ (right column) against the mean of 200 and 100 simulations, respectively. The corresponding standard deviations are clearly converging around 100 simulations (even for the extreme case of $\epsilon = 0.13$). To quantify in more detail the differences in spectral spreading of the Fully and Weakly 2D models, we define the mean directional spread function of Toffoli et al. (2010) and Hwang et al. (2000)

$$\sigma_m(k) = \left(\frac{\int_0^{\pi/2} \theta^2 F(k,\theta) \mathrm{d}\theta}{\int_0^{\pi/2} F(k,\theta) \mathrm{d}\theta} \right)^{1/2}, \tag{4.1}$$

where hereafter $\sigma_m(k)$ will be averaged over the wavenumber k and referred to as σ_m. The comparisons between the two models for $\beta = 0.14$ are nearly identical and for $\beta = 0.35$ the Weakly 2D model has a slightly higher mean directional spread than that of the Fully 2D model. Hence, in Figures 4.7-4.8 we only plot the mean spreading function of $\beta = 0.7$ for $\epsilon = 0.08$ (left) and $\epsilon = 0.13$ (right) that show appreciable differences. Furthermore, in all different cases of initial directional distribution there appears to be suggestive evidence for the existence of a quasi-steady-state of the mean directional spreading function towards the end of the simulation ($Final\ Time = 150\ Peak\ Periods \equiv 150$ sec). In Figure 4.9, we show the mean spreading function for the time frame larger by a factor of six. Mainly, we carried out the 100 averaged simulations with the final time of 900 seconds and observed that suggested quasi-steady-state for the mean spectral spreading function is indeed justified.

Contrary to the results obtained by Clamond et al. (2006), in their numerical work Trulsen and Dysthe (1990) have observed that the downshifting of the spectral peak is permanent - even in the case of nonbreaking waves. In Figure 4.10, we show the persistence of the downshift of the spectral peak in our simulations. These were carried out for the duration of 900 peak periods (900 sec) and were averaged over 100 simulations. Also, the spectra were integrated along the angle θ, rather than just taking a cross section along the line of symmetry ($k_y = 0$). What is immediately apparent is that, the main downshifting of the spectral takes place during the first 600 peak periods (600 seconds) and the downshift between 600 and 900 seconds is minimal. Also, note that because the spectra were angularly integrated, the peak appears to be substantially rising. This is actually not the case, as the angularly integrated spectra account for the spreading. If one would to plot the spectra along the line of symmetry ($k_y = 0$), you would still observe the spectral downshifting, but the rise of the peak would normally not be observed in contrast to an angularly integrated spectra.

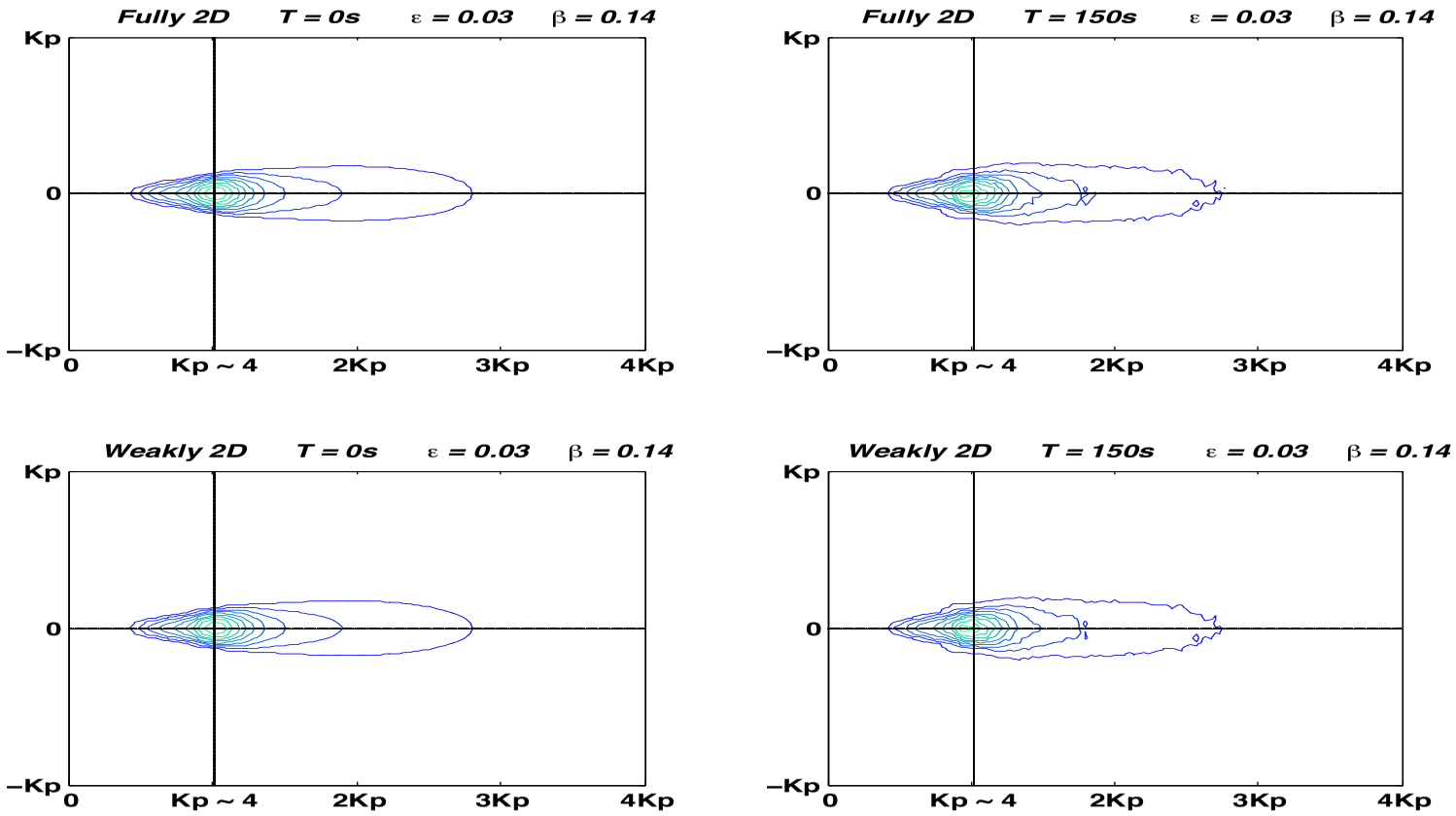

Figure 4.1 Case 1 – The evolution of the spectrum of initial directional distribution $\beta = 0.14$ (narrowest case) and wave steepness of $\epsilon = 0.03$. The left column given the initial density plot and the right column is the spectrum at 150 peak periods (150 sec), all averaged over 100 simulations. The top row corresponds to the Fully 2D model, while the bottom is the Weakly 2D model. The black crossing lines mark the spot of the initial spectral peak.

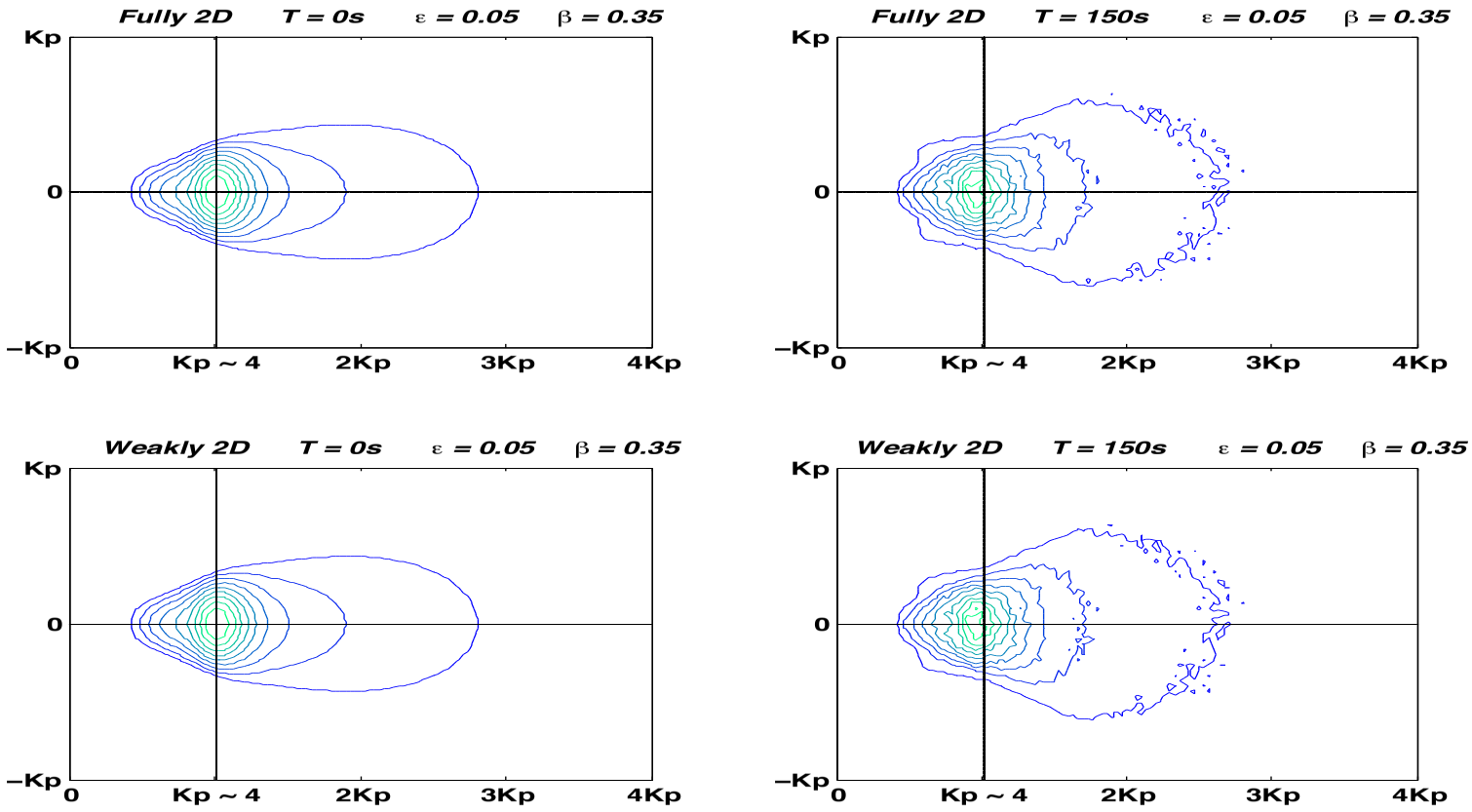

Figure 4.2 Case 2 – The evolution of the spectrum of initial directional distribution $\beta = 0.35$ (intermediate case) and wave steepness of $\epsilon = 0.05$. The left column given the initial density plot and the right column is the spectrum at 150 peak periods (150 sec), all averaged over 100 simulations. The top row corresponds to the Fully 2D model, while the bottom is the Weakly 2D model. The black crossing lines mark the spot of the initial spectral peak.

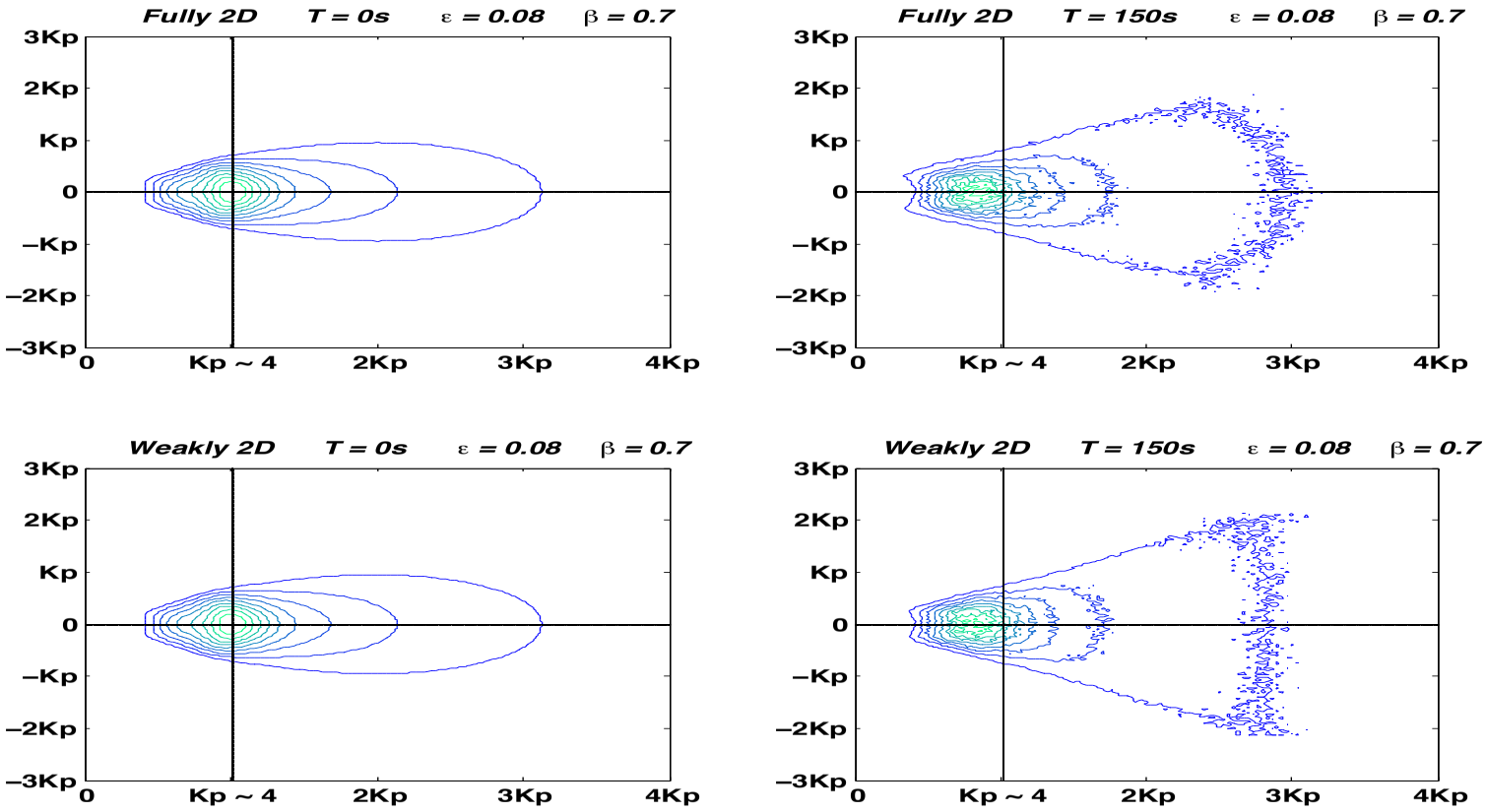

Figure 4.3 Case 3 – The evolution of the spectrum of initial directional distribution $\beta = 0.7$ (widest case) and wave steepness of $\epsilon = 0.08$. The left column given the initial density plot and the right column is the spectrum at 150 peak periods (150 sec), all averaged over 100 simulations. The top row corresponds to the Fully 2D model, while the bottom is the Weakly 2D model. The black crossing lines mark the spot of the initial spectral peak.

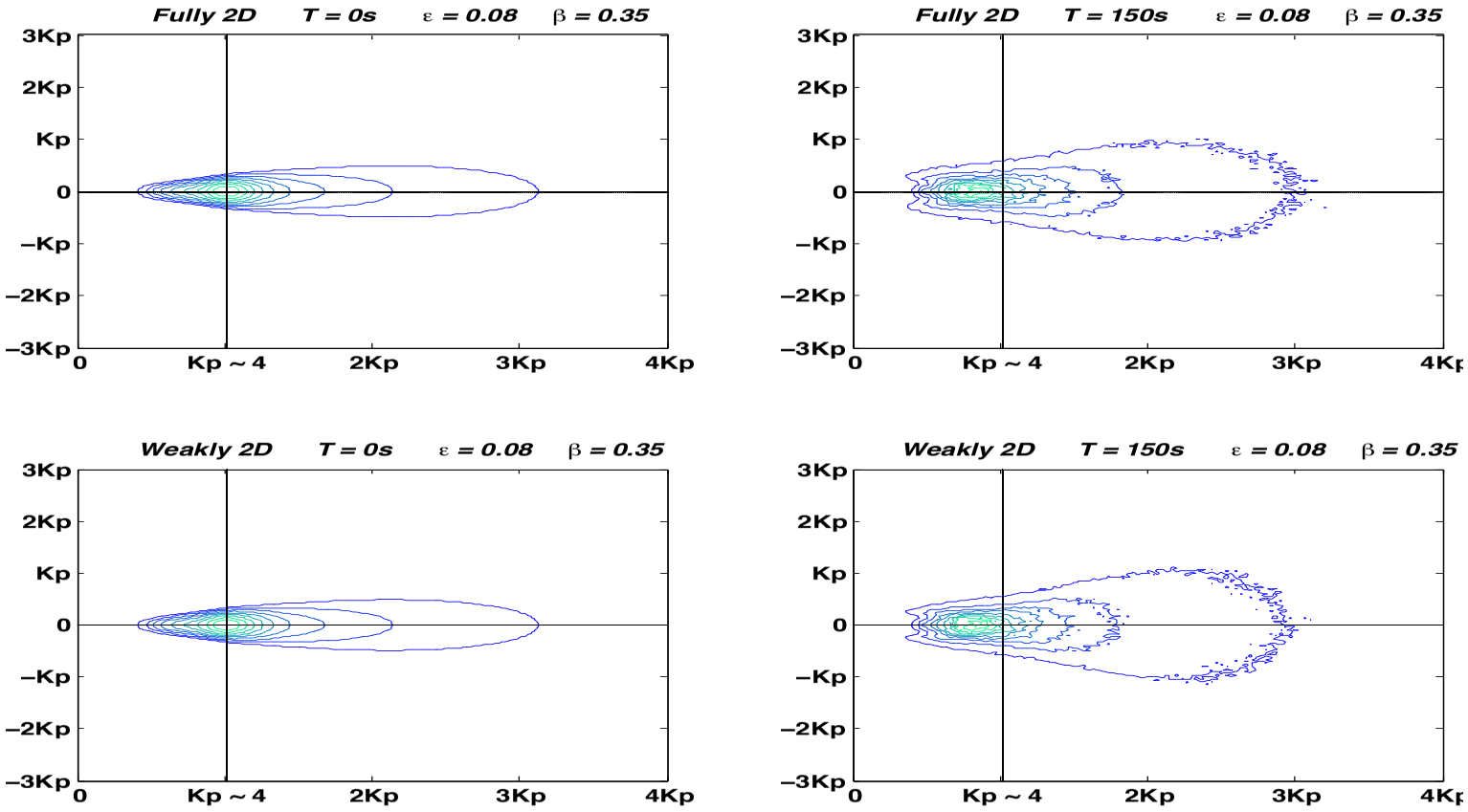

Figure 4.4 Auxiliary Case 3 – The evolution of the spectrum of initial directional distribution $\beta = 0.35$ and wave steepness of $\epsilon = 0.08$. The left column given the initial density plot and the right column is the spectrum at 150 peak periods (150 sec), all averaged over 100 simulations. The top row corresponds to the Fully 2D model, while the bottom is the Weakly 2D model. The black crossing lines mark the spot of the initial spectral peak.

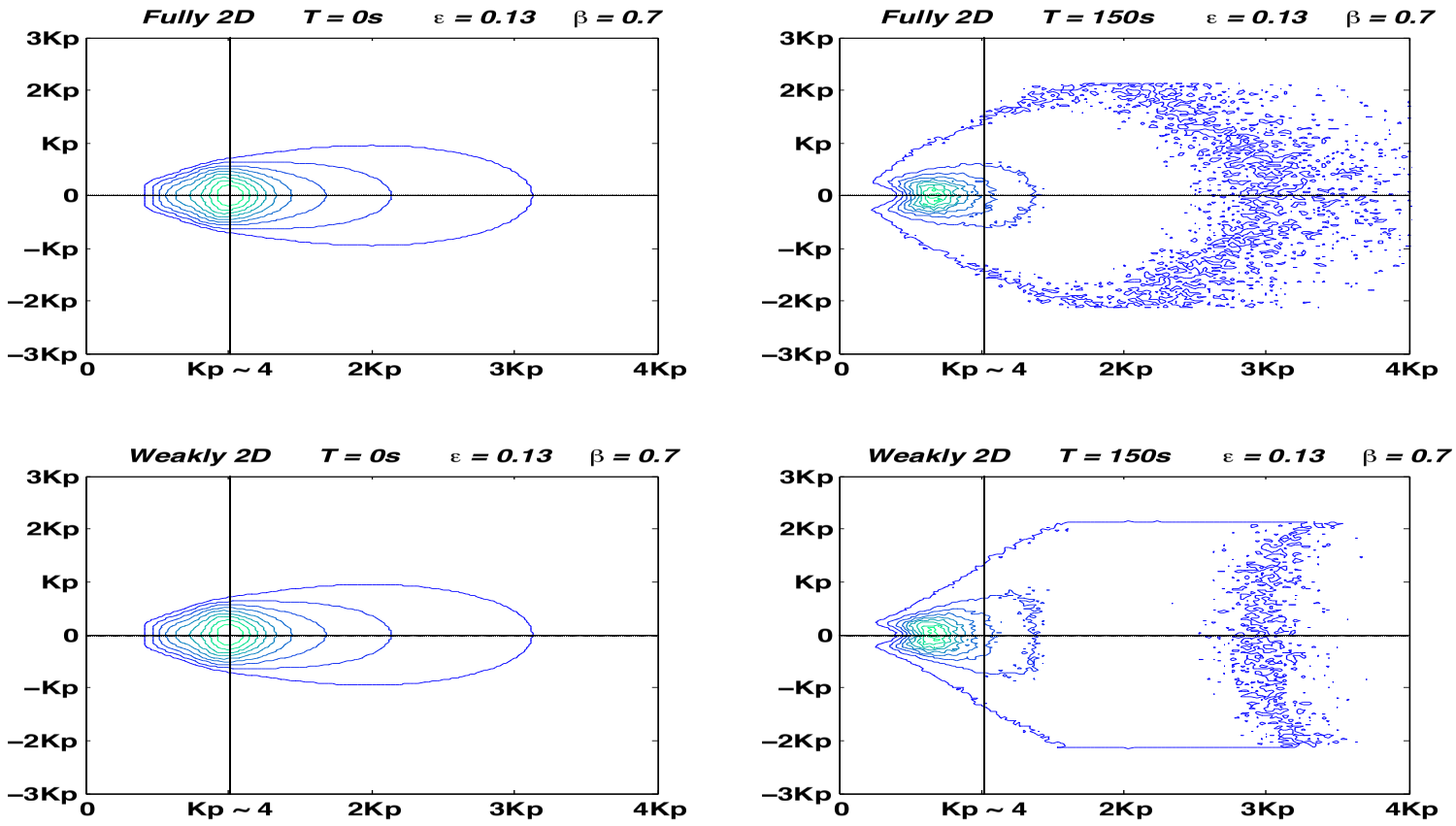

Figure 4.5 **Case 3** – with $\epsilon = 0.13$ – The evolution of the spectrum of initial directional distribution $\beta = 0.7$ (widest case) and wave steepness of $\epsilon = 0.13$. The left column given the initial density plot and the right column is the spectrum at 150 peak periods (150 sec), all averaged over 100 simulations. The top row corresponds to the Fully 2D model, while the bottom is the Weakly 2D model. The black crossing lines mark the spot of the initial spectral peak.

In fact, in Figure 4.11, we plot peak angular frequency ω_p versus time, along the line of symmetry ($k_y = 0$). The top row gives the plots of the location of the spectral peak frequency (ω_p) as the function of time, relative to the location of the initial spectral peak at $t = 0s$, for the Fully 2D (left) and Weakly 2D (right) models. While the bottom row shows the magnitude of the spectral peak frequency as a function of time, relative to the magnitude of the initial peak frequency (ω_p at $t = 0s$). Different degrees of directional distribution $\beta = 0.14, 0.35, 0.7$ and levels of wave steepness $\epsilon = 0.03, 0.05, 0.08, 0.13$ are also shown. The plots of the relative magnitude of the spectral peak are decreasing in time, but show an oscillatory decaying behavior. What is even more interesting, is that the location of the spectral peak frequency is also oscillating according to a well defined pattern. In other words, for the case of $\beta = 0.14$ and $\epsilon = 0.03$ the spectral peak upshifts and return to its original position for the first 100 peak periods (100 sec). While in the remaining 50 periods it upshift and downshift episodically. In turn, as we increase the directional distribution and wave steepness to $\beta = 0.35$ and $\epsilon = 0.05$, the spectral peak downshift and return to its original location, with an increasing level of downshifting around 80 periods. In contrast, for $\beta = 0.7$ and $\epsilon = 0.08$, we still observe downshifting with a retraction to an upshift, but it never return to the initial location of the peak. Finally, for the case of $\beta = 0.7$ and $\epsilon = 0.13$, the downshifting is even more pronounced, but the retracting upshift is never observed. In this case, the spectral peak appears to be sporadically stationary. To sum it all up, it should be rather obvious that as the initial spectral distribution (β) broadens and the wave steepness (ϵ) increases, the recurring upshifting and downshifting of the spectral peak is transformed into primarily a downshifting trend.

In Figures 4.12-4.19, we show angular dependence of the spectra under the action of both models (Fully 2D and Weakly 2D) at different values of angular wavenumber $k = \sqrt{k_x^2 + k_y^2}$, for all different cases of initial directional distribution

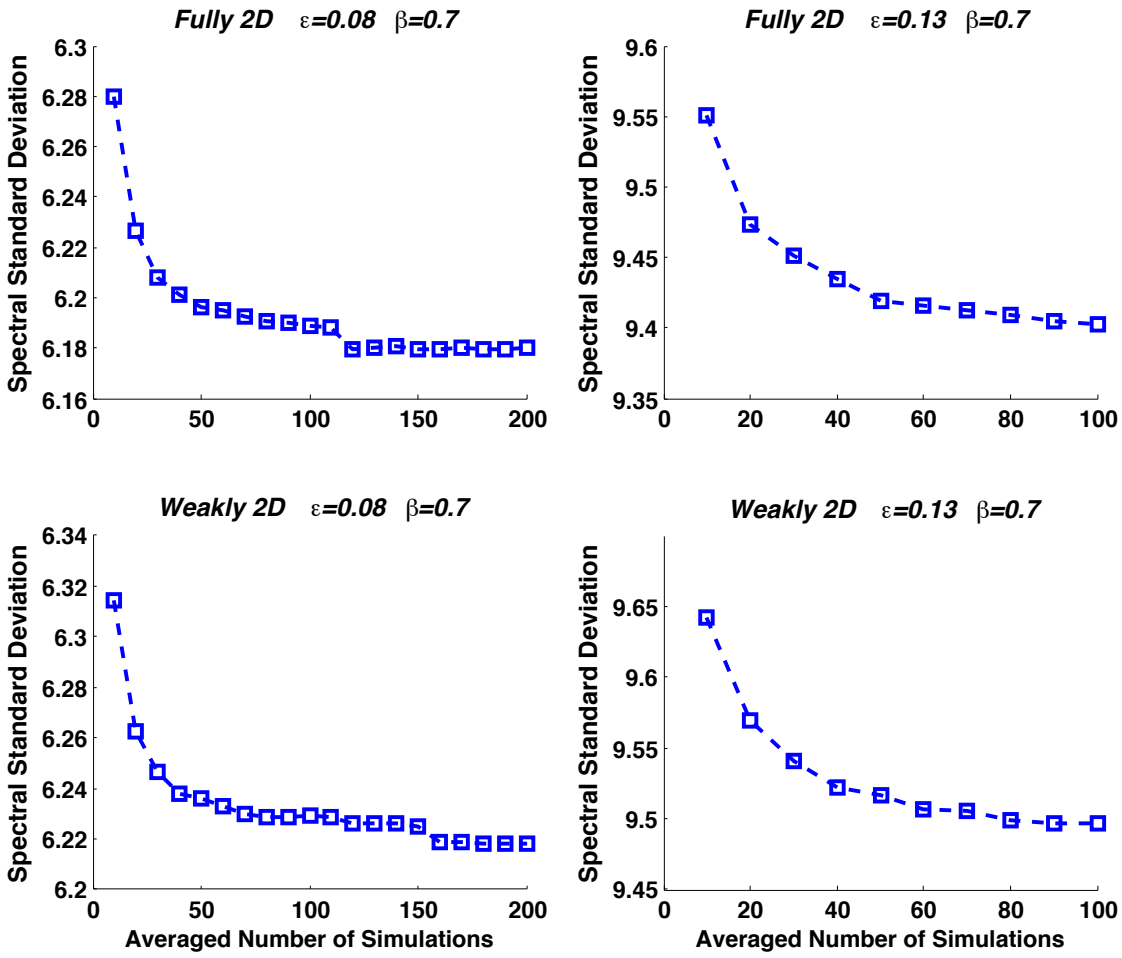

Figure 4.6 Standard deviation of the averaged spectral distribution. The left column represents $\epsilon = 0.8$ for up to 200 averaged simulations and the right column gives $\epsilon = 0.13$ for 100 averaged simulations, both for $\beta = 0.7$ directional spreading case of (3.9). Top row is for the Fully 2D model, while the bottom row is for the Weakly 2D model.

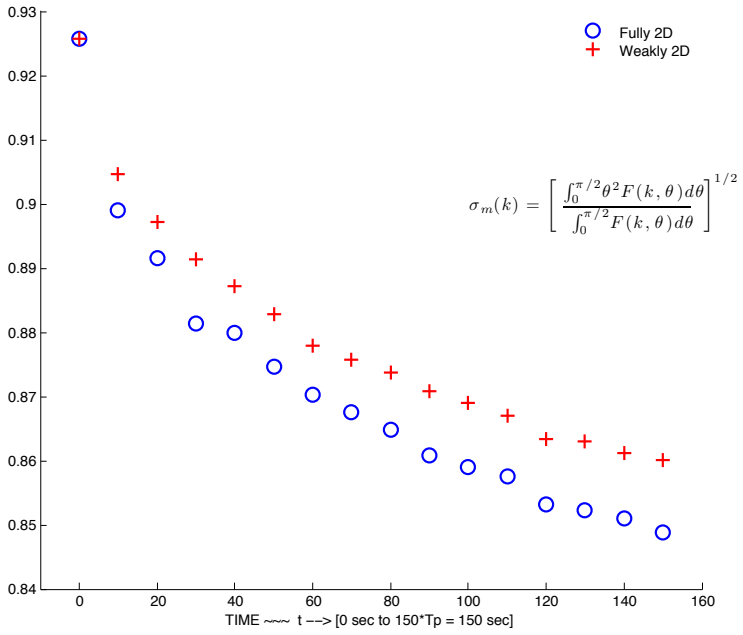

Figure 4.7 Mean Spreading Function of (4.1) for $\epsilon = 0.08$ wave steepness and $\beta = 0.7$ of directional spreading case of (3.9), averaged over 200 simulations.

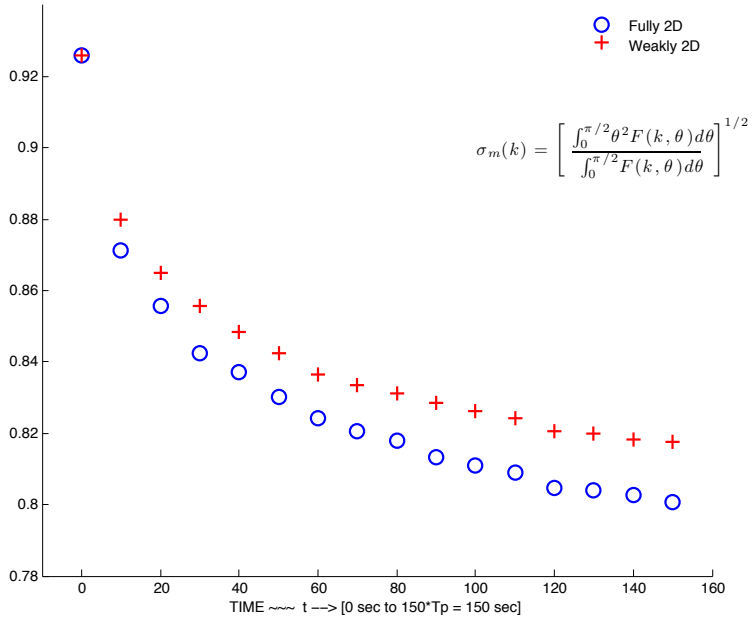

Figure 4.8 Mean Spreading Function of (4.1) for $\epsilon = 0.13$ wave steepness and $\beta = 0.7$ of directional spreading case of (3.9), averaged over 100 simulatioins.

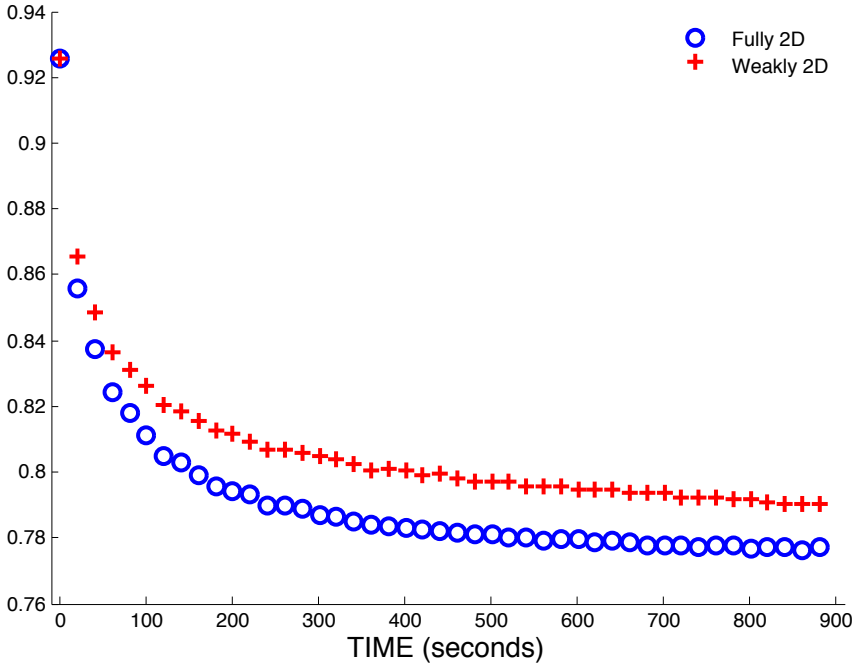

Figure 4.9 Mean Spreading Function of (4.1) for the final time of 900 seconds (900 peak periods). The wave steepness $\epsilon = 0.13$ and the initial directional spreading $\beta = 0.7$, averaged over 100 simulations.

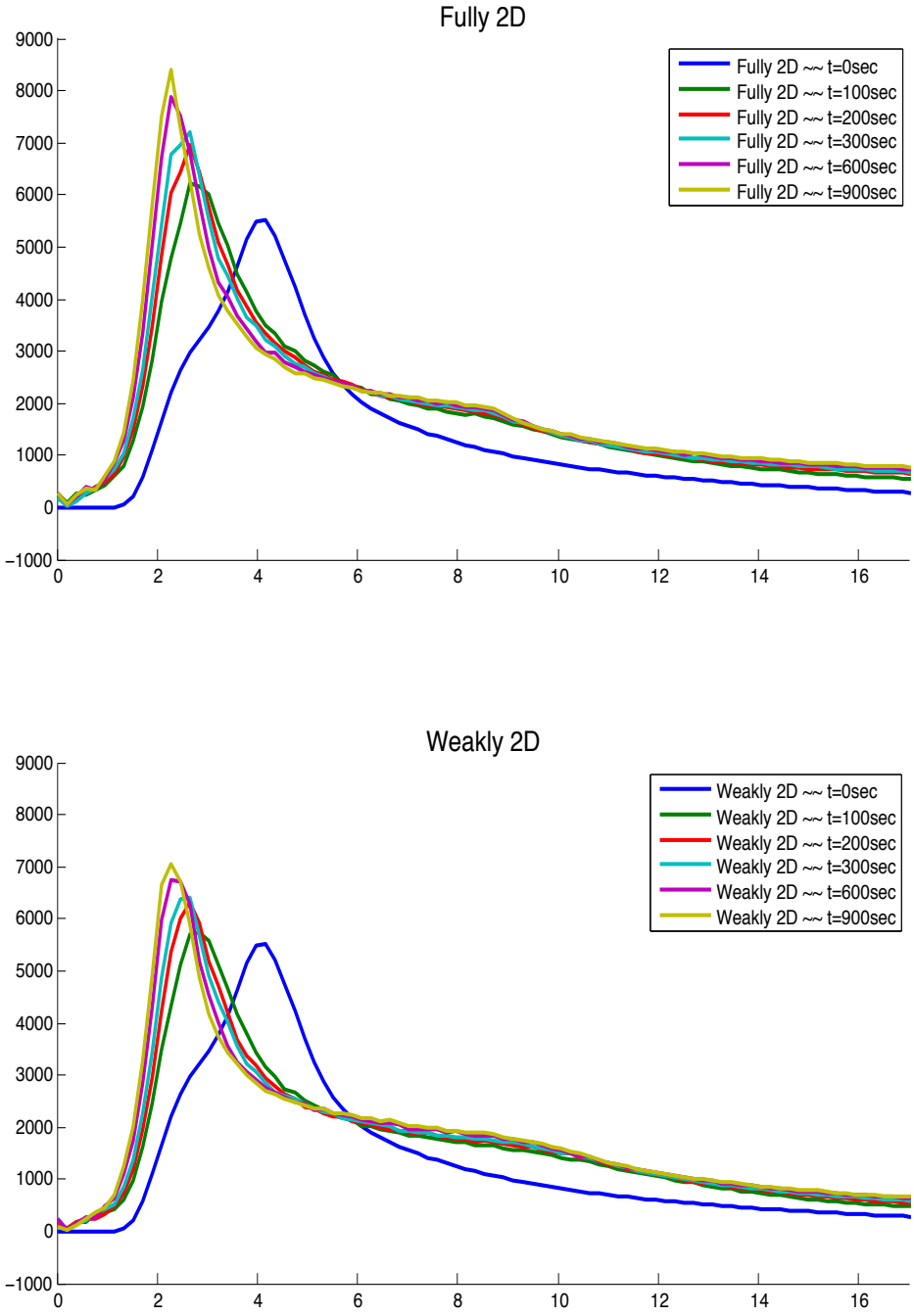

Figure 4.10 The downshifting of the spectral peak for the wave steepness $\epsilon = 0.13$ and the initial directional spreading $\beta = 0.7$. This spectra are averaged over 100 simulations and are angularly integrated along the angle θ. The final time is 900 peak periods (900 sec).

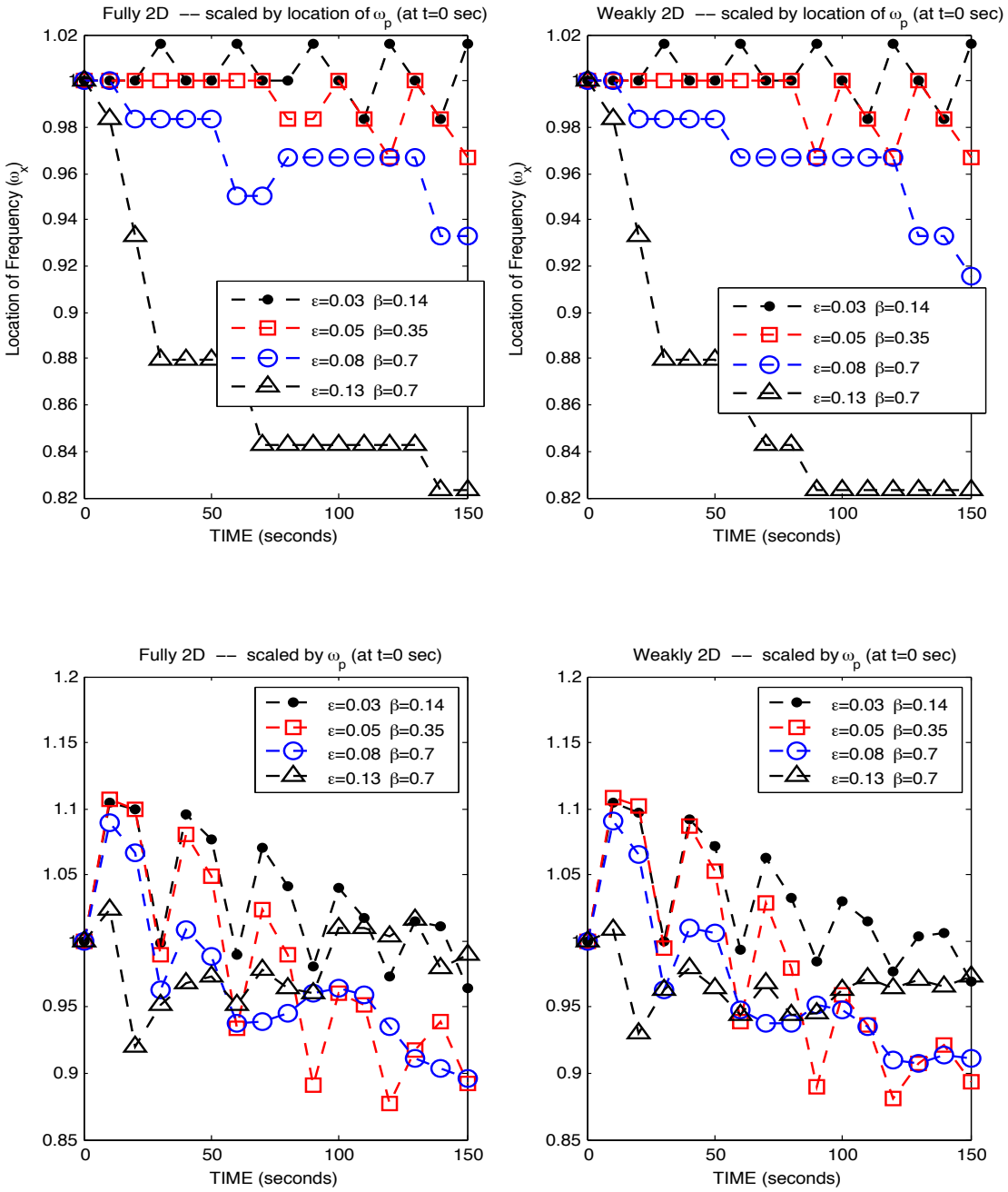

Figure 4.11 Top row gives the plots of the location of the spectral peak frequency (ω_p) as the function of time, for the Fully 2D (left) and Weakly 2D (right) models. While the bottom row shows the magnitude of the spectral peak frequency as a function of time, relative to the magnitude of the initial frequency peak (ω_p at $t = 0s$). Different degrees of directional distribution $\beta = 0.14, 0.35, 0.7$ and levels of wave steepness $\epsilon = 0.03, 0.05, 0.08, 0.13$ are also shown.

(β) and wave steepness (ϵ). Note that the spectra are symmetric over $\theta = 0$ line in the (k, θ) plane, hence we only plotted the first quadrant $\theta \in [0, \pi/2]$. In these plots, K_p represents the peak wave number, whose value is around 30 when unscaled by $2\pi/L_x$, or around 4 when scaled. What is apparent from the plots is that the spectra tend to develop a bi-modal structure around $k = K_p/3$, when the initial directional distribution broadens.

Finally, wanting to examine these two models in a more deterministic setting, in Figures 4.20-4.21, we plotted the cross sections of their surface elevations. The cross sections were chosen wherever the largest difference between the Fully and Weakly 2D models occurred. The first two cases of initial directional distribution ($\beta = 0.14, 0.35$) are almost indistinguishable, hence once again we elected to plot the latter two extreme cases of $\beta = 0.7$ for the steepness $\epsilon = 0.08$ (Figure 4.20) and $\epsilon = 0.13$ (Figure 4.21). For the first fifty peak periods (50 sec) the surface correlations are very promising and only after about one hundred peak periods we begin to notice appreciable differences in individual wave heights. It is rather difficult to asses whether the Fully or the Weakly 2D model tends to overestimate the occurrence of the large waves. Nevertheless, even after one hundred peak periods the wave speeds of large individual wave crests and troughs appear to be well resolved and surprisingly in sync.

Keeping with the spirit of extreme waves, we also correlated the fourth statistical moment (kurtosis) as an indicator for the occurrence of extreme waves – Rogue/Freak waves, whose commonly accepted definition is a wave of height at least twice of that of the significant wave height of the wave field. Recall that the kurtosis (m_4) was defined as

$$M_4(\zeta) = \sum_{j=1}^{N} \frac{(\zeta_j - \bar{\zeta})^4}{N} \qquad \Longrightarrow \qquad \text{Kurtosis :} \quad \mathrm{m}_4(\zeta) \equiv \frac{\mathrm{M}_4}{\sigma^4},$$

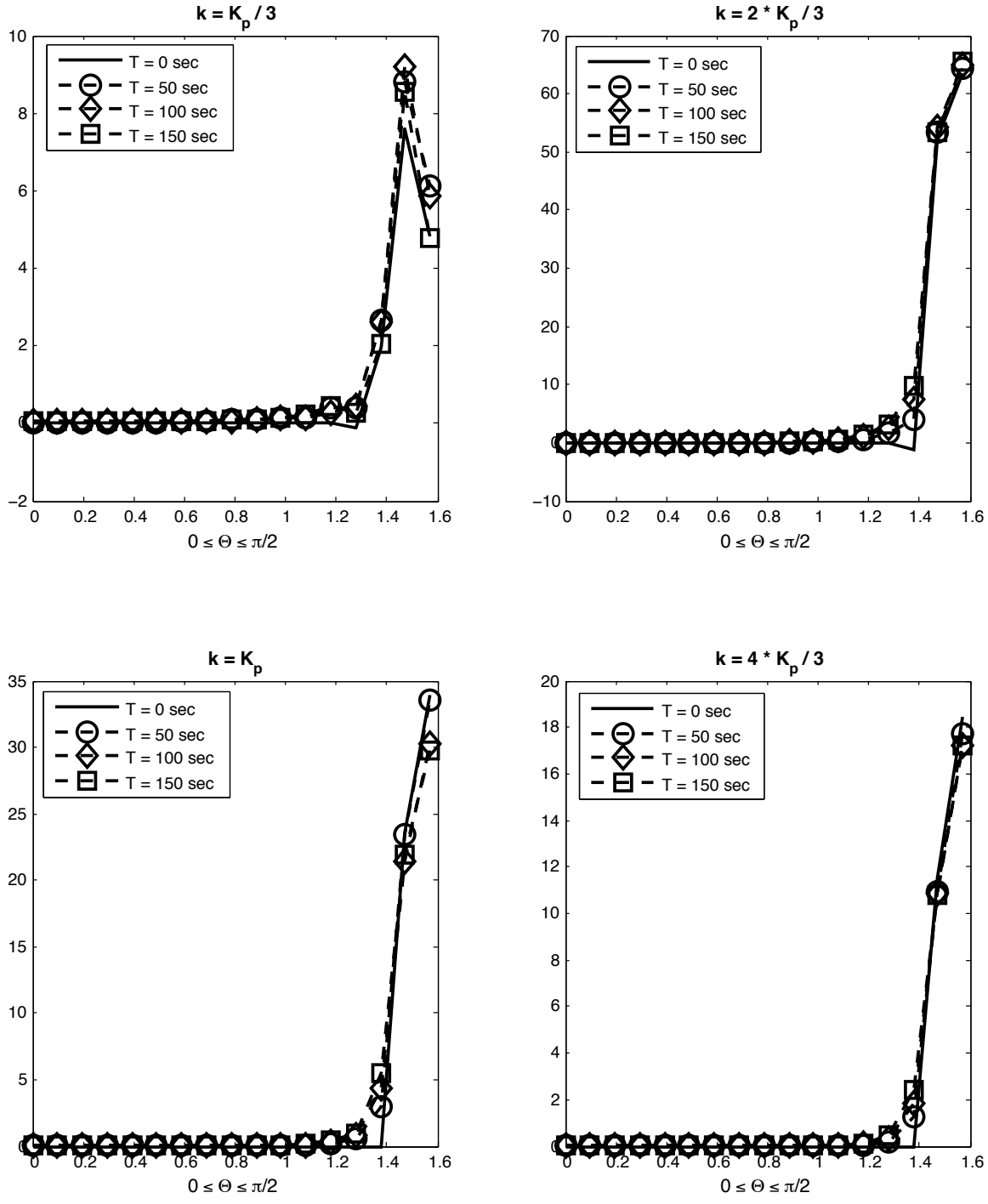

Figure 4.12 The angular distribution of the spectra of the Fully 2D model, for the initial case of $\beta = 0.14$ and $\epsilon = 0.03$. The plots were extracted along fixed values of k in the polar (k, θ) plane, where K_p represents the peak wavenumber.

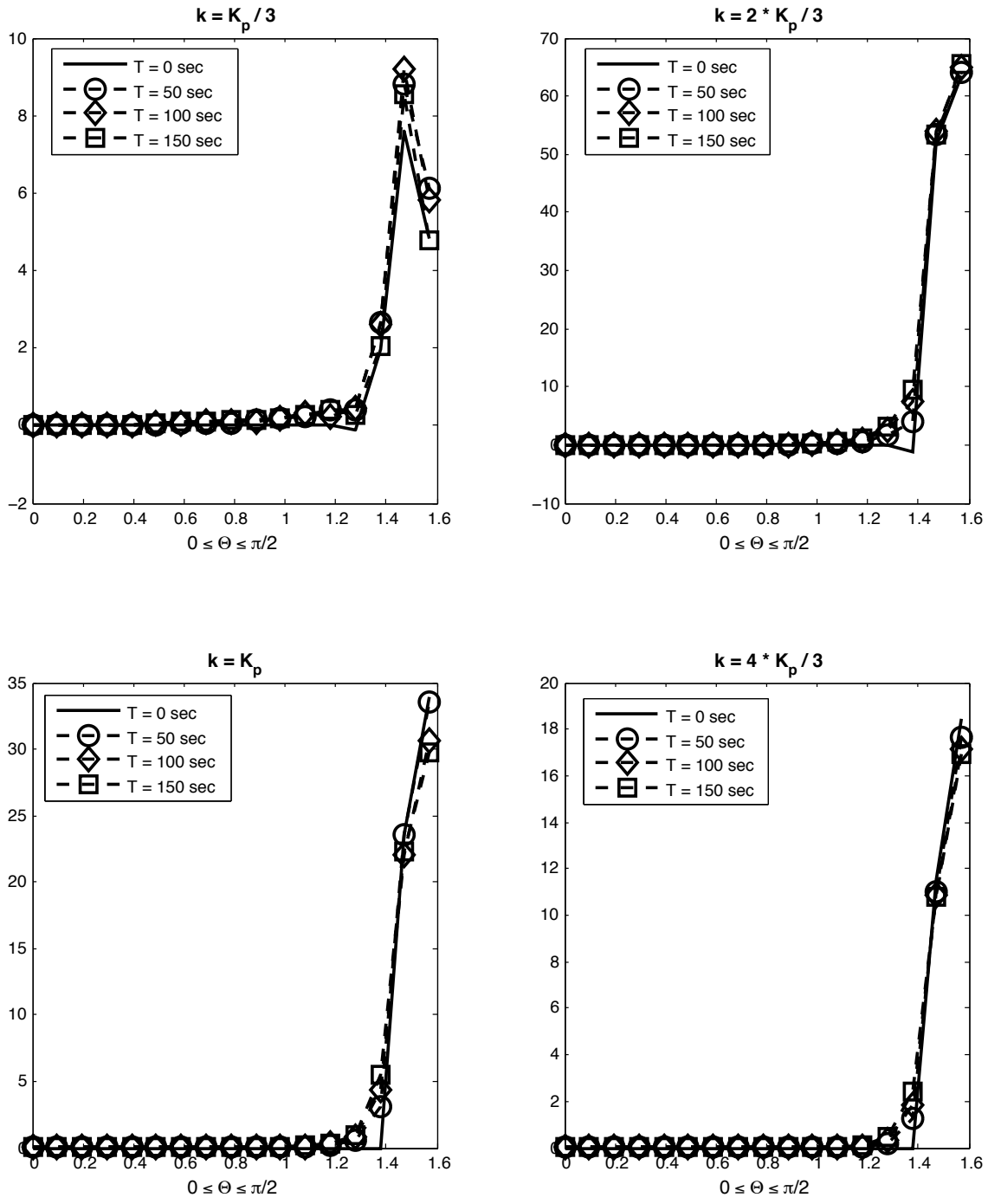

Figure 4.13 The angular distribution of the spectra of the Weakly 2D model, for the initial case of $\beta = 0.14$ and $\epsilon = 0.03$. The plots were extracted along fixed values of k in the polar (k, θ) plane, where K_p represents the peak wavenumber.

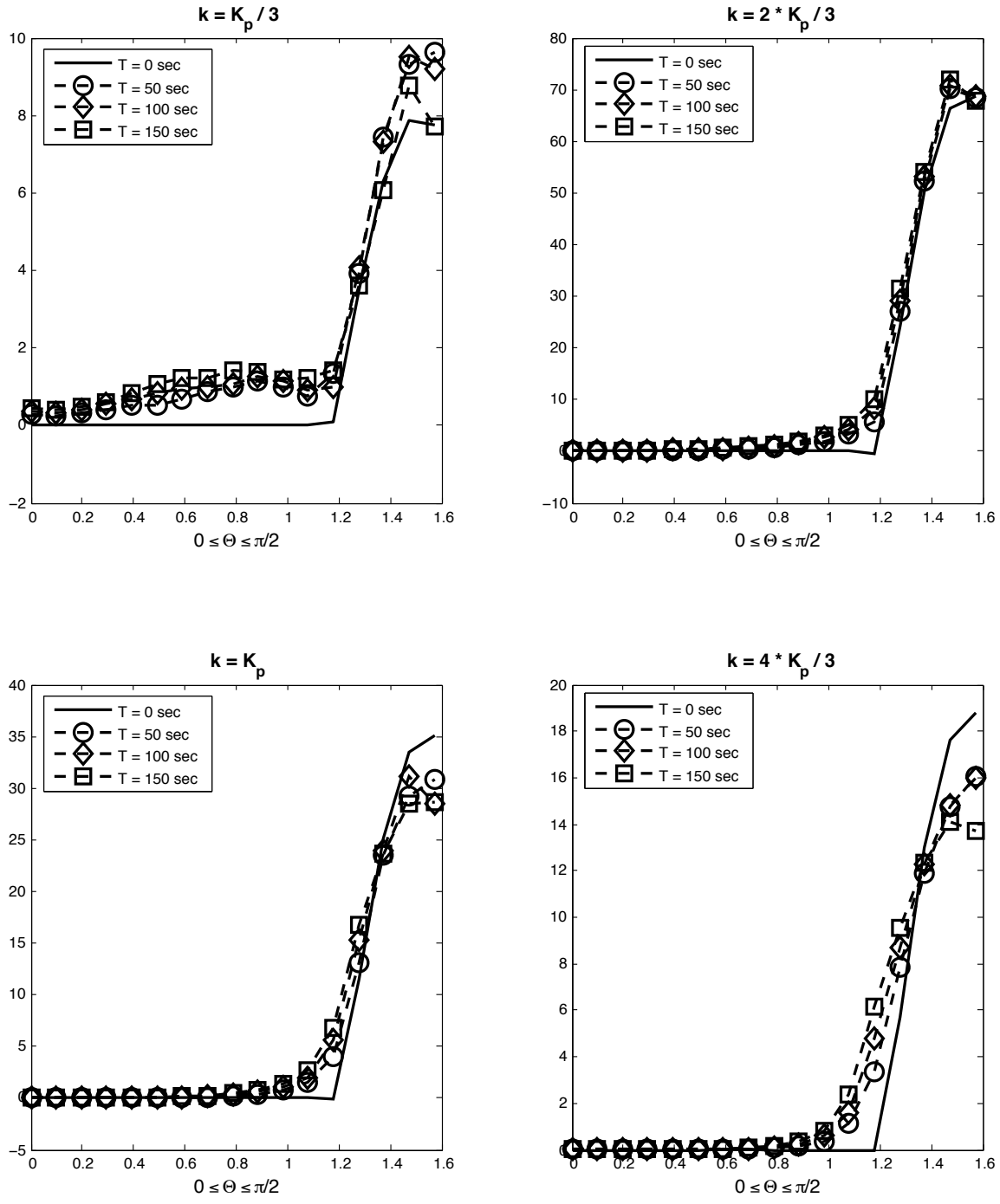

Figure 4.14 The angular distribution of the spectra of the Fully 2D model, for the initial case of $\beta = 0.35$ and $\epsilon = 0.05$. The plots were extracted along fixed values of k in the polar (k, θ) plane, where K_p represents the peak wavenumber.

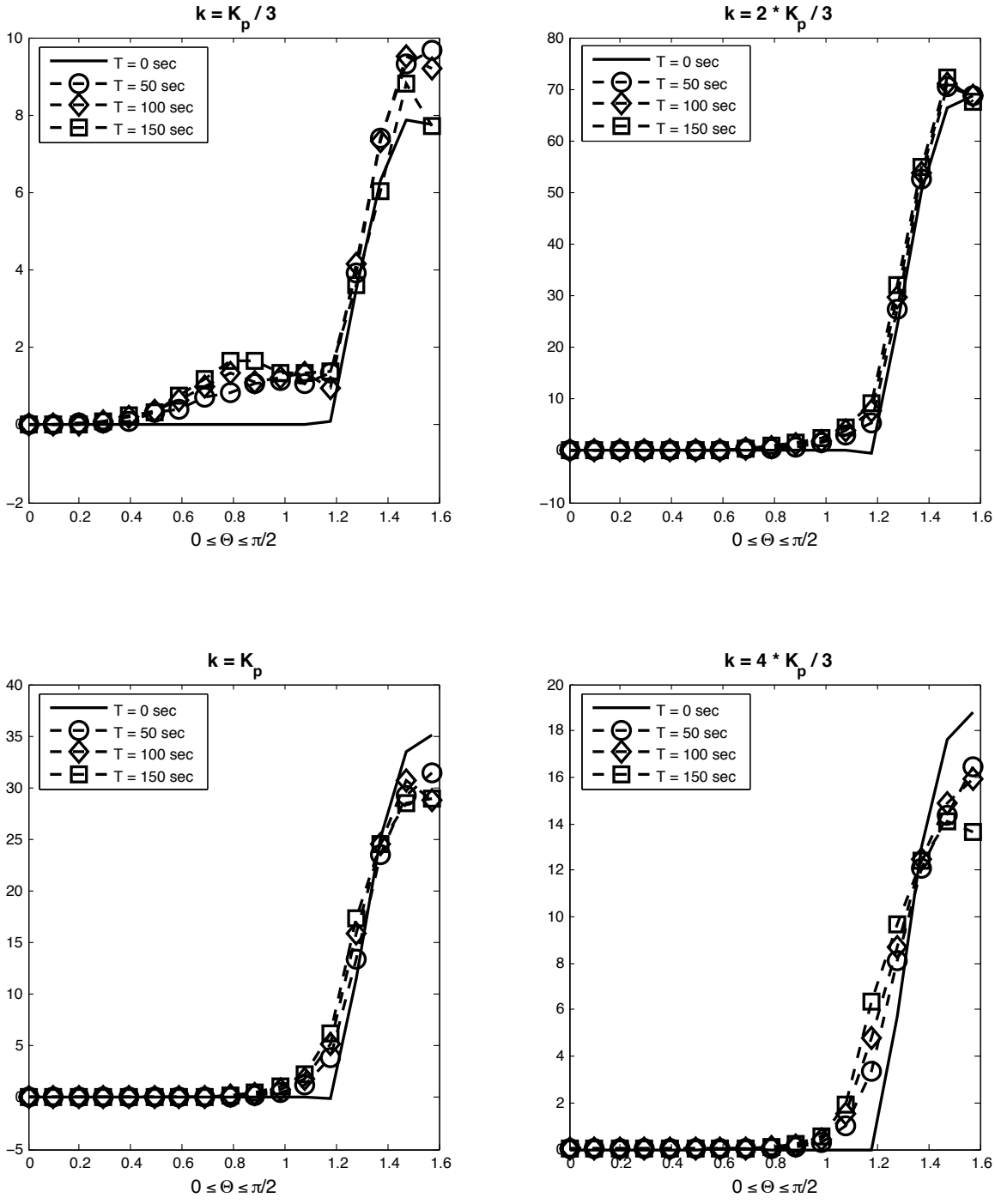

Figure 4.15 The angular distribution of the spectra of the Weakly 2D model, for the initial case of $\beta = 0.35$ and $\epsilon = 0.05$. The plots were extracted along fixed values of k in the polar (k, θ) plane, where K_p represents the peak wavenumber.

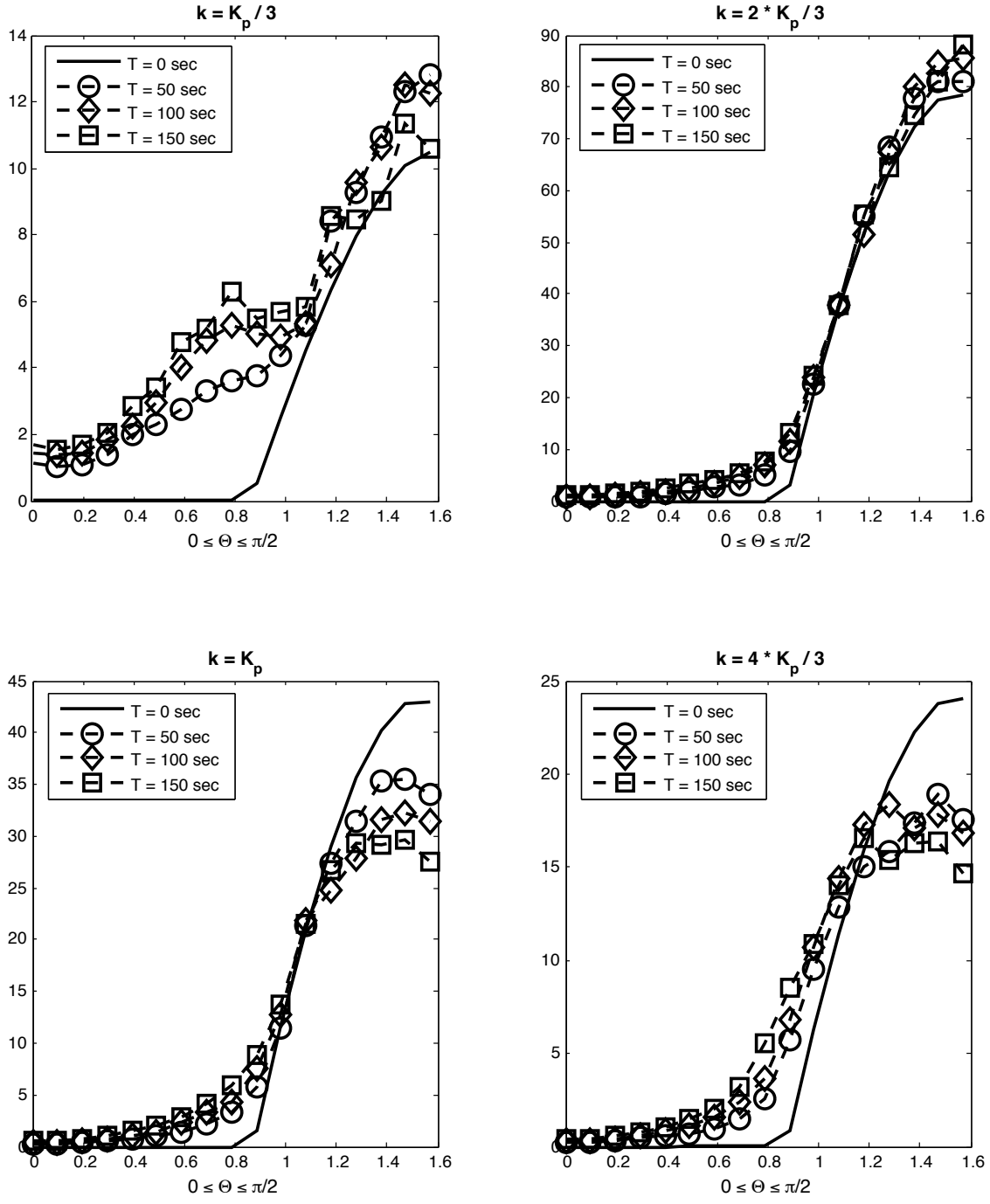

Figure 4.16 The angular distribution of the spectra of the Fully 2D model, for the initial case of $\beta = 0.7$ and $\epsilon = 0.08$. The plots were extracted along fixed values of k in the polar (k, θ) plane, where K_p represents the peak wavenumber.

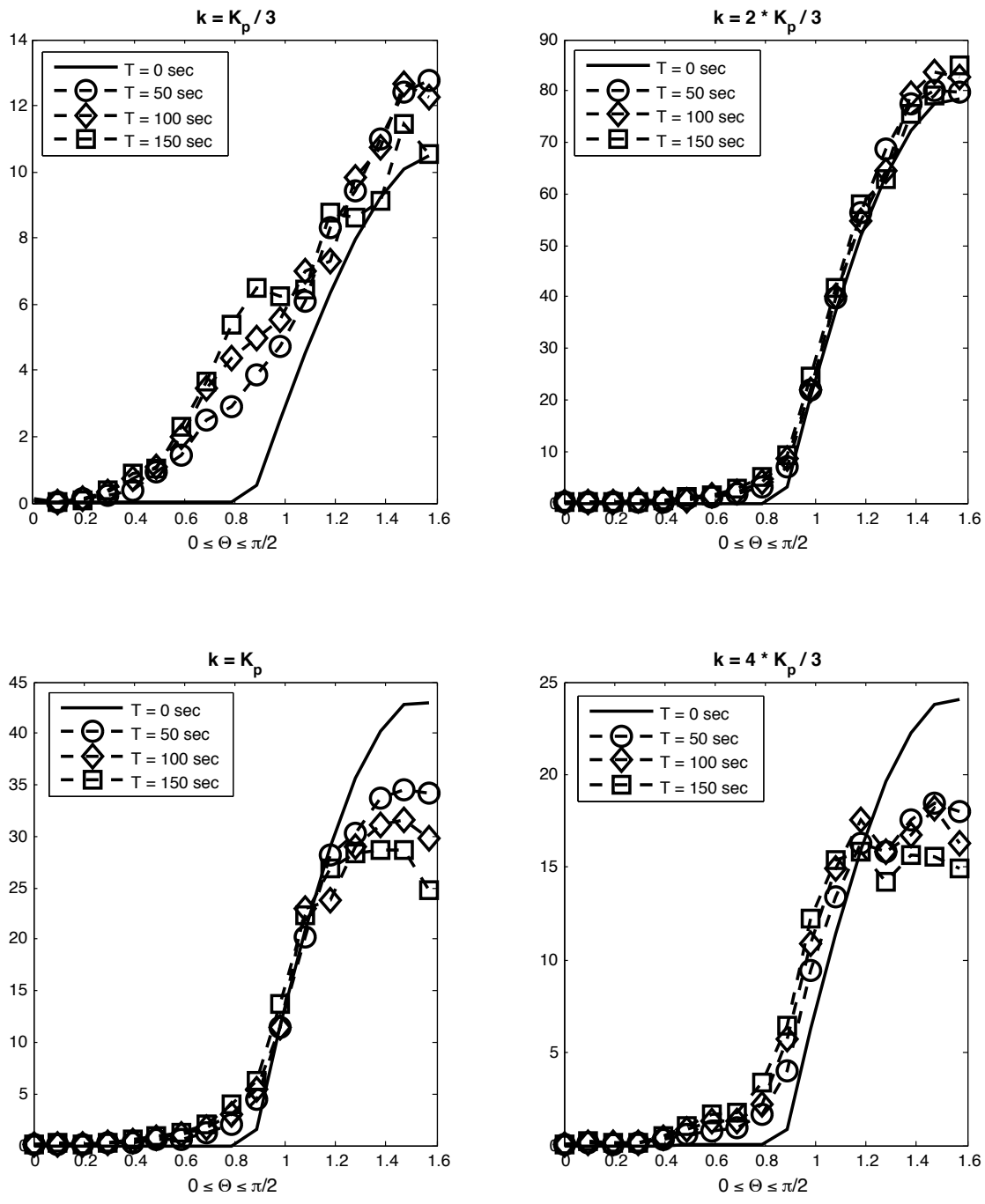

Figure 4.17 The angular distribution of the spectra of the Weakly 2D model, for the initial case of $\beta = 0.7$ and $\epsilon = 0.08$. The plots were extracted along fixed values of k in the polar (k, θ) plane, where K_p represents the peak wavenumber.

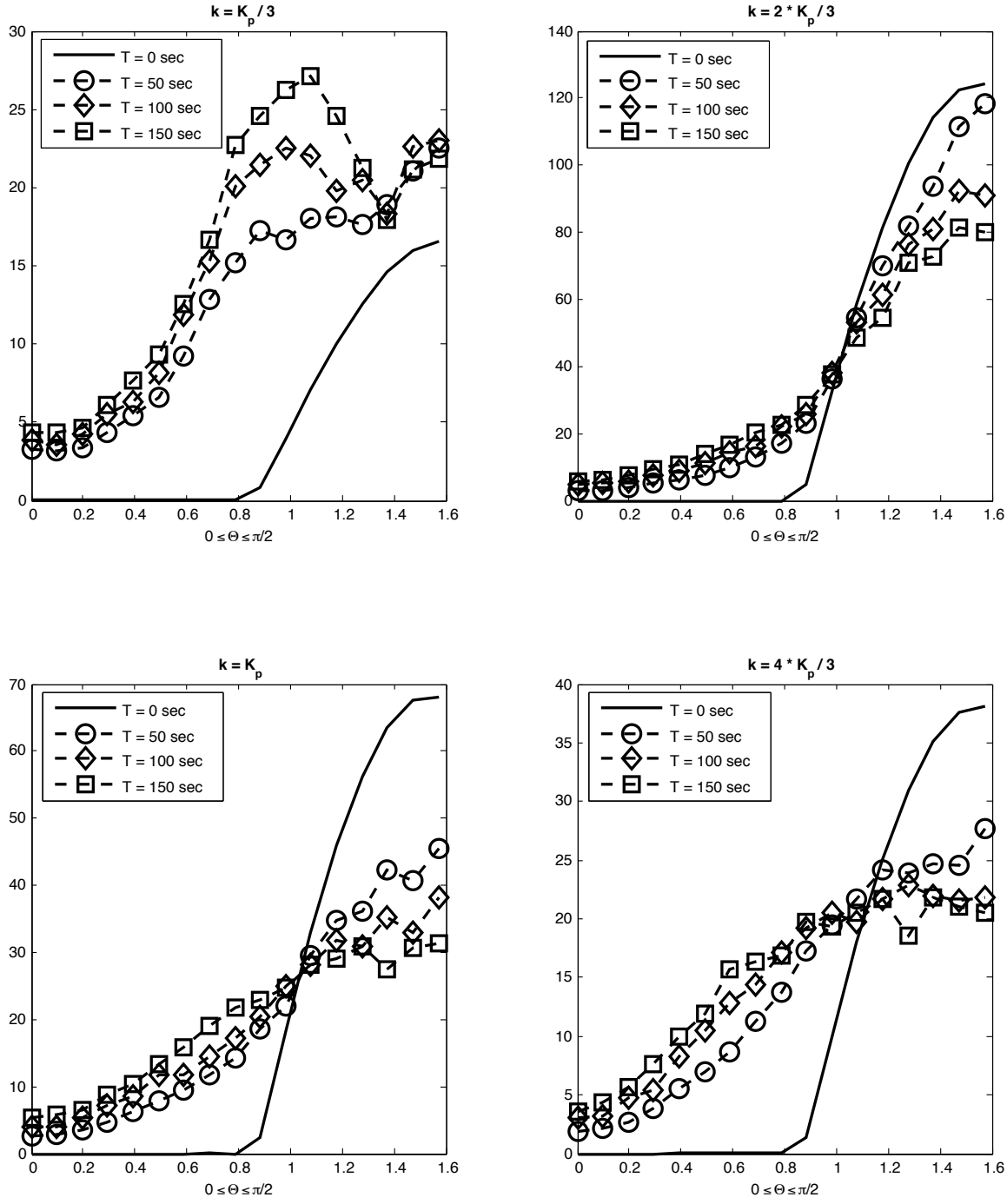

Figure 4.18 The angular distribution of the spectra of the Fully 2D model, for the initial case of $\beta = 0.7$ and $\epsilon = 0.13$. The plots were extracted along fixed values of k in the polar (k, θ) plane, where K_p represents the peak wavenumber.

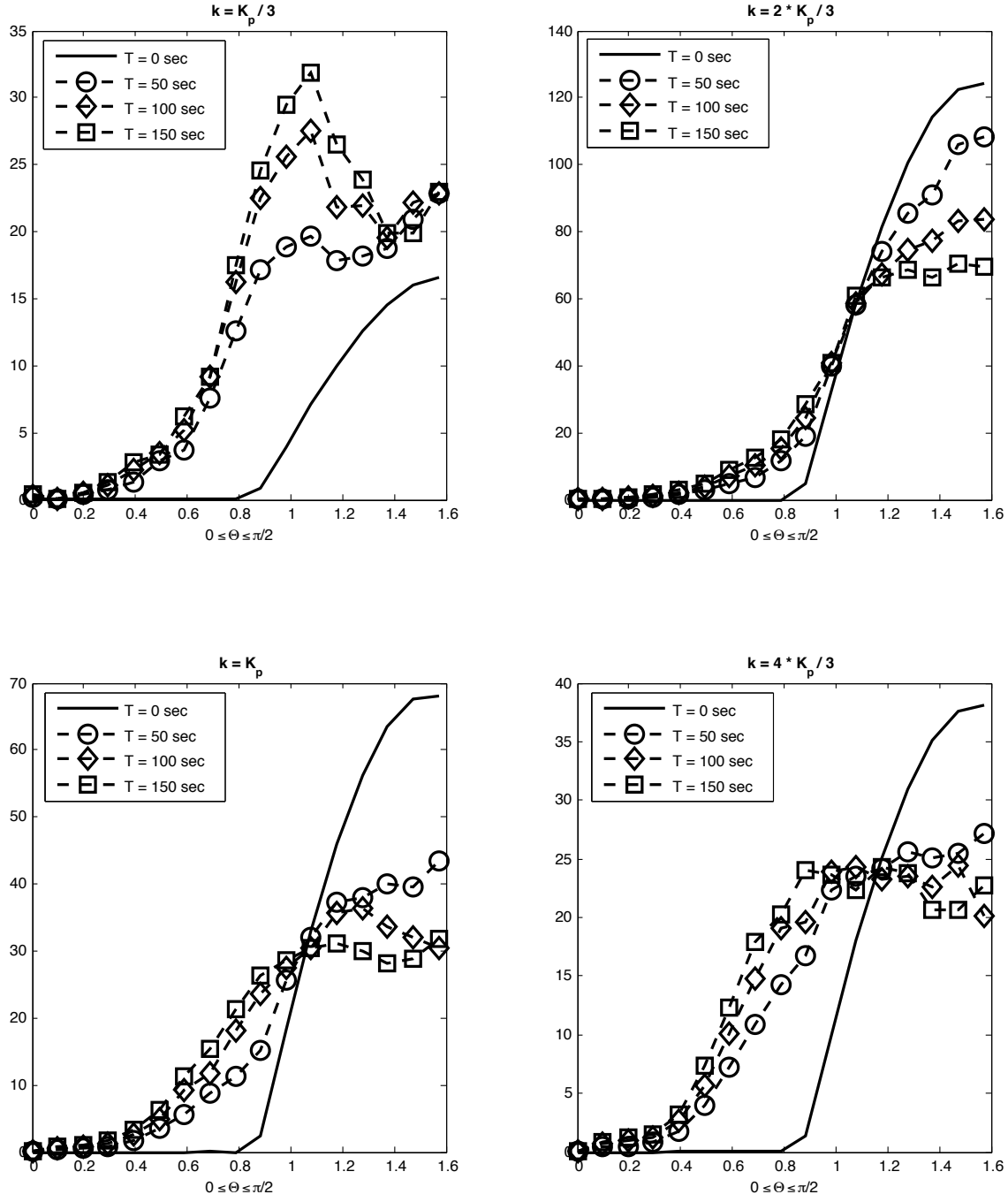

Figure 4.19 The angular distribution of the spectra of the Weakly 2D model, for the initial case of $\beta = 0.7$ and $\epsilon = 0.13$. The plots were extracted along fixed values of k in the polar (k, θ) plane, where K_p represents the peak wavenumber.

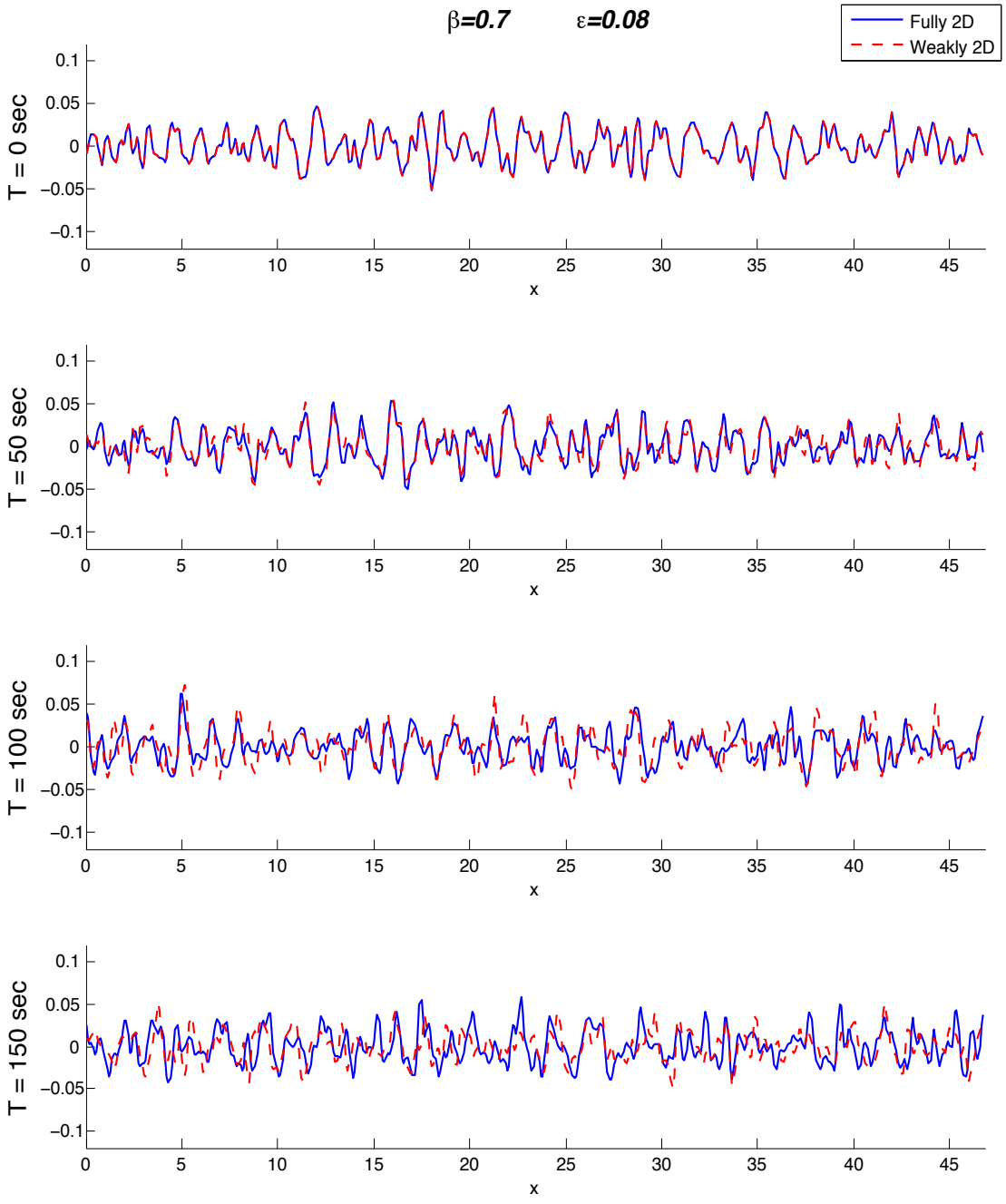

Figure 4.20 Deterministic surface-to-surface comparison for single simulation. The cross sections have been extracted along the transverse direction, wherever the largest difference between the surface elevations of the models occurred. The initial wave steepness is $\epsilon = 0.08$, for $\beta = 0.7$ directional spreading case of (3.9).

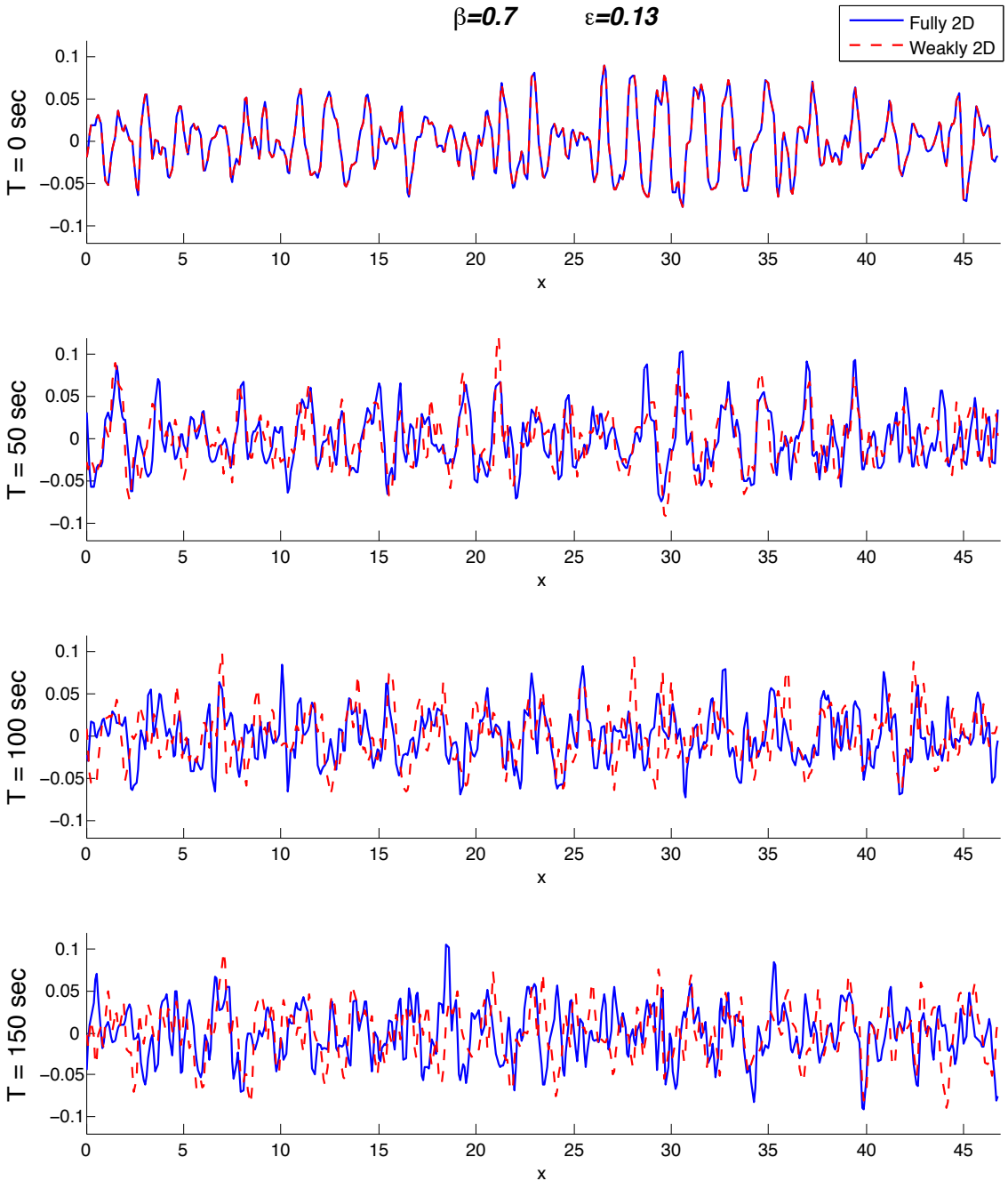

Figure 4.21 Deterministic surface-to-surface comparison for single simulation. The cross sections have been extracted along the transverse direction, wherever the largest difference between the surface elevations of the models occurred. The initial wave steepness is $\epsilon = 0.13$, with $\beta = 0.7$ directional spreading case of (3.9).

where σ^2 is the variance and σ is the standard deviation of the wave field given by

$$\sigma(\zeta) = \sqrt{\sum_{j=1}^{N} \frac{(\zeta_j - \bar{\zeta})^2}{N}}.$$

For the case of a single (or few) simulation(s), we clearly observed that the kurtosis increases beyond the value of three (where kurtosis equal to three corresponds to the standard Gaussian distribution) as the directional distribution (β) is made smaller/narrower. In fact, this has also been well documented in recent works of Onorato et al. (2006) and Toffoli et al. (2010). Moreover, when we averaged over 100 simulations for both 150 seconds (Figure 4.22) and 900 seconds (Figure 4.23) we also observed that kurtosis decreased as the directional distribution β in (3.9) broadened, but the fluctuations where much less prounouced, with the Weakly 2D model producing higher values of kurtosis than the Fully 2D model for the larger values of initial directional distribution (β). These results confirm those of Tanaka (2001), where he studied the evolution of random surface gravity waves by direct simulations of both, the HOSM (Higher Order Spectral Method) of West et al. (1987) and the Zakharov Equation (1968). Both of these equations do not suffer from the narrow-bandwidth assumption, but the Zakharov equation – being an integro-differential equation, takes considerably more time to compute. It should, however, be of no surprise that the kurtosis of the ensemble averaged simulations is closer to the value of the standard Gaussian distribution (kurtosis=3) than for a single (or couple) of simulations, since it is expected (via the Central Limit Theorem) that as the number of averaged simulations increases, we tend to approach the Gaussian spectrum.

4.2 Comparison Between Fully 2D Model and Modified Nonlinear Schrödinger Equation (MNLS)

In this section we present the results of concurrent numerical simulations of the MNLS and Fully 2D models, and comment on the observed features of the deterministic

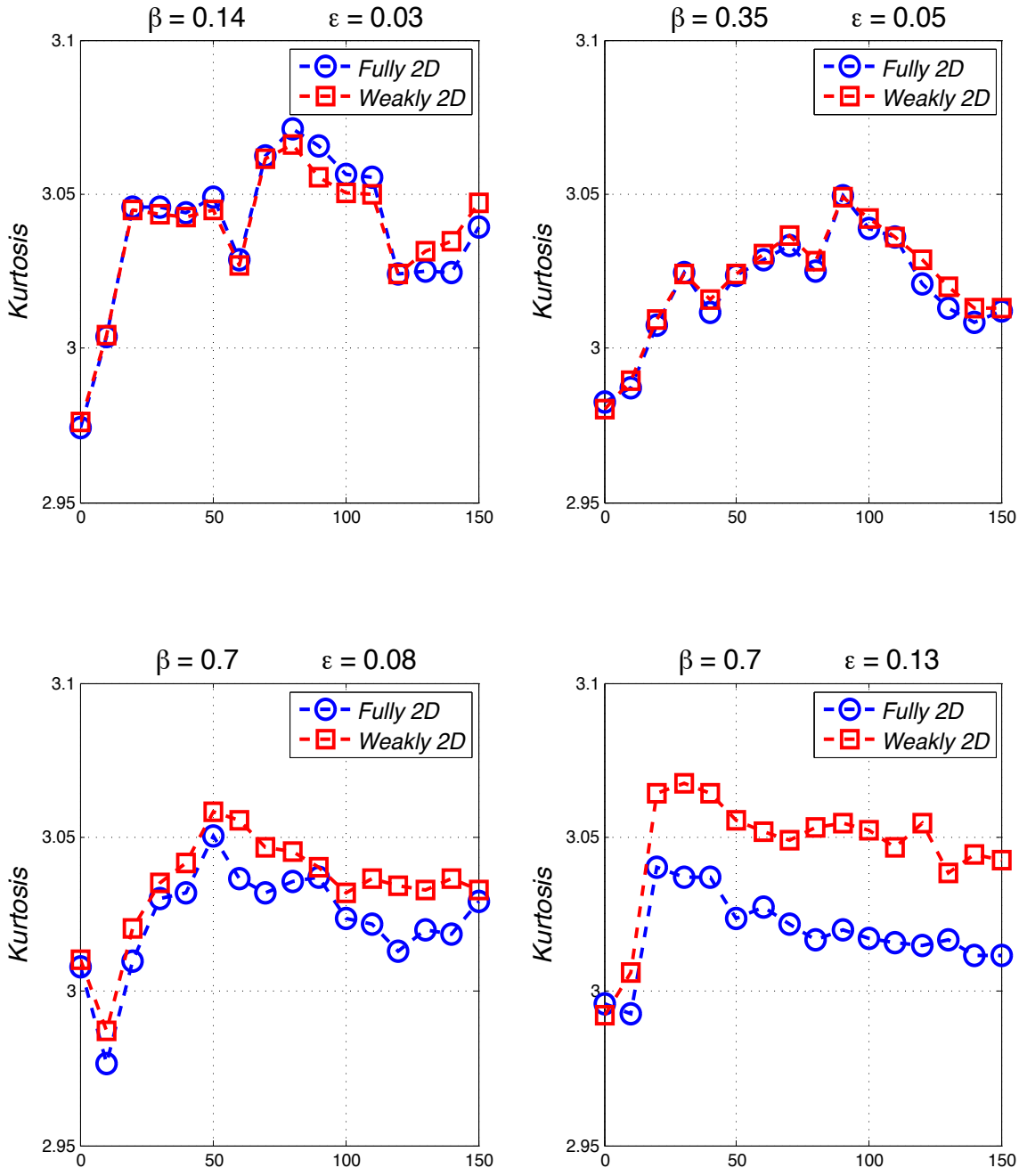

Figure 4.22 Averaged kurtosis from 100 simulations up to 150 seconds for three different cases of directional distribution ($\beta = 0.14, 0.35, 0.7$) and four different initial wave steepnesses ($\epsilon = 0.03, 0.05, 0.08, 0.13$) for Fully and Weakly 2D models.

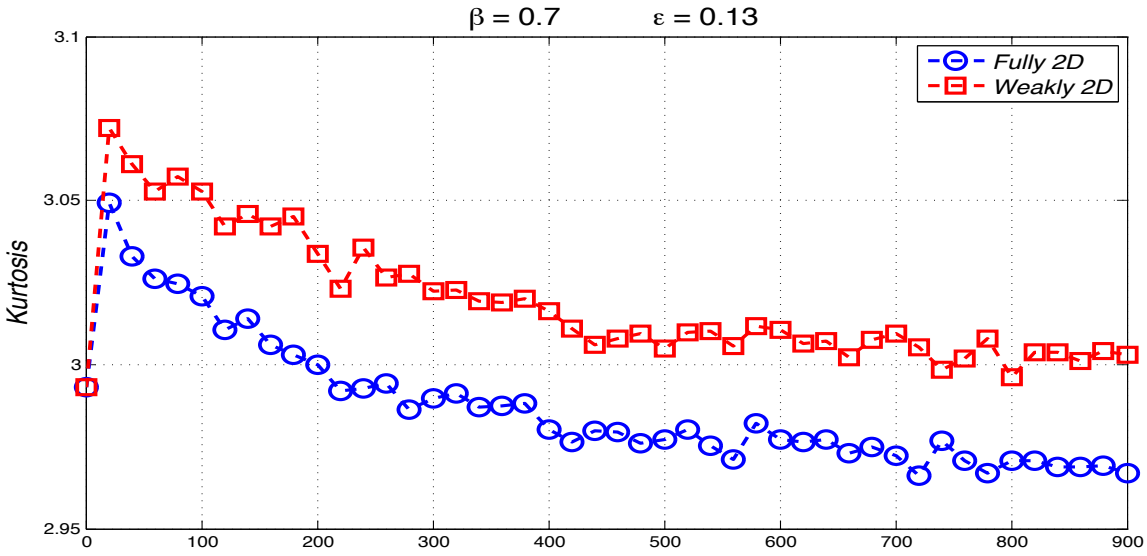

Figure 4.23 Averaged kurtosis from 100 simulations up to 900 seconds for $\beta = 0.7$ cases of directional distribution and initial wave steepness $\epsilon = 0.13$ for Fully and Weakly 2D models.

(single run) and Monte-Carlo (averaged over 100 runs) simulations. In Figures 4.24, 4.25, and 4.30, the averaged spectra (over 100 initially random simulations) for the intermediate case of directional distribution ($\beta = 0.35$) for the two-dimensional Fully (2.12)-(2.13), Weakly (2.14)-(2.15), and MNLS (2.22)-(2.23) model systems are presented, respectively.

Moreover, in the simulation of the MNLS equation (with cubic nonlinearity), rather than using the conventional rectangular half-zero-pad filter for de-aliasing, we used a circular type filter centered at ($N_x/4$, 0) (for MNLS only) with radius of $N_x/4$. This rather peculiar type of filter, also utilized in the work of Dysthe et al. (2003), allows us to suppress the quasi-recurring energy leakage (instability) originally studied and discussed by Martin and Yuen (1980). In Figure 4.26, we show that very same energy leakage when a standard rectangular half-zero-padding filter is used. Nevertheless, the spectral evolution of the two-dimensional MNLS equation with the circular filter is in good qualitative agreement with the results obtained by Socquet-Juglard et al. (2005). Also, what is relatively difficult to determine from the

two-dimensional spectral density plots, but is more apparent in Figures 4.27, 4.28, and 4.29, is that in the evolution of the spectrum one can notice evident shifting of the spectral peak, as well as a definite rise of the tail of the spectrum.

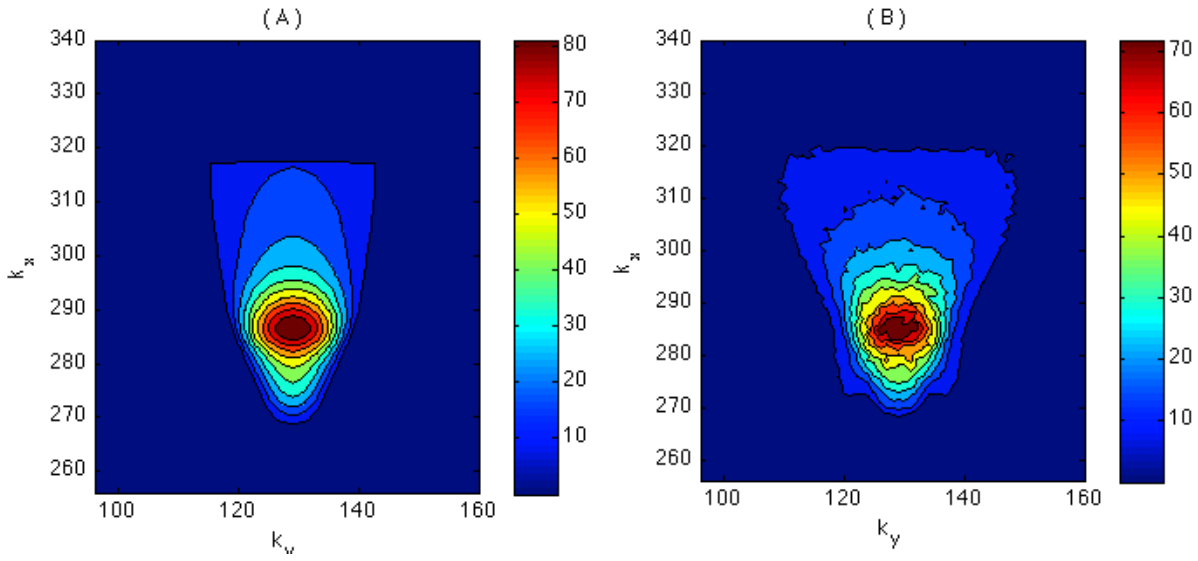

Figure 4.24 Averaged spectrum (over 100 random realization) for Fully 2D model system, for Case (2) with $\beta = 0.35$, $\gamma = 5$, $\Delta t = 10^{-3}$. Graph (A) shows the initial spectrum ($t = 0$ *sec*), while graph (B) shows the spectrum at final time ($t = 150\, T_p = 150$ *sec*), along with 10 level curves.

Finally, we would like to present direct comparisons of the Fully 2D and MNLS 2D models. In Figures 4.31 and 4.32, the intermediate (Case 2) and the widest (Case 3) spreading cases are contrasted. What should also be immediately apparent is that the surface extracted from MNLS has a smaller wave front velocity for individual wave crests (especially those with higher steepness), but more importantly MNLS seems to underestimate the occurrence of extreme waves when contrasted with the solution of the Fully 2D in the widest case — $\beta = 0.7$ and $\gamma = 3.3$ - see Figure 4.32.

As a final note, we would like to comment on the surface initialization and extraction between the Fully 2D and MNLS models. Given the initial JONSWAP spectrum $F(k, \theta)$, the surface elevation (ζ) was initialized via the Fourier transform of the autocorrelation function, as discussed in chapter 3. Then, the envelope variable

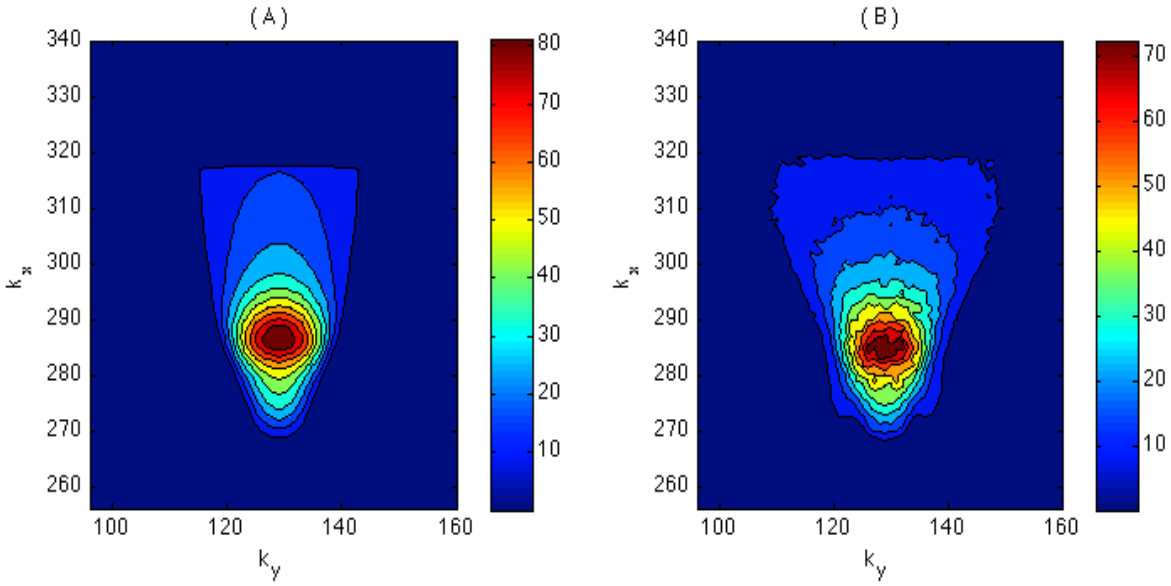

Figure 4.25 Averaged spectrum (over 100 random realization) for Weakly 2D model system, for Case (2) with $\beta = 0.35$, $\gamma = 5$, $\Delta t = 10^{-3}$. Graph (A) shows the initial spectrum ($t = 0$ *sec*), while graph (B) shows the spectrum at final time ($t = 150\,T_p = 150$ *sec*), along with 10 level curves.

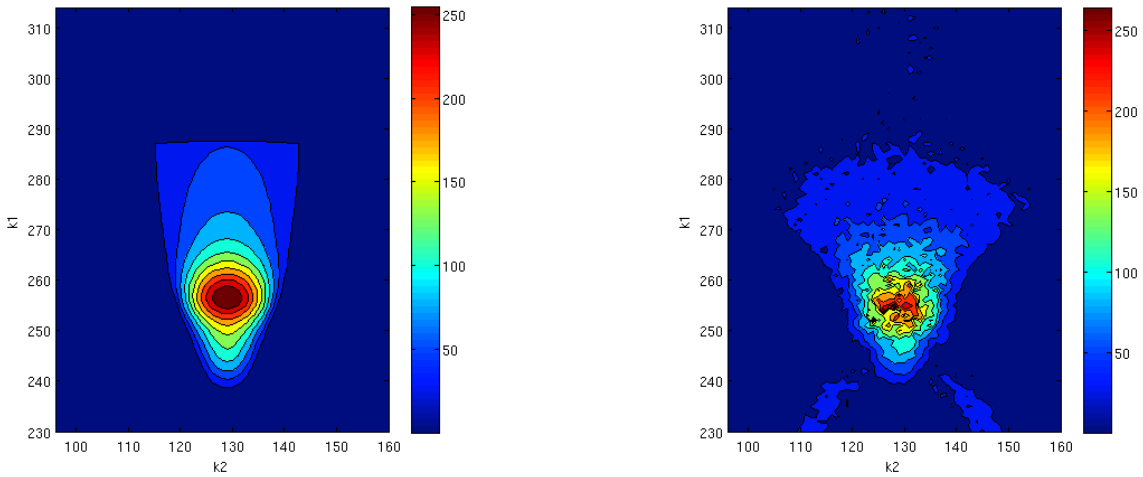

Figure 4.26 Averaged spectrum of the Modified Nonlinear Schrödinger Equation (MNLS) for10 runs with rectangular zero-pad de-aliasing filter, exhibiting the energy cascade along the instability branches (see the Appendix for derivation of instability regions). The density plot on the left shows the initial spectrum (t=0 sec), while the graph on the right is the spectrum at t=100 seconds. For this simulation the directional spreading β was chosen to be 0.35 and the peak enhancement γ was equal to 5.0.

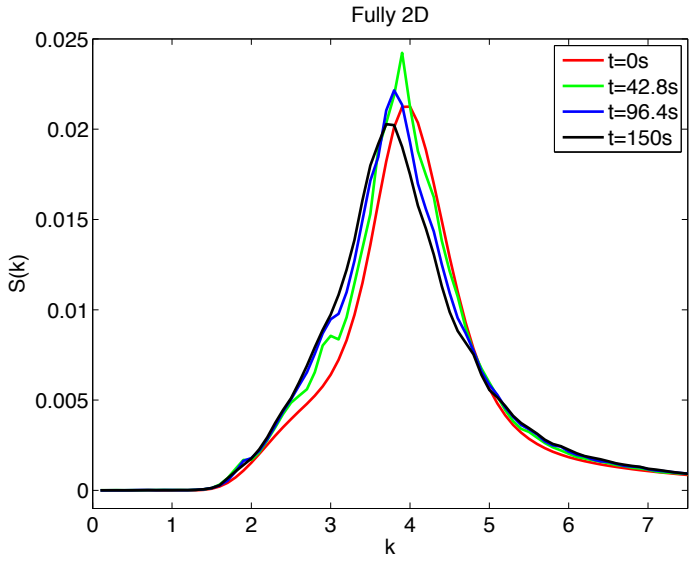

Figure 4.27 Angularly integrated spectrum of the Fully 2D model, for the intermediate case of directional spreading — $\beta = 0.35$ and $\gamma = 5$.

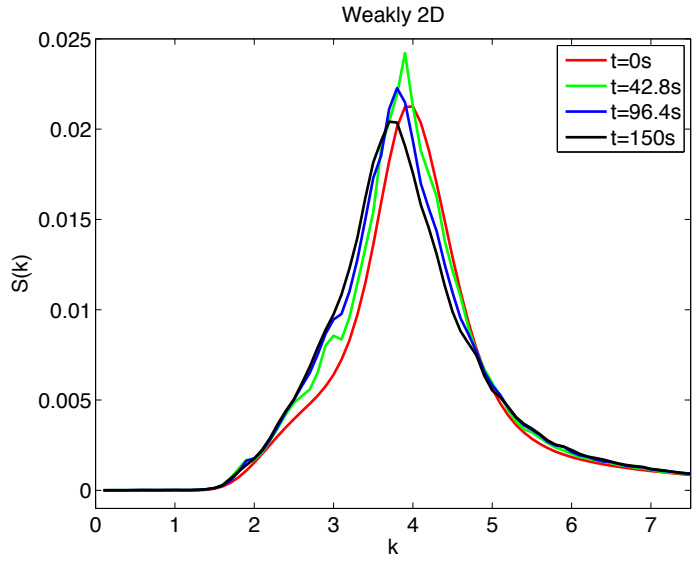

Figure 4.28 Angularly integrated spectrum of the Weakly 2D model, for the intermediate case of directional spreading — $\beta = 0.35$ and $\gamma = 5$.

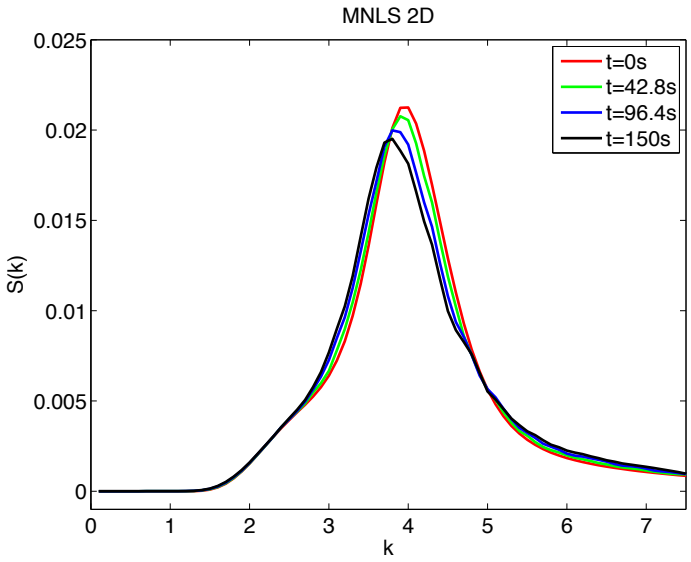

Figure 4.29 Angularly integrated spectrum of the MNLS 2D model, for the intermediate case of directional spreading — $\beta = 0.35$ and $\gamma = 5$.

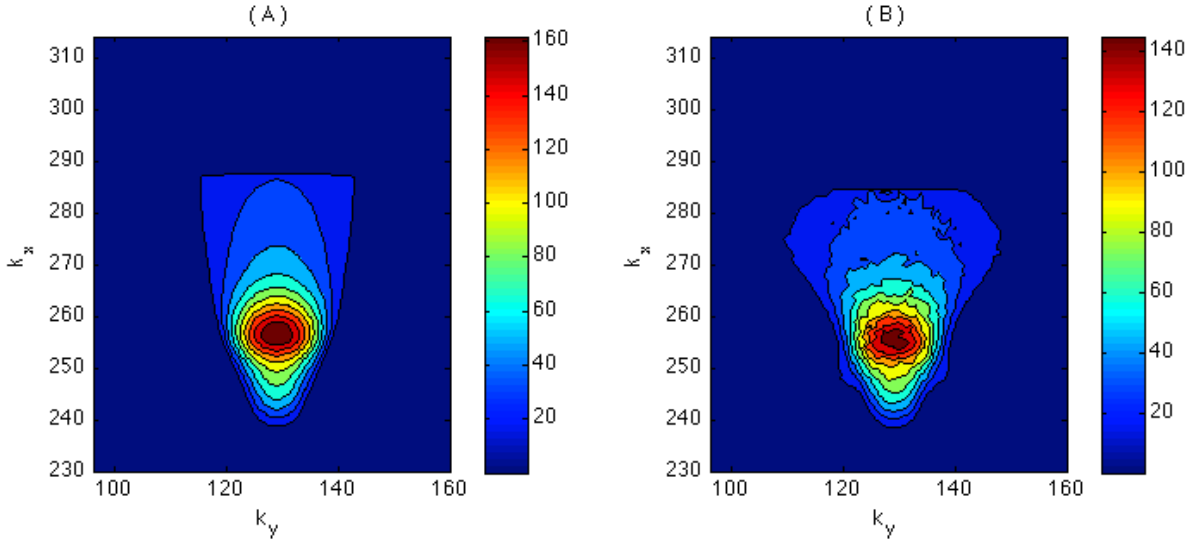

Figure 4.30 Averaged spectrum (over 100 random realization) for MNLS 2D model system, for Case (2) with $\beta = 0.35$, $\gamma = 5$, $\Delta t = 10^{-3}$. Graph (A) shows the initial spectrum ($t = 0$ *sec*), while graph (B) shows the spectrum at final time ($t = 150\,T_p = 150$ *sec*), along with 10 level curves. **NOTE:** here we used a circular zero-pad filter.

(A) in the MNLS equation was initialized with a simple phase shift and all of the initial energy was put solely into a first harmonic (A), since

$$\zeta(x,y,t) = \frac{1}{2}A\mathrm{e}^{i(k_x x + k_y y - \omega t)} + \text{higher order terms} + c.c.\,,$$

where $c.c.$ represents the complex conjugate. In fact, when we took the time to spread the energy over the first three harmonics (A, A_2, A_3), we did not notice any appreciable differences in the final results, hence we elected to simplify our initialization by writing

$$\zeta(x,y,t=0) = \frac{1}{2}A\mathrm{e}^{i(k_x x + k_y y)} + c.c = \frac{1}{2}A\mathrm{e}^{i\theta} + c.c \quad \Longrightarrow \quad A = \zeta \mathrm{e}^{-i\theta}.$$

Once the simulations were initialized, the final results for the evolution of the envelope (A) were transformed into a surface elevation ζ. In other words, we used the reconstruction formulae given by (2.26), to set up to the surface elevation, correct up to third order in wave steepness (ϵ^3).

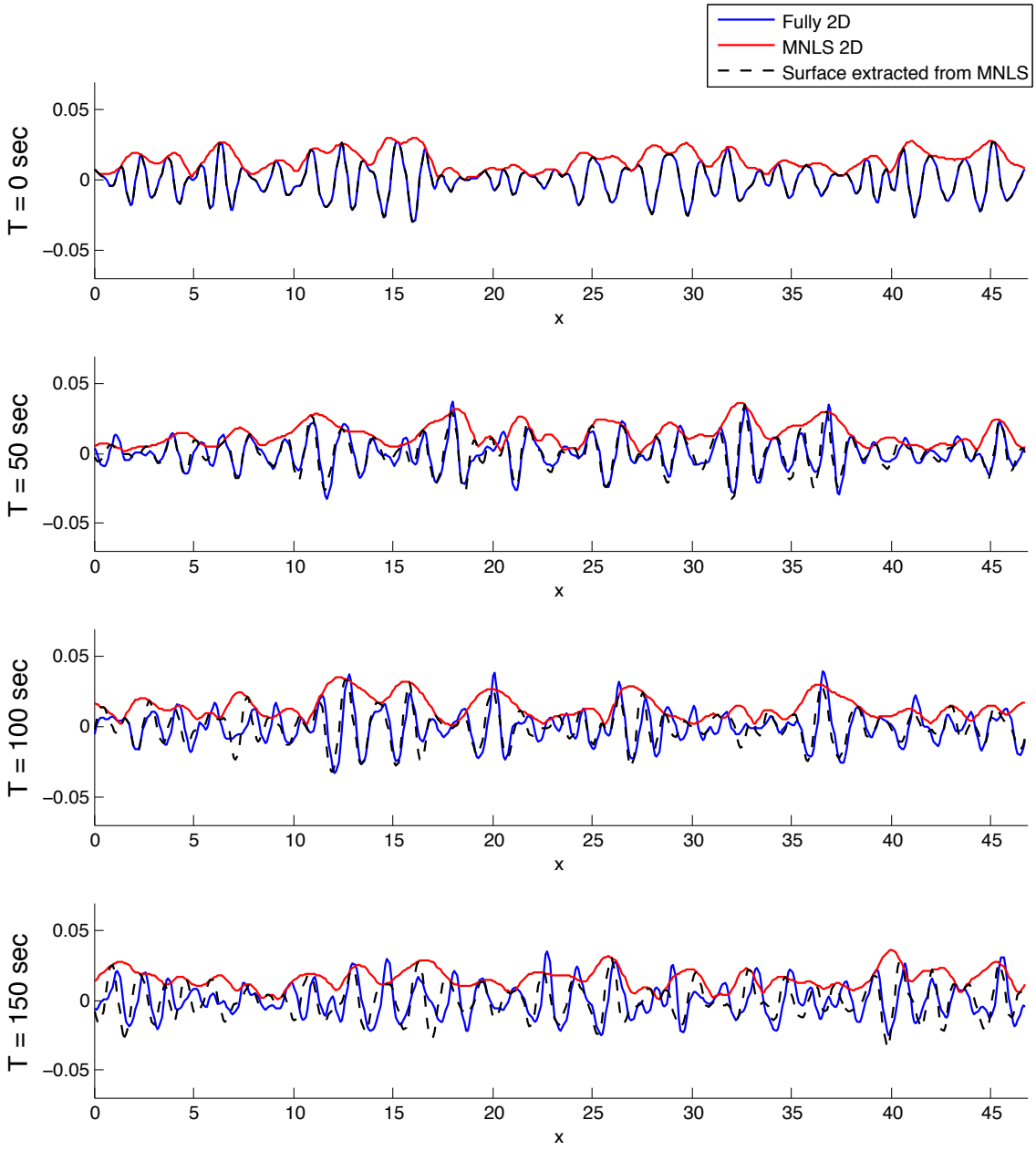

Figure 4.31 Single deterministic run comparison of Fully 2D and MNLS 2D models for the intermediate case of transverse dependence: Case 2 - $\beta = 0.35$, $\gamma = 5$, with $\Delta t = 10^{-3}$. Snapshot taken along a particular value of y-coordinate which produced the largest difference between two surface models.

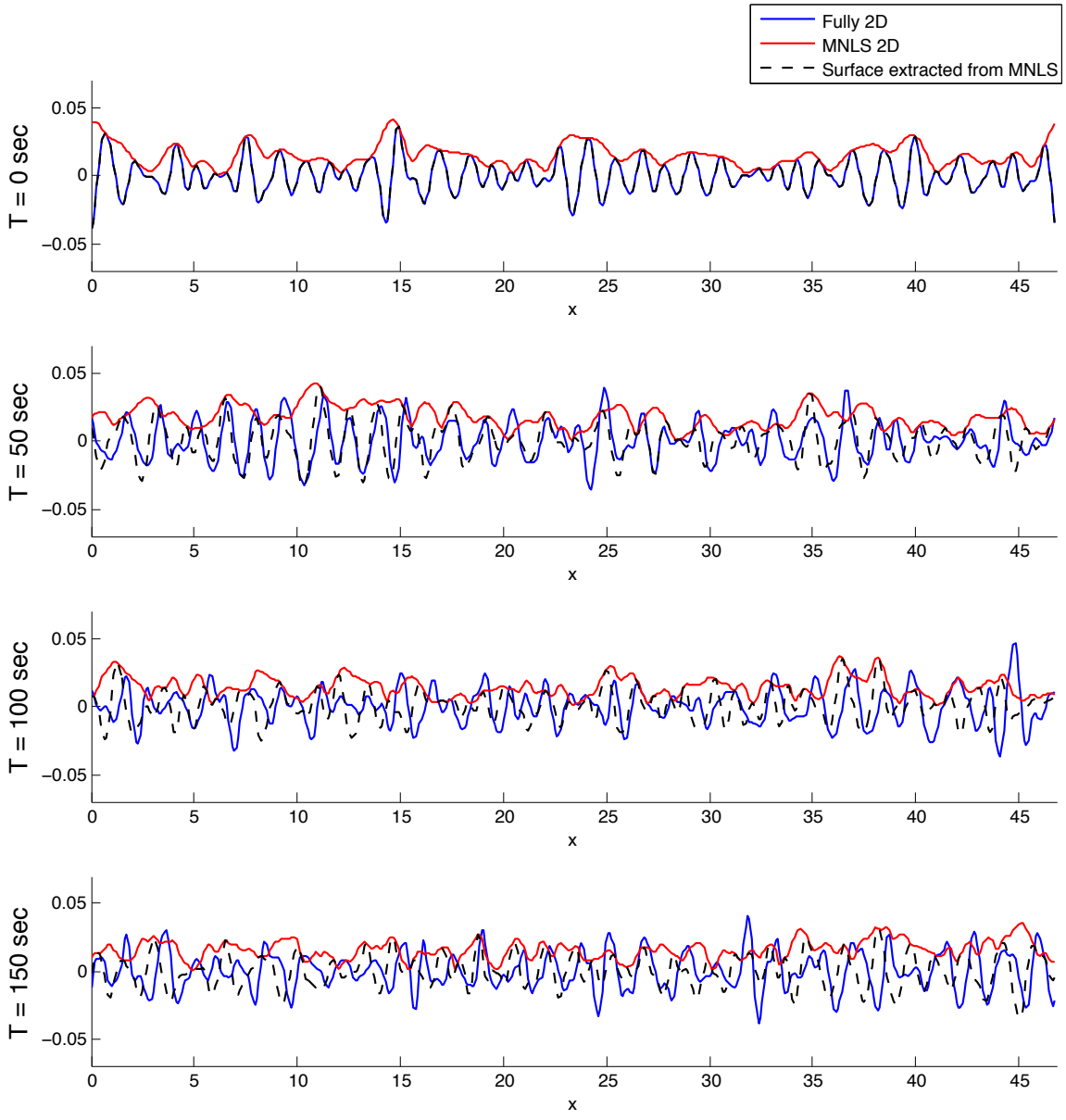

Figure 4.32 Single deterministic run comparison of Fully 2D and MNLS 2D models for the largest case of transverse dependence: Case 3 - $\beta = 0.7$, $\gamma = 3.3$, with $\Delta t = 10^{-3}$. Snapshot taken along a particular value of y-coordinate which produced the largest difference between two surface models.

CHAPTER 5

REDUCED ORDER UNCOUPLED SYSTEMS

5.1 Bi-directional Uncoupled Models

This section and its immediate subsections deal with both uncoupled bi-directional and uni-directional wave propagation. For the latter we will, without loss of generality, propose a one dimensional version of the equations. Recall once again the Fully 2D system of evolution equations (2.12) and (2.13), that is reproduced here for convenience.

$$\frac{\partial \zeta}{\partial t} = -\mathcal{L}[\Phi] - \nabla(\zeta \nabla \Phi) - \mathcal{L}[\zeta \mathcal{L}[\Phi]] - \nabla^2 \left(\frac{\zeta^2}{2} \mathcal{L}[\Phi] \right) - \mathcal{L} \left[\frac{\zeta^2}{2} \nabla^2 \Phi + \zeta \mathcal{L}[\zeta \mathcal{L}[\Phi]] \right] + O(\epsilon^4),$$

$$\frac{\partial \Phi}{\partial t} = -g\zeta - \frac{1}{2} |\nabla \Phi|^2 + \frac{1}{2} \left(\mathcal{L}[\Phi] \right)^2 + \mathcal{L}[\Phi] \left(\zeta \nabla^2 \Phi + \mathcal{L}[\zeta \mathcal{L}[\Phi]] \right) + O(\epsilon^4).$$

At the leading-order we have

$$\begin{cases} \frac{\partial \zeta}{\partial t} = -\mathcal{L}[\Phi] \\ \\ \frac{\partial \Phi}{\partial t} = -g\zeta \,, \end{cases} \tag{5.1}$$

with cross time derivative we obtain a bi-directionl uncoupled system

$$\begin{cases} \frac{\partial^2 \zeta}{\partial t^2} = g\mathcal{L}[\zeta] \\ \\ \frac{\partial^2 \Phi}{\partial t^2} = g\mathcal{L}[\Phi] \,, \end{cases} \tag{5.2}$$

and the unidirectional aspect of the above system will be discussed in material that follows when we deal with a second order system. Subsequently, truncating at the

second order yields ($\epsilon = k_p \bar{a}$)

$$\begin{cases} \frac{\partial \zeta}{\partial t} + \mathcal{L}[\Phi] + \nabla(\zeta \nabla \Phi) + \mathcal{L}[\zeta \mathcal{L}[\Phi]] + O(\epsilon^3) = 0 \\ \frac{\partial \Phi}{\partial t} + g\zeta + \frac{1}{2}|\nabla \Phi|^2 - \frac{1}{2}\left(\mathcal{L}[\Phi]\right)^2 + O(\epsilon^3) = 0\,, \end{cases} \tag{5.3}$$

and then at third order we have

$$\begin{cases} \frac{\partial \zeta}{\partial t} = -\mathcal{L}[\Phi] - \nabla(\zeta \nabla \Phi) - \mathcal{L}[\zeta \mathcal{L}[\Phi]] - \nabla^2\left(\frac{\zeta^2}{2}\mathcal{L}[\Phi]\right) - \mathcal{L}\left[\frac{\zeta^2}{2}\nabla^2\Phi + \zeta \mathcal{L}[\zeta \mathcal{L}[\Phi]]\right] + O(\epsilon^4) \\ \frac{\partial \Phi}{\partial t} = -g\zeta - \frac{1}{2}|\nabla \Phi|^2 + \frac{1}{2}\left(\mathcal{L}[\Phi]\right)^2 + \mathcal{L}[\Phi]\left(\zeta \nabla^2 \Phi + \mathcal{L}[\zeta \mathcal{L}[\Phi]]\right) + O(\epsilon^4)\,. \end{cases} \tag{5.4}$$

First, in order to decouple the system accurate to second order we take the time derivative of the second equation in (5.3) and substitute it into the first equation, while using the second equation in (5.1) in the nonlinear (second order correction) terms wherever ζ appears, hence effectively making sure that the error is $O(\epsilon^3)$. Then we arrive at a decoupled system of equations for the velocity potential Φ (defined at the free-surface) and the corresponding surface elevation ζ, both being correct up to the second order

$$\frac{\partial^2 \Phi}{\partial t^2} - g\mathcal{L}[\Phi] + 2\nabla\Phi \cdot \nabla \Phi_t + \frac{\partial \Phi}{\partial t}\nabla^2 \Phi - \mathcal{L}[\Phi]\mathcal{L}[\Phi_t] + \mathcal{L}\left[\frac{\partial \Phi}{\partial t}\mathcal{L}[\Phi]\right] = 0\,, \tag{5.5}$$

$$g\zeta = -\frac{\partial \Phi}{\partial t} + \frac{1}{2}(\mathcal{L}[\Phi])^2 - \frac{1}{2}|\nabla \Phi|^2\,. \tag{5.6}$$

Extending this procedure to third order and making similar substitution for ζ with (5.1) and (5.6) where appropriate to keep the error $O(\epsilon^4)$ yields

$$\begin{aligned}\Phi_{tt} \quad & - g\Omega + \nabla\Phi\cdot\nabla\Phi_t - \tfrac{1}{2}(\Omega^2)_t + \nabla\left(\left[\Phi_t - \tfrac{1}{2}\Omega^2 + \tfrac{1}{2}|\nabla\Phi|^2\right]\nabla\Phi\right)\\ & + \mathcal{L}\left[\left(\Phi_t - \tfrac{1}{2}\Omega^2 + \tfrac{1}{2}|\nabla\Phi|^2\right)\Omega\right] - \tfrac{1}{g}\nabla^2\left(\tfrac{1}{2}(\Phi_t)^2\Omega\right) - \tfrac{1}{g}\mathcal{L}\left[\tfrac{1}{2}(\Phi_t)^2\nabla^2\Phi + \Phi_t\mathcal{L}[\Phi_t\Omega]\right]\\ & + \tfrac{1}{g}\Omega_t(\Phi_t\nabla^2\Phi + \mathcal{L}[\Phi_t\Omega]) + \tfrac{1}{g}\Omega(\Phi_{tt}\nabla^2\Phi + \Phi_t\nabla^2\Phi_t + \mathcal{L}[\Phi_{tt}\Omega + \Phi_t\Omega_t]) + O(\epsilon^4) = 0,\end{aligned} \tag{5.7}$$

$$g\zeta = -\Phi_t + \tfrac{1}{2}\Omega^2 - \tfrac{1}{2}|\nabla\Phi|^2 - \tfrac{1}{g}\Omega(\Phi_t\nabla^2\Phi + \mathcal{L}[\Phi_t\Omega]) + O(\epsilon^4). \tag{5.8}$$

Where $\Omega \equiv -\mathcal{L}[\Phi]$ and just to clean up a bit, our third order uncoupled system (after using (5.2) to substitute for Φ_{tt} at the end of (5.7)) becomes

$$\begin{cases}\Phi_{tt} - g\Omega + \mathcal{S}\{\Phi,\Phi_t\} + \mathcal{C}\{\Phi,\Phi_t\} + O(\epsilon^4) = 0\\ g\zeta = -\Phi_t - \tfrac{1}{2}|\nabla\Phi|^2 + \tfrac{1}{2}\Omega^2 - \tfrac{1}{g}\Omega(\Phi_t\Delta\Phi + \mathcal{L}[\Phi_t\Omega]) + O(\epsilon^4)\,,\end{cases} \tag{5.9}$$

where $\mathcal{S}$ and $\mathcal{C}$ are defined by

$$\mathcal{S}\{\Phi,\Phi_t\} = \quad 2\nabla\Phi\cdot\nabla\Phi_t + \Phi_t\Delta\Phi + \mathcal{L}[\Phi_t\Omega] - \Omega\,\Omega_t\,,$$

$$\begin{aligned}\mathcal{C}\{\Phi,\Phi_t\} = \quad & -\Omega\,\nabla\Omega\cdot\nabla\Phi + |\nabla\Omega|\nabla(|\nabla\Phi|)\cdot\nabla\Phi + \tfrac{1}{2}\Omega^2\Delta\Phi + \tfrac{1}{2}|\nabla\Phi|^2\Omega\\ & - \tfrac{1}{2}\mathcal{L}[\Omega^3] + \tfrac{1}{2}\mathcal{L}[|\nabla\Phi|^2\Omega] - \tfrac{1}{g}|\nabla\Phi_t|^2\Omega - \tfrac{1}{g}\Phi_t\Delta\Phi_t\Omega - \tfrac{2}{g}\Phi_t\nabla\Phi_t\cdot\nabla\Omega\\ & - \tfrac{1}{2g}(\Phi_t)^2\Delta\Omega - \tfrac{1}{2g}\mathcal{L}[(\Phi_t)^2\Delta\Phi] - \tfrac{1}{g}\mathcal{L}[\Phi_t\mathcal{L}[\Phi_t\Omega]] - \tfrac{1}{g}\Omega_t\Phi_t\Delta\Phi\\ & - \tfrac{1}{g}\Omega_t\mathcal{L}[\Phi_t\Omega] + \tfrac{1}{g}\Omega\Phi_t\Delta\Phi_t + \Omega\mathcal{L}[\Omega^2] + \tfrac{1}{g}\Omega\mathcal{L}[\Phi_t\Omega_t].\end{aligned}$$

At this point it would be beneficial to justify the validity and correctness of our model. For that purpose we step back to our model accurate to second order and compare our result with, as far as we know, the only decoupled model of Akers and Milewski (2008). It should be pointed out that their model deals with water of infinite depth and the velocity potential ϕ_o defined at the mean surface, as well as

the surface tension. Therefore we substitute

$$\begin{aligned}\Phi &= \phi_o - \zeta\mathcal{L}[\phi_o] - \frac{\zeta^2}{2}\Delta\phi_o + O(\epsilon^4) \\ &= \phi_o + \left(\frac{1}{g}\phi_{o_t} - \frac{1}{g}\left(\frac{1}{2}\mathcal{L}[\phi_o]^2 - \frac{1}{2}|\nabla\phi_o|^2\right)\right)\mathcal{L}[\phi_o] - \frac{1}{2g^2}(\phi_{o_t})^2\Delta\phi_o + O(\epsilon^4)\end{aligned}$$

into (5.5) and truncate at second order (dropping terms of $O(\epsilon^3)$) and then we obtain (dropping the subscript o)

$$\phi_{tt} - g\mathcal{L}[\phi] + \frac{1}{2}(\mathcal{L}[\phi]^2)_t + \frac{1}{2}(|\nabla\phi|^2)_t + \nabla(\nabla\phi\,\phi_t) + \frac{1}{g}\left(\mathcal{L}[\phi_t]\phi_t\right)_t + O(\epsilon^3) = 0. \quad (5.10)$$

Setting $\mathcal{L} \Rightarrow -\mathcal{L}$ and non-dimensionalizing to scale g out of the problem, plus accounting for finite water depth and no surface tension effects in our model, allows us to recover the exact form of the equation of Akers and Milewski (2008).

5.2 Uni-Directional Models (Second Order)

When the truncation was done at the second order it mirrored the results of Akers and Milewski (2008), as expected. However, the question on what will happen at the third order is still an open one, and as far as we are concerned, apparently has not been investigated by anyone yet. Nevertheless, the apparent advantages of the reduction to a single equation (unidirectional model) should be clear, both analytically, as well as numerically. The first approach we are going to present parallels that of Akers and Milewski (2008), where the leading order (linear) terms are split into two modal wave components. For reference we reproduce here a one-dimensional (two-dimensional surface elevation) form of equation (5.5)

$$\Phi_{tt} - g\mathcal{L}[\Phi] + 2\Phi_x\Phi_{xt} - \frac{1}{2}(\mathcal{L}[\Phi]^2)_t + \Phi_t\Phi_{xx} + \mathcal{L}[\Phi_t\mathcal{L}[\Phi]] = 0 \quad (5.11)$$

and subsequently we split up the linear terms by defining

$$2u \equiv \Phi_t + i\mathcal{M}\Phi \qquad\qquad 2v \equiv \Phi_t - i\mathcal{M}\Phi, \tag{5.12}$$

where the operator $\mathcal{M}$ has the following form in the Fourier space

$$\hat{\mathcal{M}} = \mathrm{sgn}(\kappa)\sqrt{g|\kappa|\tanh(|\kappa|h)},$$

with $\Phi_t = u + v$ and $\Phi = (i\mathcal{M})^{-1}(u - v)$. Therefore, the newly formed system takes on the following form

$$\begin{cases} u_t - i\mathcal{M}u + \frac{1}{2}\mathcal{Q}(u+v, (i\mathcal{M})^{-1}(u-v)) = 0, \\ v_t + i\mathcal{M}v + \frac{1}{2}\mathcal{Q}(u+v, (i\mathcal{M})^{-1}(u-v)) = 0, \end{cases} \tag{5.13}$$

where $\mathcal{Q}$ is for now the next (second) order correction defined in terms of u and v as

$$\begin{aligned} \mathcal{Q}\left((i\mathcal{M})^{-1}(u-v),\ u+v\right) = \ & 2(u_x + v_x)(i\mathcal{M})^{-1}(u_x - v_x) \\ & +(u+v)(i\mathcal{M})^{-1}(u_{xx} - v_{xx}) \\ & +\mathcal{L}\left[(u+v)\mathcal{L}[(i\mathcal{M})^{-1}(u-v)]\right] \\ & -\mathcal{L}\left[(i\mathcal{M})^{-1}(u-v)\right]\ \mathcal{L}[u+v]. \end{aligned} \tag{5.14}$$

However, if we assume that Φ has a small projection on waves in one direction, or in other words if v starts off small (say $O(\epsilon^2)$) then it will remain small (loosely speaking) for a"long time" (Akers and Milewski 2008). Hence, we can effectively uncouple the system (5.13) by dropping v in the next order correction $\mathcal{Q}$ of the first equation, thus arriving at

$$\begin{aligned} u_t - i\mathcal{M}u \quad & +\tfrac{1}{2}\left(2u_x(i\mathcal{M})^{-1}u_x + u(i\mathcal{M})^{-1}u_{xx} + \mathcal{L}\left[u\mathcal{L}[(i\mathcal{M})^{-1}u]\right]\right) \\ & -\tfrac{1}{2}\left(\mathcal{L}\left[(i\mathcal{M})^{-1}u\right]\mathcal{L}[u]\right) + O(\epsilon^3) = 0. \end{aligned} \tag{5.15}$$

To illustrate our reasoning more clearly, we can express (5.13) in the following form

$$\begin{cases} u_t - L[u] + N_2[u^2, uv, v^2] = 0, \\ v_t + L[v] + N_2[u^2, uv, v^2] = 0, \end{cases} \tag{5.16}$$

where the operators L and N_2 are the linear and nonlinear operator parts of (5.13), respectively. In addition, if we suppose that initially $v = 0$ and $u = O(\epsilon)$ then v will be $O(u^2) \Rightarrow O(\epsilon^2)$ for the duration of the time for the validity of the second order asymptotic approximation. Therefore, any coupling between u and v can be neglected at that order, hence essentially leaving first equation of (5.16), or rather (5.13), solely in terms of u.

In the first equation of (5.13) at the next order (correct up to $O(\epsilon^3)$), however, we cannot simply drop all the terms that have v in it, since at that order the coupling between u and v is no longer negligible. We can instead use the second equation in (5.13) for v along the same lines, that is if we assume initially $v = O(\epsilon^2)$ then it will remain at the same order for a quite a long time, which of course would have to be rigorously determined. Our system could be symbolically represented in the following form

$$\begin{cases} u_t - L[u] + N_2[u^2, uv, v^2] + N_3[u^3, u^2v, uv^2, v^3] = 0, \\ v_t + L[v] + N_2[u^2, uv, v^2] + N_3[u^3, u^2v, uv^2, v^3] = 0, \end{cases} \tag{5.17}$$

and from the second equation in (5.17) we would have

$$v_t + L[v] + N_2[u^2] + O(\epsilon^3) = 0. \tag{5.18}$$

Hence, to effectively uncouple the system, we would be required to make the substitution for v at every instance in the first equation of (5.17) using (5.18), which at this point is the subject of the author's ongoing work.

Now, we would like to present a slightly different approach in deriving a unidirectional version of (5.11). Rather than introducing two auxiliary variables u and v, we adhere to our original form and keep Φ as our main variable of interest and write down (5.11) in the following form

$$\Phi_{tt} + \mathcal{M}^2[\Phi] + \mathcal{Q}(\Phi, \Phi_t) = 0 \quad \Rightarrow \quad \left(\frac{\partial}{\partial t} + i\mathcal{M}\right)\left(\frac{\partial}{\partial t} - i\mathcal{M}\right)\Phi + \mathcal{Q}(\Phi, \Phi_t) = 0, \tag{5.19}$$

where the operator $\mathcal{M}$ has the following representation in Fourier space

$$\hat{\mathcal{M}} = \mathrm{sgn}(\kappa)\sqrt{g|\kappa|\tanh(|\kappa|h)}$$

and $\mathcal{Q}$ for a moment being just the second order nonlinear correction (in general any order - second or higher).

At the leading order

$$\left(\frac{\partial}{\partial t} + i\mathcal{M}\right)\left(\frac{\partial}{\partial t} - i\mathcal{M}\right)\Phi = 0 \quad \Rightarrow \quad (2i\mathcal{M})\left(\frac{\partial}{\partial t} - i\mathcal{M}\right)\Phi = 0, \tag{5.20}$$

and therefore

$$\left(\frac{\partial}{\partial t} - i\mathcal{M}\right)\Phi + \left[\frac{1}{2}(i\mathcal{M})^{-1} + h.o.t.\right]\mathcal{Q}(\Phi, \Phi_t) = 0. \tag{5.21}$$

A key point, which still lacks a rigorous justification, is that we postulate that at second order the higher order terms ($h.o.t.$) can be neglected and hence we arrive at the at the following decoupled unidirectional version of (5.11)

$$\begin{aligned}\Phi_t - i\mathcal{M}[\Phi] = \; & (-i\mathcal{M})^{-1}\left[\Phi_x i\mathcal{M}[\Phi_x]\right] + \tfrac{1}{2}(i\mathcal{M})^{-1}[\Phi_{xx} i\mathcal{M}[\Phi]] \\ & -\tfrac{1}{2}(i\mathcal{M})^{-1}(\,\mathcal{L}[i\mathcal{M}[\Phi]\mathcal{L}[\Phi]]\,) + \tfrac{1}{2}(i\mathcal{M})^{-1}\,(\,\mathcal{L}[\Phi]\,\mathcal{L}[i\mathcal{M}[\Phi]]\,)\,.\end{aligned} \tag{5.22}$$

The above expression (5.22) is believed to be asymptotically equivalent to (5.15) and the transition from one form to the other will be addressed in the next paragraph. It should also be pointed out that at the next (third) order, it is believed that the higher

order terms (*h.o.t.*) in (5.21) can no longer be neglected and their corresponding form will be discussed in the next subsection.

To compare the above result with the one obtained by using the approach of two auxiliary variable (u, v) we will use (5.12) to go from (5.22) to (5.15). In other words, we substitute

$$\Phi = (i\mathcal{M})^{-1}[u - v]$$

directly into (5.22) and upon discarding the terms which contain v in the second order (nonlinear) correction $\mathcal{Q}$, hence being consistent and keeping the error of $O(\epsilon^3)$, we obtain the following

$$\begin{aligned} u_t - i\mathcal{M}[u] - (v_t - i\mathcal{M}[v]) \;=\; & -\tfrac{1}{2}\left(2u_x(i\mathcal{M})^{-1}[u_x] + u(i\mathcal{M})^{-1}[u_{xx}]\right) \\ & +\tfrac{1}{2}\left(\mathcal{L}\left[u\,\mathcal{L}\left[(i\mathcal{M})^{-1}[u]\right]\right]\right) \\ & -\tfrac{1}{2}\left(\mathcal{L}\left[(i\mathcal{M})^{-1}[u]\right]\,\mathcal{L}[u]\right). \end{aligned} \tag{5.23}$$

In order to make (5.23) equivalent to (5.15) we need the last two terms on the left-hand-side to be zero at this (second) order. Hence, recalling that $v = \frac{1}{2}\left(\Phi_t - i\mathcal{M}[\Phi]\right)$ and $\Phi_{tt} + \mathcal{M}^2[\Phi] = -\mathcal{Q}(\Phi, \Phi_t) + O(\epsilon^3)$ and at the same time, since in 5.21 we tentatively assumed that $\Phi_t - i\mathcal{M}[\Phi] = -(2i\mathcal{M})^{-1}\mathcal{Q} + O(\epsilon^3)$, we have

$$\begin{aligned} v_t - i\mathcal{M}[v] \;&=\; v_t + i\mathcal{M}[v] - 2i\mathcal{M}[v] \\ &=\; -\tfrac{1}{2}\mathcal{Q} - i\mathcal{M}[\Phi_t] - \mathcal{M}^2[\Phi] + O(\epsilon^3) \\ &=\; -\tfrac{1}{2}\mathcal{Q} - i\mathcal{M}\left[\Phi_t - i\mathcal{M}[\Phi]\right] \\ &=\; -\tfrac{1}{2}\mathcal{Q} - i\mathcal{M}\left[(2i\mathcal{M})^{-1}(-\mathcal{Q})\right] + O(\epsilon^3) \\ &=\; \tfrac{1}{2}\mathcal{Q} - \tfrac{1}{2}\mathcal{Q} = O(\epsilon^3). \end{aligned} \tag{5.24}$$

Thus (5.24) shows that the last two terms on the left-hand-side of (5.23) are indeed $O(\epsilon^3)$, hence making (5.23), or rather (5.22), asymptotically equivalent to (5.15). Furthermore, with the help of (5.32) and (5.33) we can further deduce that

$$\frac{\partial}{\partial t}\mathcal{Q} \;=\; i\mathcal{M}[\mathcal{Q}] \,+\, O(\epsilon^3) \quad \Longrightarrow \quad (i\mathcal{M})^{-1}\frac{\partial}{\partial t}\mathcal{Q} \;=\; \mathcal{Q} + O(\epsilon^3), \tag{5.25}$$

which will be an important fact in the derivation of the next (third) order correction terms in the subsequent section.

Also, under the same underlying assumption (5.21), it is helpful to write down the bi-directional (5.26) and uni-directional (5.27) models solely in terms of surface elevation (ζ) correct up to second order, respectively

$$\begin{aligned}\zeta_{tt} - g\mathcal{L}[\zeta] = \; & \tfrac{g^2}{2}\mathcal{L}\left[\left((i\mathcal{M})^{-1}[\zeta_x]\right)^2\right] - \tfrac{g^2}{2}\mathcal{L}\left[\left(\mathcal{L}\left[(i\mathcal{M})^{-1}[\zeta]\right]\right)^2\right] \\ & + g\tfrac{\partial}{\partial x}\left(\zeta_t(i\mathcal{M})^{-1}[\zeta_x] + \zeta\zeta_x\right) + g\mathcal{L}\left[\zeta_t\mathcal{L}\left[(i\mathcal{M})^{-1}[\zeta]\right] + \zeta\mathcal{L}[\zeta]\right] + O(\epsilon^3)\,,\end{aligned} \tag{5.26}$$

$$\begin{aligned}\zeta_t - i\mathcal{M}[\zeta] \; = \; & \tfrac{g}{4}i\mathcal{M}\left[\left((i\mathcal{M})^{-1}[\zeta_x]\right)^2\right] - \tfrac{g}{4}i\mathcal{M}\left[\left(\mathcal{L}\left[(i\mathcal{M})^{-1}[\zeta]\right]\right)^2\right] \\ & + \tfrac{g}{2}(i\mathcal{M})^{-1}\left[\tfrac{\partial}{\partial x}\left(i\mathcal{M}[\zeta](i\mathcal{M})^{-1}[\zeta_x] + \zeta\zeta_x\right)\right] \\ & + \tfrac{1}{2}(i\mathcal{M})^{-1}\left[i\mathcal{M}[\zeta]\mathcal{L}\left[(i\mathcal{M})^{-1}[\zeta]\right] + \zeta\mathcal{L}[\zeta]\right] + O(\epsilon^3),\end{aligned} \tag{5.27}$$

where g is the acceleration due to gravity.

5.2.1 Third Order Uni-directional Model

Akers and Milewski (2008) applied their models to gravity-capillary waves, hence they only needed to carry out their expansions up to second order. In our case, however, since we are dealing primarily with gravity waves, we need to carry out our expansions up to third order in wave steepness (ϵ). At first we recall again the equation (5.19)

$$\Phi_{tt} + \mathcal{M}^2[\Phi] + \mathcal{Q}(\Phi, \Phi_t) = 0 \quad \Rightarrow \quad \left(\frac{\partial}{\partial t} + i\mathcal{M}\right)\left(\frac{\partial}{\partial t} - i\mathcal{M}\right)\Phi \; = \; -\mathcal{Q}(\Phi, \Phi_t), \tag{5.28}$$

and introduce a new unidirectional equation with nonlinear correction $\mathcal{R}$ of unknown form

$$\left(\frac{\partial}{\partial t} - i\mathcal{M}\right)\Phi \; = \; \mathcal{R}(\Phi), \tag{5.29}$$

where $\mathcal{Q}$ and $\mathcal{R}$ are in general, any order nonlinear corrections and can therefore be formally written down in powers of ϵ as

$$\begin{cases} \mathcal{Q} \;=\; Q_2 + Q_3 + ... \\ \mathcal{R} \;=\; R_2 + R_3 + ..., \end{cases} \tag{5.30}$$

where Q_2 and R_2 are the second order and Q_3 and R_3 are the third order corrections, and moreover, the the form of $\mathcal{Q}_2$ and $\mathcal{Q}_3$ are known a priori. Now, we substitute (5.29) into (5.28) and obtain the following

$$\begin{aligned} &\left(\tfrac{\partial}{\partial t} - i\mathcal{M}\right)\left(2i\mathcal{M}[\Phi] + \mathcal{R}\right) \;=\; -\mathcal{Q} \\ \implies &\tfrac{\partial \Phi}{\partial t} - i\mathcal{M}[\Phi] = -(2i\mathcal{M})^{-1}[\mathcal{Q}] - (2i\mathcal{M})^{-1}\left[\left(\tfrac{\partial}{\partial t} - i\mathcal{M}\right)\mathcal{R}\right] \;\equiv\; \mathcal{R}. \end{aligned} \tag{5.31}$$

In addition, from the previous section (key assumption) we know that at the second order

$$R_2 \;=\; -(2i\mathcal{M})^{-1} Q_2, \tag{5.32}$$

and hence we can also deduce that

$$(2i\mathcal{M})^{-1}\left[\left(\frac{\partial}{\partial t} - i\mathcal{M}\right) R_2\right] \;=\; O(\epsilon^3). \tag{5.33}$$

Consequently, at the third order we have

$$-(2i\mathcal{M})^{-1} Q_3 - (2i\mathcal{M})^{-1}\left[\left(\frac{\partial}{\partial t} - i\mathcal{M}\right)\left(R_2 + R_3 + O(\epsilon^4)\right)\right] \;\equiv\; R_3. \tag{5.34}$$

Note that Q_3 can be obtained from the $\mathcal{C}\{\Phi, \Phi_t\}$ expression in (5.9) with every appearance of time derivative $\frac{\partial}{\partial t}$ being replaced with $i\mathcal{M}$ and therefore with the help of (5.32) we can can symbolically write down the next (third) order correction R_3 from (5.30), or rather (5.29), in the following form

$$\left(\frac{1}{2} + (2i\mathcal{M})^{-1}\frac{\partial}{\partial t}\right) R_3 \;=\; -(2i\mathcal{M})^{-1}\left[Q_3 - (2i\mathcal{M})^{-1}\left[\frac{\partial Q_2}{\partial t} - i\mathcal{M}[Q_2]\right]\right]. \tag{5.35}$$

However, we suspect, without further justification at the moment that the following equality will hold

$$\left(\frac{1}{2} + (2i\mathcal{M})^{-1}\frac{\partial}{\partial t}\right) R_3 = R_3 + O\left(\epsilon^4\right).$$

It should also be mentioned that at this stage of the development, due to a dependence of $\mathcal{Q}_2$ on time on the right hand side of (5.35), any numerical discretization of the temporal domain would yield an implicit system, thus potentially requiring either a direct or an iterative inversion of the temporal derivative matrix.

CHAPTER 6

DISCUSSION AND CONCLUSIONS

6.1 Discussion

The main focus of this manuscript has been the development of an accurate numerical model for the short-term evolution of weakly nonlinear ocean surface waves. In that respect, the aforementioned Weakly 2D model, based on additional assumption of weak transverse dependence, behaved surprisingly well in directional wave fields. The spectral evolution for the first two cases of initial directional distribution ($\beta = 0.14, 0.35$) give excellent qualitative and quantitative agreement between the Weakly and Fully 2D models. The latter cases of $\beta = 0.7$ for two values of wave steepness ($\epsilon = 0.08, 0.13$) show differences in spectral evolution, but these disparities are usually located towards the high wavenumbers, hence the end of the spectrum. To quantify that further, we reintroduced the mean spreading function in (4.1) averaged over wavenumber $k = \sqrt{k_x^2 + k_y^2}$ and showed in Figures (4.7)-(4.8) that the Weakly 2D model tends to have a higher mean spread than the Fully 2D model; albeit both models suggested the existence of a quasi-steady state for the mean spreading function when simulated over 150 peak periods (150 sec).

When the time frame was increased by a factor of six (900 sec), we showed that the mean directional distribution function does indeed converge to an apparent steady state. The same was the case for the angularly integrated spectra. Moreover, it was evident that the spectral peak experiences a permanent downshifting (at least on our time scale, 900 sec), even though our models do not allow for wave breaking. What was also interesting, was the fact that as the spectrum was approaching this steady state in its distribution (for the averaged case of 100 simulations for up to

900 sec, $\beta = 0.7$ and $\epsilon = 0.13$), the spectral bandwidth has also been progressively decreasing concurrent with the downshifting of the spectral peak.

Also, we believe that in part the modulational instability, nonlinear wave-wave interaction, and energy transfer is behind the observed spectral downshifting in the case of broad directional distribution. In fact, Waseda et al. (2009b) suggested that an initial directional distribution of $\beta = 0.35$ gives rise to the transition from the so-called quasi-resonant to the full resonant interaction. When the latter is ultimately in effect whenever the initial spreading (β) is larger than 0.35. Onorato et al. (2002) argued that the modulational instability is suppressed whenever the initial directional distribution is higher than $\beta \sim 0.26$, however we believe that the modulational instability will still be in effect for the dominant waves that are steep enough. The reasoning behind this argument is that in the examination of surface elevations for fairly broad directional fields ($\beta = 0.35$ and above), we frequently observed (not shown here) irregular wavetrains of an adjacent triplet of large waves, whose height was well above twice the significant wave height (H_s).

Finally, in Figures 4.20 and 4.21 we managed to show a deterministic comparison between surfaces of the two models. It is rather comforting to see that the Weakly 2D model is in good qualitative agreement with the Fully 2D model, even for the wave fields with relatively broad directional distribution ($\beta = 0.7$) and essentially for the duration of the entire simulation (150 sec).

One of the main advantages of the Weakly 2D model is its gain in the computational speed. Mainly, in Weakly 2D system (2.14)-(2.15) there are only two terms that depend on the transverse wavenumber variable k_y. Because of that, we can cut down the computation time of all the other remaining terms via 2D FFT (two-dimensional Fast Fourier Transform) by 50%. In other words, wherever we have any x-derivative, which would correspond to k_x Fourier multiplier, we can elect to carry out only a 1D (one-dimensional) Fourier transform along the x-direction for

every single y-component, thus essentially performing 50% of the operations required for a 2D FFT.

In summary, in the face of limited computational resources there is a pressing need to reduce the cost of evaluating hydrodynamic models, without losing the level of necessary accuracy and preserving the desired coherent structures. The derivation of the Weakly 2D model was carried out with exactly that in mind. In fact, with the application to for instance Naval hydrodynamics, this problem becomes even more acute in the context of ensemble modeling – which requires a large, statistically significant number of model runs, and variational data assimilation – which itself requires repeated forward and backward integrations of the model. In such large-scale computational settings, model reductions that are capable of generating compact system representations and can capture essential features of the fully articulated high resolution model with only a small loss of fidelity, offer enormous potential benefits to the operational utility of computational models.

APPENDIX A

MODULATIONAL INSTABILITY OF STOKES WAVES OF THE MODIFIED NONLINEAR SCHRÖDINGER (MNLS) EQUATION

Equations (2.22)-(2.23) have a particularly straightforward exact uniform wave solution known as the Stokes wave, given by

$$A = A_0 \mathrm{e}^{-\frac{i|A_0|^2 t}{2}}. \tag{A.1}$$

The reconstruction of the surface elevation accurate to third order in wave steepness (ϵ) in terms of the Stokes wave can be written as

$$\zeta = \epsilon \cos(\theta) + \frac{\epsilon^2}{2}\cos(2\theta) + \frac{3\epsilon^3}{8}\cos(3\theta).$$

The stability of the Stokes wave can be found by simple perturbation of the both the amplitude A_0 and phase θ. Before that is carried out, we would like to rewrite the coupling term $\left(iA\frac{\partial\bar{\phi}}{\partial x}\right)$ in the MNLS equation (2.22), so that it is completely uncoupled from the Laplace equation for the velocity potential. From the reconstruction formulae we know that

$$\frac{\partial\bar{\phi}}{\partial z} = \frac{1}{2}\frac{\partial|A|^2}{\partial x} \quad \text{at} \quad z = 0,$$

where $\bar{\phi}$ is the velocity potential defined at the mean surface level ($z = 0$). When we take the Fourier transform of the above expression, we obtain with the help of our integral operator (2.9) the following relation

$$\mathcal{F}\left[\frac{\partial\bar{\phi}}{\partial z}\right] = \frac{i}{2}k_x\mathcal{F}\left[|A|^2\right] \equiv W_0 = \kappa\tanh(\kappa h)\hat{\bar{\phi}} \quad \text{where} \quad \kappa \equiv \sqrt{k_x^2 + k_y^2}.$$

Hence,

$$\hat{\bar{\phi}} = \frac{ik_x}{2}\left(\kappa\tanh(\kappa h)\right)^{-1}\mathcal{F}\left[|A|^2\right]$$
$$\implies iA\frac{\partial\bar{\phi}}{\partial x} = -iA\mathcal{F}^{-1}\left[\frac{k_x^2}{2}\left(\kappa\tanh(\kappa h)\right)^{-1}\mathcal{F}\left[|A|^2\right]\right],$$

where $\mathcal{F}$ and $\mathcal{F}^{-1}$ form the forward and inverse Fourier transform pair. Consequently, perturbing the amplitude and phase and linearizing we obtain

$$A = A_0(1+a)\mathrm{e}^{i\theta}\mathrm{e}^{-\frac{i}{2}|A_0|^2t} \sim A_0(1+a+i\theta)\mathrm{e}^{-\frac{i}{2}|A_0|^2t},$$

where a and θ are infinitesimal perturbations of the amplitude and phase, respectively. Then, substituting into equation 2.22 and seeking the plane wave solution we impose

$$\begin{pmatrix} a \\ \theta \end{pmatrix} = \begin{pmatrix} \hat{a} \\ \hat{\theta} \end{pmatrix}\mathrm{e}^{i(k_xx+k_yy-\omega t)} + c.c,$$

where $c.c$ stands for the complex conjugate and $\omega \in \mathbb{C}$ gives the instability region. After some algebraic simplifications we arrive at the formula for $\omega(k_x, k_y)$, with the growth rate of the instability being the imaginary part of it [$\mathrm{Im}(\omega)$]

$$\omega(k_x,k_y) \;=\; -\left(\alpha+\frac{1}{4}|A_0|^2k_x\right) \pm \sqrt{\frac{1}{4}|A_0|^4k_x^2 - 4\beta\left(|A_0|^2+2\hat{\mathcal{M}}-\beta\right)}, \qquad \text{(A.2)}$$

where

$$\alpha \;=\; \frac{k_x}{2}+\frac{k_x^3}{16}-\frac{3}{8}k_xk_y^2+\frac{5}{4}|A_0|^2k_x$$
$$\beta \;=\; \frac{k_x^2}{8}-\frac{k_y^2}{4}$$
$$\hat{\mathcal{M}}\{\cdot\} \;=\; \frac{-k_x^2}{2\sqrt{k_x^2+k_y^2}}\mathcal{F}\{\cdot\}.$$

In turn, the complex value of ω achieved whenever

$$\frac{1}{4}|A_0|^4k_x^2 - 4\beta\left(|A_0|^2+2\hat{\mathcal{M}}-\beta\right) < 0,$$

will lead to perturbations becoming unstable.

Figure A.1 shows the instability region for the MNLS equation for various values of the wave steepness (ϵ), with imposed color intensity shading to describe larger areas of instability (occurring in the center).The growth rate is symmetric over the k_x axis, hence we only show the first quadrant. Also, Figure A.2 gives the so-called stability boundary curve (when the discriminant for the growth rate ω is zero), along with horizontal and vertical lines indicating where the de-aliasing zero-pad filter was imposed (according to cubic nonlinearity). In addition, the circular arc, where the augmented zero-pad filter was imposed in the numerical simulations via the Fourier pseudo-spectral method of the MNLS to get rid off the growing cascade of energy (instability), is shown in Figure 4.26. Note that the instability region is disconnected from its other branch, as opposed to the hyperbola being uniformly connected for the case of simple hyperbolic cubic Nonlinear Schrödinger Equation (NLS). The hyperbolic NLS has the property that the instability regions is unbounded (inside the stability boundary curve, of course) and that fact contributes to the unlimited leak/cascade of energy out to large wavenumbers (short-crested waves become excited), see Martin and Yuen (1980).

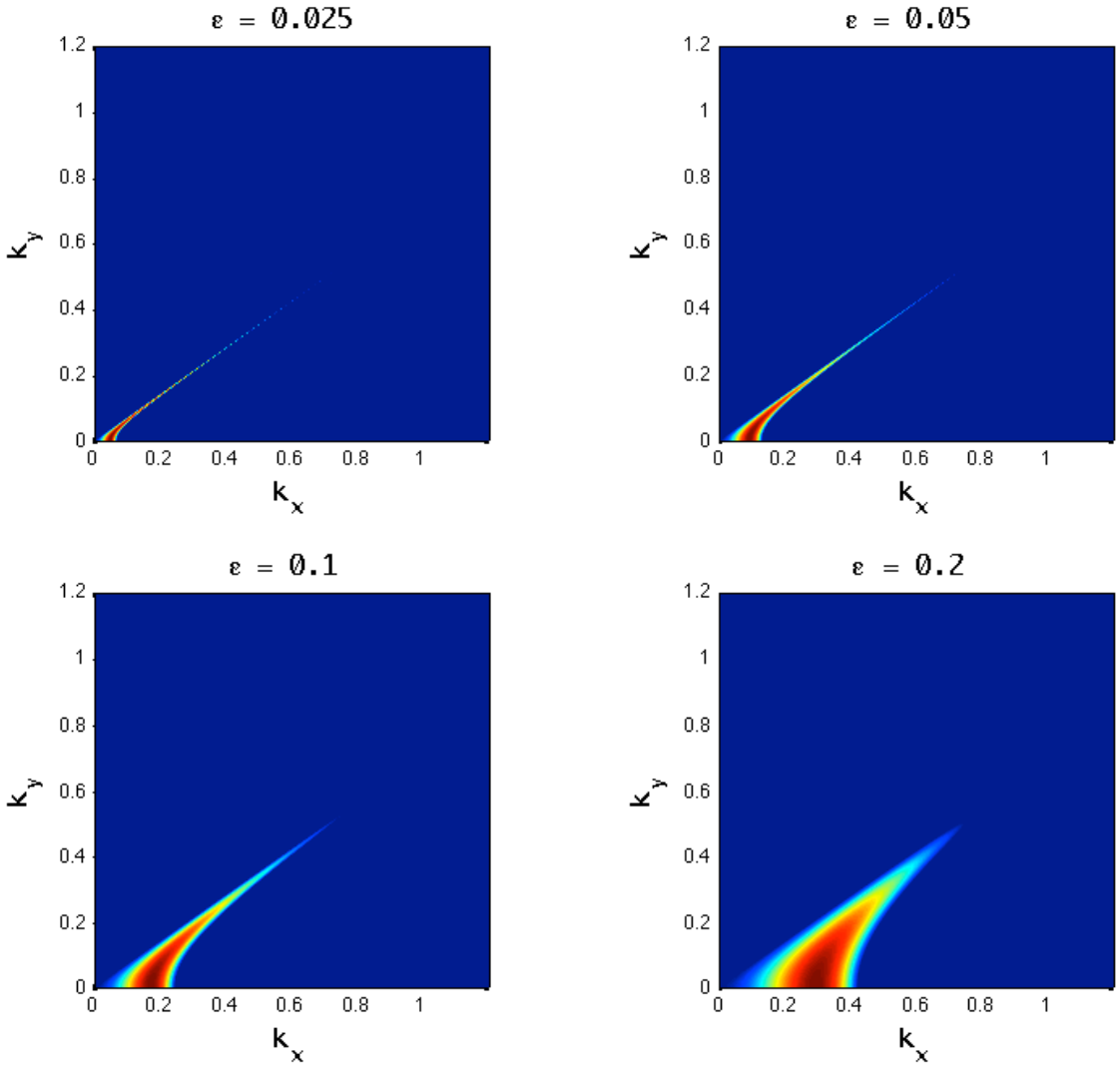

Figure A.1 Instability region of the Modified Nonlinear Schrödinger Equation (MNLS) for various initial values of the wave steepness $\epsilon = 0.025, 0.05, 0.1, 0.2$. The center of the curve resembling the highest intensity shading gives rise to the most unstable modes.

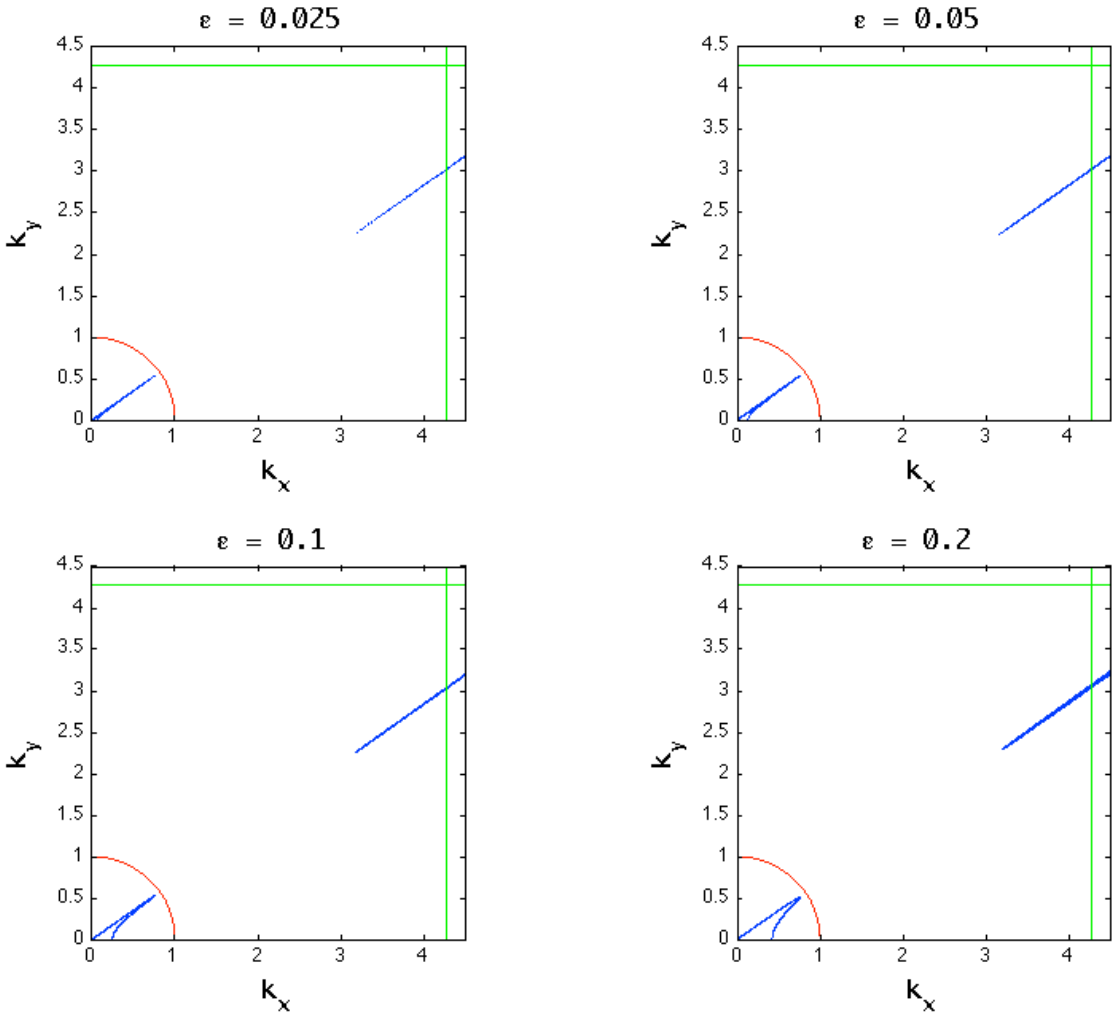

Figure A.2 Stability boundary of the Modified Nonlinear Schrödinger Equation (MNLS) for various initial values of the wave steepness $\epsilon = 0.025, 0.05, 0.1, 0.2$. Two vertical and horizontal lines mark the areas of the de-aliasing filter for the cubic nonlinearity and the circular arc is the augmented filter applied to the Fourier pseudo-spectral method for suppressing the instabilities appearing in Figure 4.26.

REFERENCES

[1] Akers, B. & Milewski, P. A. 2008 *Model Equations for Gravity-Capillary Waves in Deep Water*, Stud. Appl. Math., **121**, 49 - 69.

[2] Babanin, A., V., Chalikov, D., Young, I. R. & Savelev, I. 2010 *Numerical and Laboratory Investigation of Breaking of Steep Two-Dimensional Waves in Deep Water*, J. Fluid Mech. **644**, 433 - 463.

[3] Bateman, W. J. D., Swan, C. & Taylor, P. H. 2001 *On the Efficient Numerical Simulation of Directionally Spread Surface Water Waves*, J. Comput. Phys. **174**, 277 - 305.

[4] Brinch-Nielsen, U. & Jonsson, I. G. 1986 *Fourth Order Evolution Equations and Stability Analysis for Stokes Waves on Arbitrary Water Depth*, Wave Motion, **8**, 455 - 472.

[5] Chase, A. G. *http://www.bell.mma.edu/achase/NS-221-Big-Wave.html*

[6] Choi, W. 1995 *Nonlinear Evolution Equations for Two-Dimensional Surface Waves in Fluid of Finite Depth*, J. Fluid Mech. **295**, 381 - 394.

[7] Choi W. & Lyzenga, D. R. 2006 *Nonlinear Surface Wave Dynamics in Slowly Varying Ocean Environments*, **26** Symposium on Naval Hydrodynamics.

[8] Clamond, D., Francius, M., Grue, J. & Kharif, C. 2006 *Long Time Interaction of Envelope Solitons and Freak Wave Formations*, Eur. J. of Mech. B/Fluids **25**, 536 - 553.

[9] Craig, W. & Sulem, C. 1993 *Numerical Simulation of Gravity Waves*, J. Comput. Phys. **108**, 73 - 83.

[10] Dommermuth, D. G. & Yue, D. K. 1987 *A High-Order Spectral Method for the Study of Nonlinear Gravity Waves*, J. Fluid Mech. **184**, 267 - 288.

[11] Dysthe, K. B. 1979 *Note on a Modification to the Nonlinear Schrödinger Equation for Application to Deep Water Waves*, Proc. R. Soc. Lond. A **369**, 105 - 114.

[12] Dysthe, K.B. & Trulsen, K. 1999 *Note on Breather Type Solutions of the NLS as Models for Freak-Waves*, Physica Scripta **82**, 48 - 52.

[13] Dysthe, K. B., Trulsen, K., Krogstad, H. & Socquet-Juglard, H. 2003 *Evolution of a Narrow-Band Spectrum of Random Surface Gravity Waves*, J. Fluid Mech. **478**, 1 - 10.

[14] ESA (European Space Agency) 2004 *Ship-Sinking Monster Waves Revealed by ESA Satellites.*

[15] Goullet, A. & Choi, W. 2011 *A Numerical and Experimental Study on the Nonlinear Evolution of Long-Crested Irregular Waves*, Phys. Fluids **23**, 016601, 1 - 15.

[16] Haver, S. 2005 *Freak Waves: a Suggested Definition and Possible Consequences for Marine Structures*, In: Olagnon, M., & Prevosto, M. (eds), Rogue Waves 2004, Ifremer, France.

[17] Hwang, P. A., Wang, D. W., Walsh, E. J., Krabill, W. B. & Swift, R. N. 2000 *Airborne Measurements of the Wavenumber Spectra of Ocean Surface Waves. Part II: Directional Distribution*, J. Phys. Oceanogr. **30**, 2768 - 2787.

[18] Kadomtsev, B. B. & Petviashvili, V. I. 1970 *On the Stability of Solitary Waves in Weakly Dispersive Media*, Sov. Phys. Dokl. **15**, 539 - 541.

[19] Kharif, C., Pelinovsky, E. & Talipova, T. 2000 *Nonlinear Dispersive Mechanism of the Freak Wave Formation in Shallow Water*, Phys. D. **147**, 83 - 94.

[20] Kharif, C., Pelinovsky, E. & Slunyaev, A. 2009 *Rogue Waves in the Ocean*, Adv. in Geoph. and Env. Mech. and Math., Springer-Verlag Berlin Heidelberg.

[21] Komar, P. D. 2007 *Higher Waves Along U.S. East Coast Linked to Hurricanes*, Eos Trans. AGU 88:301.

[22] Lawton, G. 2001 *Monsters of the Deep (The Perfect Wave)*, New Scientist 170, No. 2297:28 - 32.

[23] Lavrenov, I.V. 1998 *The Wave Energy Concentration at the Agulhas Current of South Africa*, Natural Hazards **17**, 117 - 127.

[24] Lo, E. Y. & Mei, C. C. 1987 *Slow Evolution of Nonlinear Deep-Water Waves in Two Horizontal Directions: A Numerical Study*, Wave Motion **9**, 245 - 259.

[25] Martin, D. U. & Yuen, H. C. 1980 *Quasi-Recurring Energy Leakage in the Two-Space-Dimensional Nonlinear Schrödinger Equation*, Phys. Fluids, **23**, 881 - 883.

[26] McLean, J. W., Ma, Y. C., Martin, D. U., Saffman, P. G. & Yuen, H. C. *Three-Dimensional Instability of Finite-Amplitude Water Waves*, Phys. Rev. Lett. **46**, 817 - 821.

[27] Ochi, M. K. 2005 *OCEAN WAVES: The Stochastic Approach*, Cambridge Ocean Technology Series 6, Cambridge University Press.

[28] Onorato, M., Osborne, A. R. & Serio, M. 2002 *Extreme Wave Events in Directional, Random Oceanic Sea States*, Phys. Fluids **14**, 25 - 28.

[29] Onorato, M., Osborne, A., Serio, M., Cavaleri, L., Brandini, C. & Stansberg, C. T. 2006 *Extreme Waves, Modulational Instability and Second Order Theory: Wave Flume Experiments on Irregular Waves*, Eur. J. Mech. B/Fluids **25**, 586 - 601.

[30] Osborne, A. R. 2010 *Nonlinear Ocean Waves and the Inverse Scattering Transform*, Intern. Geoph. Series, **97**, Elsevier.

[31] Pushkarev, A., Resio, D. & Zakharov V. E. 2003 *Weak Turbulent Approach to the Wind-Generated Gravity Sea Waves*, Physica D **184**, 29 - 63.

[32] Sedletsky, Y. V. 2003 *The Fourth-Order Nonlinear Schödinger Equation for the Envelope of Stokes Waves on the Surface of a Finite-Depth Fluid*, J. Exp. Theor. Phys, **97**, 180 - 193.

[33] Smith, R. 1976 *Giant Waves*, J. Fluid Mech., **77** – part 3, 417 - 431

[34] Socquet-Juglard H., Dysthe, K., Trulsen, K., Krogstad, H., E. & Liu, J. 2005 *Probability Distributions of Surface Gravity Waves During Spectral Changes*, J. Fluid Mech. **542**, 195 - 216.

[35] Tanaka, M. 2001 *A Method of Studying Nonlinear Random Field of Surface Gravity Waves by Direct Simulation*, Fluid Dyn. Research – Elsevier **28**, 41 - 60.

[36] Tanaka, M. 2007 *On the Role of Resonant Interactions in the Short-Term Evolution of Deep-Water Ocean Spectra*, J. Phys. Oceanogr. **37:4**, 1022 - 1036.

[37] Toffoli, A., Gradstad, O., Trulsen, K., Monbaliu, J., Bitner-Gregersen, E. & Onorator, M. 2010 *Evolution of Weakly Nonlinear Random Directional Waves: Laboratory Experiments and Numerical Simulations*, J. Fluid Mech. **664**, 313 - 336.

[38] Trulsen, K. & Dysthe, K. B. 1990 *Frequency Down-Shift Through Self Modulation and Breaking*, Water Wave Kinematics - A. Torum and O. T. Gudmestad (eds.), Kluwer Academic Publishers, 561 - 572.

[39] Trulsen, K. & Dysthe, K. B. 1996 *A Modified Nonlinear Schödinger Equation for Broader Bandwidth Gravity Waves on Deep Water*, Wave Motion **24**, 281 - 289.

[40] Trulsen, K. & Dyshe K. B. 1997 *Freak Waves – A Three-Dimensional Wave Simulation*, Proc. 21st Symposium on Naval Hydrodynamics, National Academy Press, USA, 550 - 560.

[41] Tsai, W.-T. & Yue, D. K. 1996 *Computation of Nonlinear Free-Surface Flows*, Annu. Rev. Mech. **28**, 249 - 279.

[42] Waseda T. 2006 *Impact of Directionality on the Extreme Wave Occurrence in a Discrete Random Wave*, In Proceedings of 9th International Workshop on Wave Hindcasting and Forecasting, Victoria, Canada.

[43] Waseda, T., Kinoshita, T. & Tamura, H. 2009a *Evolution of a Random Directional Wave and Freak Wave Occurrence*, J. Phys. Oceanogr. **39**, 621 - 639.

[44] Waseda, T., Kinoshita, T. & Tamura, H. 2009b *Notes and Correspondences: Interplay of Resonant and Quasi-Resonant Interaction of the Directional Ocean Waves*, J. Phys. Oceanogr. **39**, 2351 - 2362.

[45] West, B. J., Brueckner, K. A., Janda, R. S., Milder, M. & Milton, R. L. 1987 *A New Numerical Method for Surface Hydrodynamics*, J. Geophys. Res. **92**, 11,808 - 11,824.

[46] White, B.S. & Fornberg, B. 1998 *On the Chance of Freak Waves at Sea*, J. Fluid Mech. **355**, 113 - 138.

[47] Zakharov, V. E. 1968 *Stability of Periodic Waves of Finite Amplitude on the Surface of a Deep Fluid*, J. Appl. Mech.Tech. Phys. **9**, 190 - 194.